Open access • Journal Article • DOI:10.1063/1.1660771

Precipitation in high purity silicon single crystals. — Source link

E. Nes, J. Washburn

Published on: 01 Aug 1971 - Journal of Applied Physics (American Institute of Physics)

Topics: Nucleation, Silicon, Dislocation and Precipitation (chemistry)

2 cys

UCRL-19608

PRECIPITATION IN HIGH PURITY SILICON SINGLE CRYSTALS

Aasmund Erik Nes
(Ph. D. Thesis)

August 1970

AEC Contract No. W-7405-eng-48

LAWRENCE RADIATION LABORATORY
UNIVERSITY of CALIFORNIA BERKELEY

UCRL-19608

DISCLAIMER

PAGES i to ii

WERE INTENTIONALLY

LEFT BLANK

Contents

PRECIPITATION IN HIGH PURITY SILICON SINGLE CRYSTALS

Aasmund Erik Nes

Inorganic Materials Research Division, Lawrence Radiation Laboratory
Department of Materials Science and Engineering, College of Engineering
University of California, Berkeley

ABSTRACT

Precipitation in high purity, Lopex (low oxygen, dislocation free), silicon has been examined by x-ray diffraction topography and transmission electron microscopy. It has been found that the impurity concentration in the as-grown silicon crystals is sufficient to cause precipitation of a second phase if the specimens are annealed in the temperature range 700 to 1000°C, followed by a critical cooling rate. The precipitating phase has been tentatively identified as α-Fe_3Si.

The precipitates appear in colonies. Each colony has a three dimensional star like configuration, where the different arms are planar arrangements of precipitates enveloped by a dislocation loop. The dislocation loops are of interstitial edge type and both $a/2\langle 110\rangle$ and $a\langle 100\rangle$ Burgers vectors are involved.

The nucleation of colonies is heterogeneous in nature and the presence of small silica particles as nucleation centers is suggested. The critical cooling rate effect is explained in terms of a vacancy condensation mechanism.

Following the nucleation step is the generation of dislocation loops with either $a/2\langle 110\rangle$ or $a\langle 100\rangle$ Burgers vectors. The different Burgers vectors give rise to two growth modes resulting in colony branches with characteristic differences in precipitate size and distribution, as well as in dislocation structure.

1. INTRODUCTION

This work was initiated by the discovery of a precipitation effect in undoped, low oxygen, dislocation free silicon samples, graded as of high purity.

This precipitation effect exhibits striking similarities with that reported on copper in silicon.[1-6] The present results will, to some extent, be analyzed in terms of this copper precipitation effect. Some of the characteristic results reported in the literature on the precipitation of copper in silicon are briefly outlined in the following paragraphs.

It is well known that copper precipitates on dislocations during quenching of copper doped silicon crystals. This effect has been used as a dislocation decoration technique.[1] Transmission electron microscopy studies of foils made from silicon crystals saturated with copper at high temperatures, and subsequently quenched to room temperature, show that small spherical precipitates are trailing dislocation segments that have moved nonconservatively.[3] The most extensive works on copper precipitation have been carried out by Fiermans and Vennik.[4-6] These authors report that by quenching copper doped silicon crystals, star-like precipitates appear both on, and isolated from the grown in dislocations. A growth mechanism was proposed for the copper precipitates which is based on indentation at silica precipitates, followed by climb of dislocation loops. The climbing dislocations leaving copper specks in their trail, thus forming precipitate colonies. The experimental techniques deployed by Fiermans and Vennik were infrared microscopy,[4,5] x-ray diffraction topography[5] and electron microprobe analysis,[6] all techniques with very limited resolution. Thus,

no observations related to dislocation structure and precipitate arrangements within the star branches were reported.

Only the macroscopic geometrical structure of the copper precipitate colonies has been determined. No mechanism has been proposed for the growth kinetics of these colonies and on the nucleation of copper precipitate colonies the only theory is that based on indentation of the silicon matrix by silica particles.[4,5] As no experimental evidence of silica precipitates in the as-grown material was presented by Fiermans and Vennik, this nucleation mechanism cannot be considered established.

In the present investigation the general geometrical shape and the internal strucutre of the precipitate colonies have been studied in great detail. The experimental techniques involved have primarily been transmission electron microscopy. Both conventional 100 kV and high voltage 650 kV electron microscopes have been used. X-ray diffraction topography was used to study the bulk distribution of precipitates. Models for the nucleation and growth of the colonies have been developed. An interesting aspect is that these models may apply to the precipitation of a series of impurity atoms in silicon.

It is beyond the scope of this work to determine or predict what influence this precipitation effect may have on the electronic properties of the silicon samples. However, one should bear in mind that this precipitation effect is caused by impurities present in as-grown materials designed for production of electronic components.

2. EXPERIMENTAL

2.1 Specimen Preparation

The silicon single crystals were obtained from Texas Instruments Company. The material was graded as Lopex (low oxygen, dislocation free silicon). The crystals were Czochralski grown in the form of cylindrical rods of 1 in. diam × 6 in., with [111] growth axis. The resistance of the crystals were 50 Ω-cm and the conductivity was n type.

Wafers with [111], [110] and [100] surface orientation were cut from the cylindrical rod with a diamond saw. Wafer thicknesses were in the range 0.22 mm to 1 mm, where the thinner specimens were used for preparation of foils for electron microscopy studies, and the thicker for x-ray diffraction topography investigations. After cutting, the wafers were chemically polished in order to remove the damaged surface layer. The polishing solution used was of the following composition.[7]

A freshly prepared mixture of 65% A and 35% B where

(A) is 3:1 mixture of concentrated HNO_3 and 45% HF, and

(B) is 2.5 g of iodine in 100 ml of glacial acetic acid.

After polishing, the wafers were washed in distilled water, then dried in acetone.

2.1.1 Heat Treatments

The specimens were annealed either in air, or in evacuated quartz capsules. The capsules, Fig. 1, had a diameter of approximately one inch. The temperature close to the specimen was monitored during the heat treatment by a thermocouple sealed into the capsule. A simple muffle furnace was used for the experiments. The diagram in Fig. 2

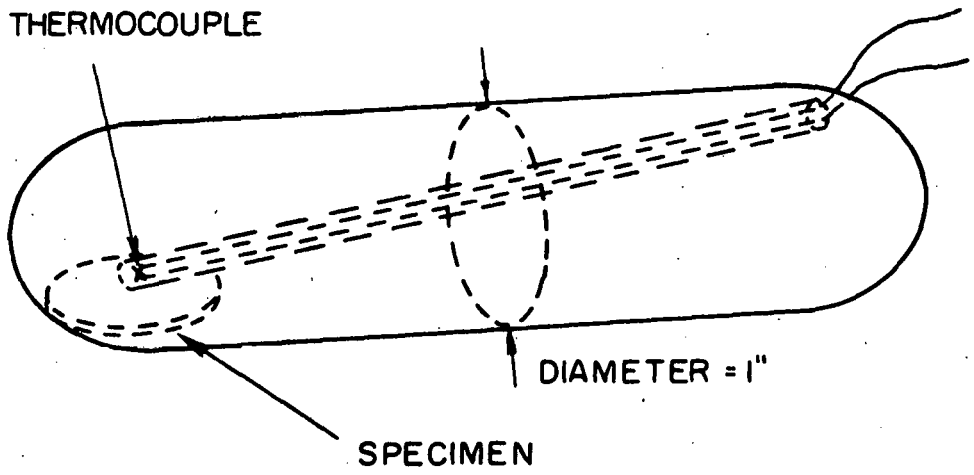

Fig. 1. Sketch showing a specimen in a quartz capsule.

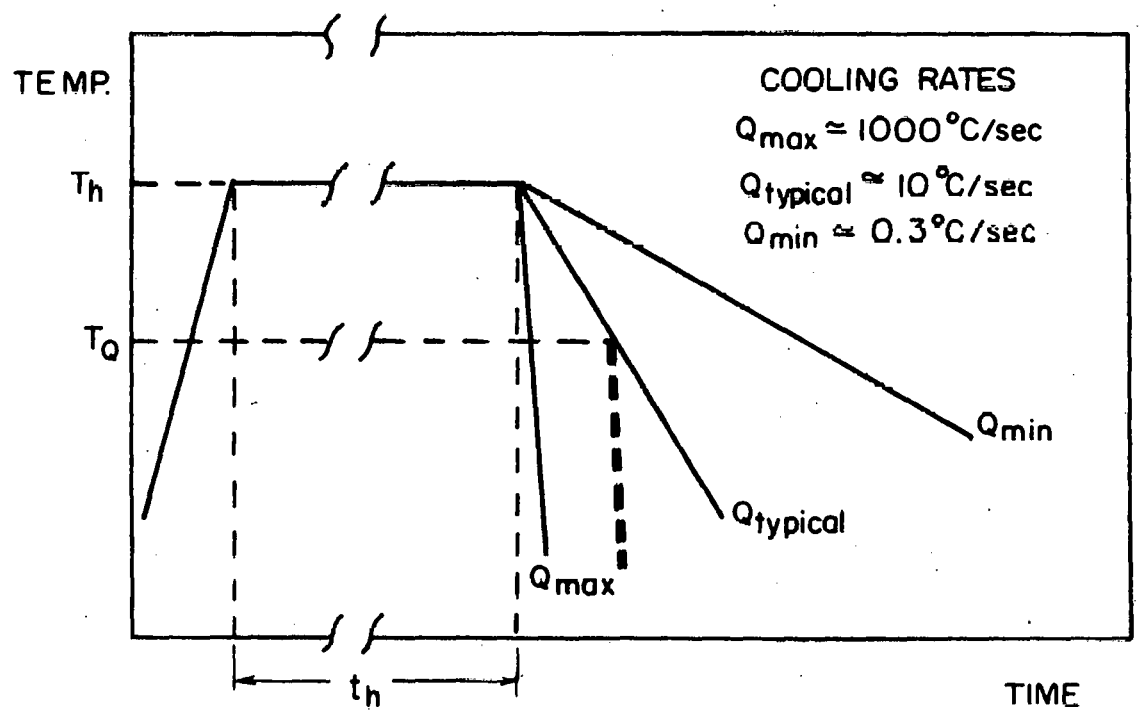

XBL 707-1554

Fig. 2. The heat treatments given to the specimens. The temperature, T_h, was ranged from 723°C up to 976°C. The annealing time, t_h, was in the range from about 2 minutes up to about 30 minutes.

shows the heat treatments given to the specimens. The annealing temperature, T_h, ranged from about 700°C up to about 1000°C. The annealing times, t_h, varied from a few minutes up to 30 minutes. Specimens subjected to a wide range of cooling rates have been examined. For the encapsulated specimens different cooling rates were obtained by either having the capsules furnace cooled, air cooled outside the furnace or cooled by dropping the hot capsule into a liquid cooling agent. The cooling rates in these three cases were 0.3°C/sec, 6°C/sec and 12°C/sec respectively. Faster cooling was achieved for the specimens annealed in air. By air cooling of specimens wrapped in thin platinum foils, cooling rates of about 22°C/sec were obtained. The temperature was monitored by a thermocouple attached to the foil. Some specimens have been quenched into silicone oil. The exact cooling rate during quenching cannot be measured directly, but theoretical estimates based on the heat conductivity and the geometrical shape of the specimens indicate that the cooling may be as fast as 1000°C/sec or more.

Some experiments required an abrupt change in the cooling rate, as shown by the heavy broken line in Fig. 2. This was achieved by keeping the specimen in a specially designed alumina tube. This tube was similar in construction to the capsule in Fig. 1, except that the rear end was open (the front end to be where the specimen is, Fig. 1). By air-cooling of this alumina tube from temperatures in the range 8-900°C a cooling rate of about 8-10°C/C was measured. This cooling rate could be interrupted at any temperature, T_Q, by dropping the specimen through the open end of the tube into silicone oil.

2.2 X-ray Diffraction Topography Technique

The x-ray diffraction topography technique, like transmission electron microscopy, reveals crystalline defects inside the material. The advantage of the x-ray technique compared to electron microscopy is that relatively thick crystals (Si, approx. 2 mm) can be studied. In the present investigation the x-ray topography technique was used to study bulk density and distribution of defect clusters. The main disadvantage of this technique is the low resolution (approx. 5 μm). The x-ray diffraction technique of Lang[8] was applied. The geometry of the experimental setup is schematically shown in Fig. 3. The x-ray source is S and C is the specimen oriented for Bragg reflection. The source to specimen distance is about 60 cm. The divergence in the x-ray beam is limited by the slit V_1. The photographic plate P is at a right angle to the diffracted beam. The photographic plate will record only the area exposed by the slit V_1. In order to obtain a topograph of the entire wafer, the photographic plate and the crystal are translated simultaneously back and forth in the direction indicated by the arrows. V_2 is a stationary slit to stop the transmitted beam from striking the photographic plate.

Two x-ray diffraction Lang cameras manufactured by Rigaku-Denki and Jarrell Ash have been used together with a Hilger and Watts microfocus x-ray generator. $Mo_{k\alpha 1}$ radiation was used, and the tube was operating at 40 kV and 2.5 mA. The topographs were recorded on Ilford G5 nuclear emulsion plates with emulsion thickness 50 μm. A detailed description of the experimental setup of the Lang camera and the processing of the nuclear plates are given in the Ph. D. thesis by V. C. Kannan.[9]

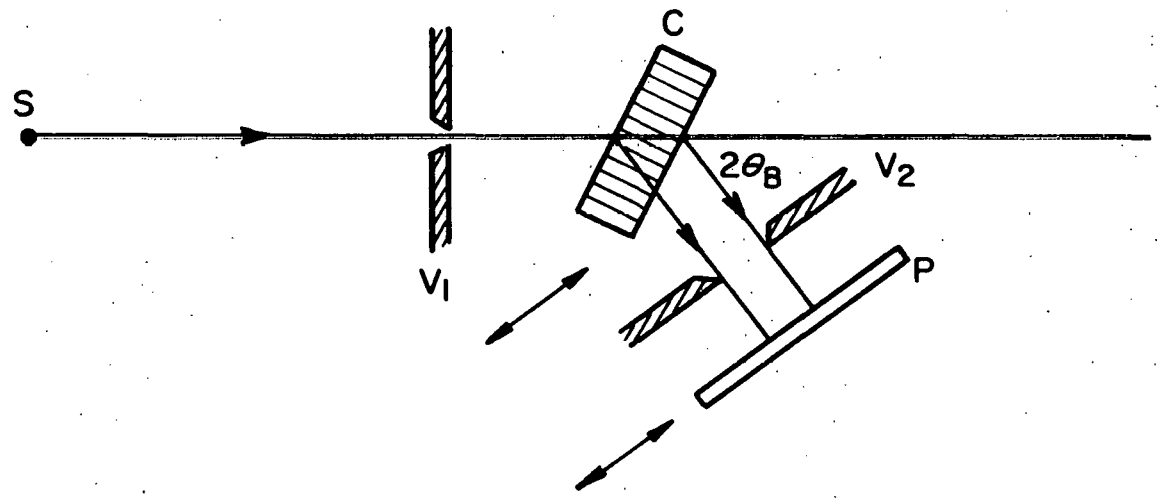

XBL 707-1555

Fig. 3. Sketch of the experimental arrangement explaining the principles of the Lang technique for taking topographs.

2.3 Transmission Electron Microscopy

Foils for transmission electron microscopy were prepared by using a chemical polishing technique developed by J. E. Lawrence and H. Koehler.[10] Specimens about 0.2 to 0.5 mm thick were chemically polished[7] down to a thickness of a few 100μm. Then the samples were mounted on a Teflon sheet with apiezon wax so that only one face was exposed. The chemical polishing was continued until the diameter of the samples were a few mm. The final diameter of the foils is dictated by the initial diameter to thickness ratio of the wafer. A 10 X 10 X 0.2 mm wafer will give a 2 mm diameter foil with central thickness somewhat less than 1μm.

The dislocation structure of the defect clusters were determined by using a Siemens Elmiscope electron microscope operating at 100 kV. The precipitates could not be identified from diffraction analysis, using the 100 kV microscope. The inelastic scattering obscured the precipitate reflections even in selected area diffraction patterns from very thin foils. These difficulties were overcome by using the high voltage Hitachi electron microscope operating at 650 kV. Because of the better resolution obtained by the high voltage microscope, this microscope was used to determine the morphology of the precipitates. The high voltage microscope is equippped with a hot stage specimen holder. This holder was used to carry out a few annealing experiments in the microscope.

To distinguish between micrographs taken on the different microscopes, the figure numbers will be followed by (100 kV) or (650 kV) indicating 100 kV Siemens and 650 kV Hitachi micrographs respectively.

3. EXPERIMENTAL RESULTS

3.1 Bulk Distribution of Precipitate Colonies

No defects, precipitates or dislocations have been observed in the as-grown material, either by x-ray or by electron microscope observations. However, surface etching of as grown (111) wafers reveals a ring pattern as shown in Fig. 4a.* The rings consist of a high density of triangular etch pits, Fig. 4b. By heating an as-grown specimen to a temperature in the range 700-1000°C for a few minutes, and then cooling at a moderate rapid rate, about 10°C/sec, a high density of precipitate colonies were introduced. Each colony appears as a small black dot on the x-ray topograph, Fig. 5. As will be demonstrated in Section 3.3 each black dot in the x-ray topographs represents a colony of precipitates and dislocation tangles. Figure 5a and b represent wafers cut normal and parallel to the [111] growth axis. The wafer cut normal to this axis, Fig. 5a, indicates an even distribution of colonies, while the topograph from the wafer cut parallel to the growth axis, Fig. 5b, shows that the colonies are segregated into a stack of narrow planar areas, recorded as slightly curved lines on the photographic plate. The segregated layers of high colony concentration are oriented normal to the growth axis, and the curvature of the layers is nearly symmetrical about the crystal ingot axis. The

---

* Lattice defects and precipitates in silicon single crystals can easily be revealed by surface etching. First the specimens are chemically polished.[7] After polishing the specimens are etched for ten minutes in a 50% HF - 50% Cr-acid solution.[11]

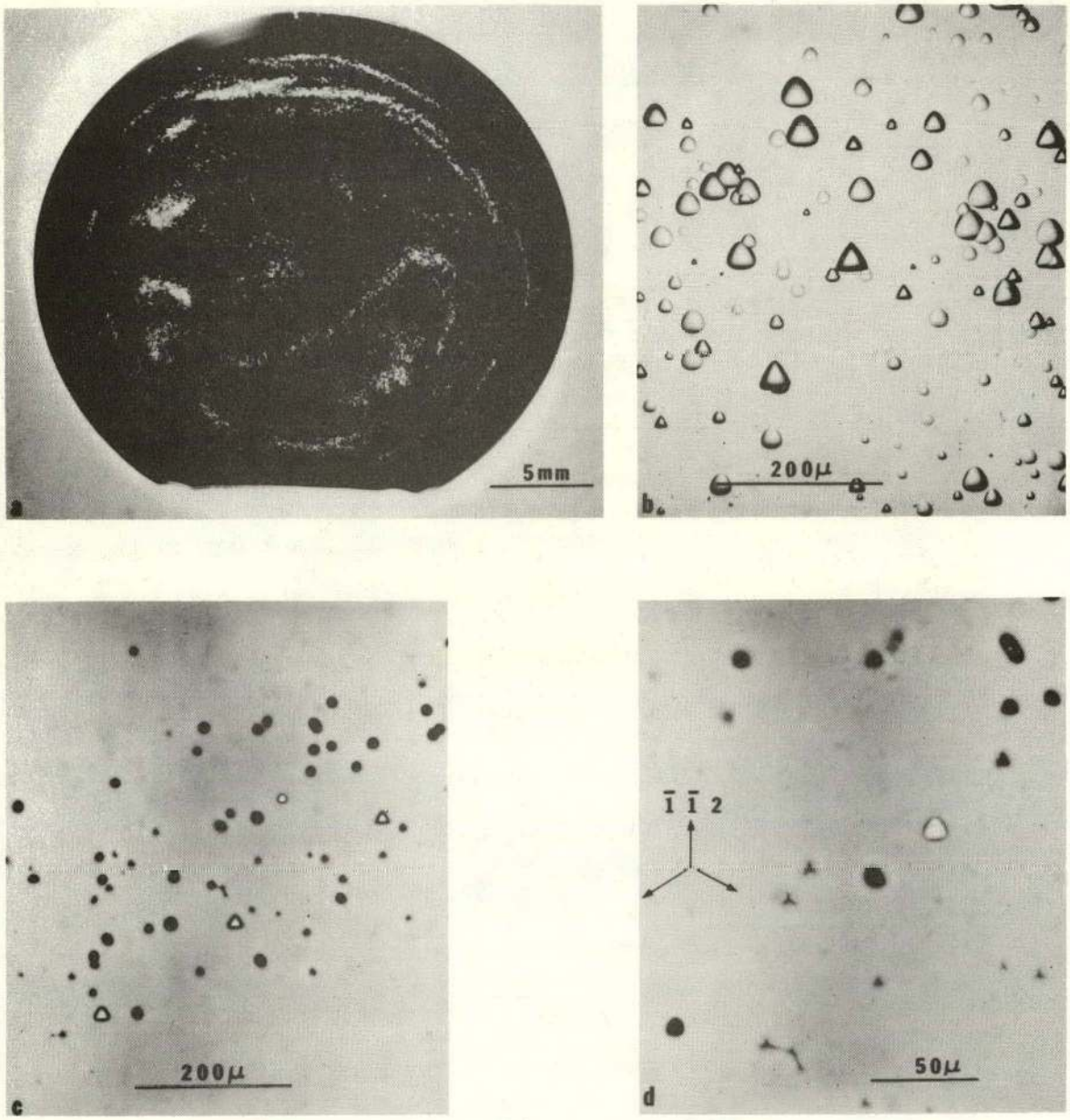

XBB 707-3130

Fig. 4. Surfaces of etched (111) silicon wafers. (a and b) As grown material. (c and d) Heat treated specimens.

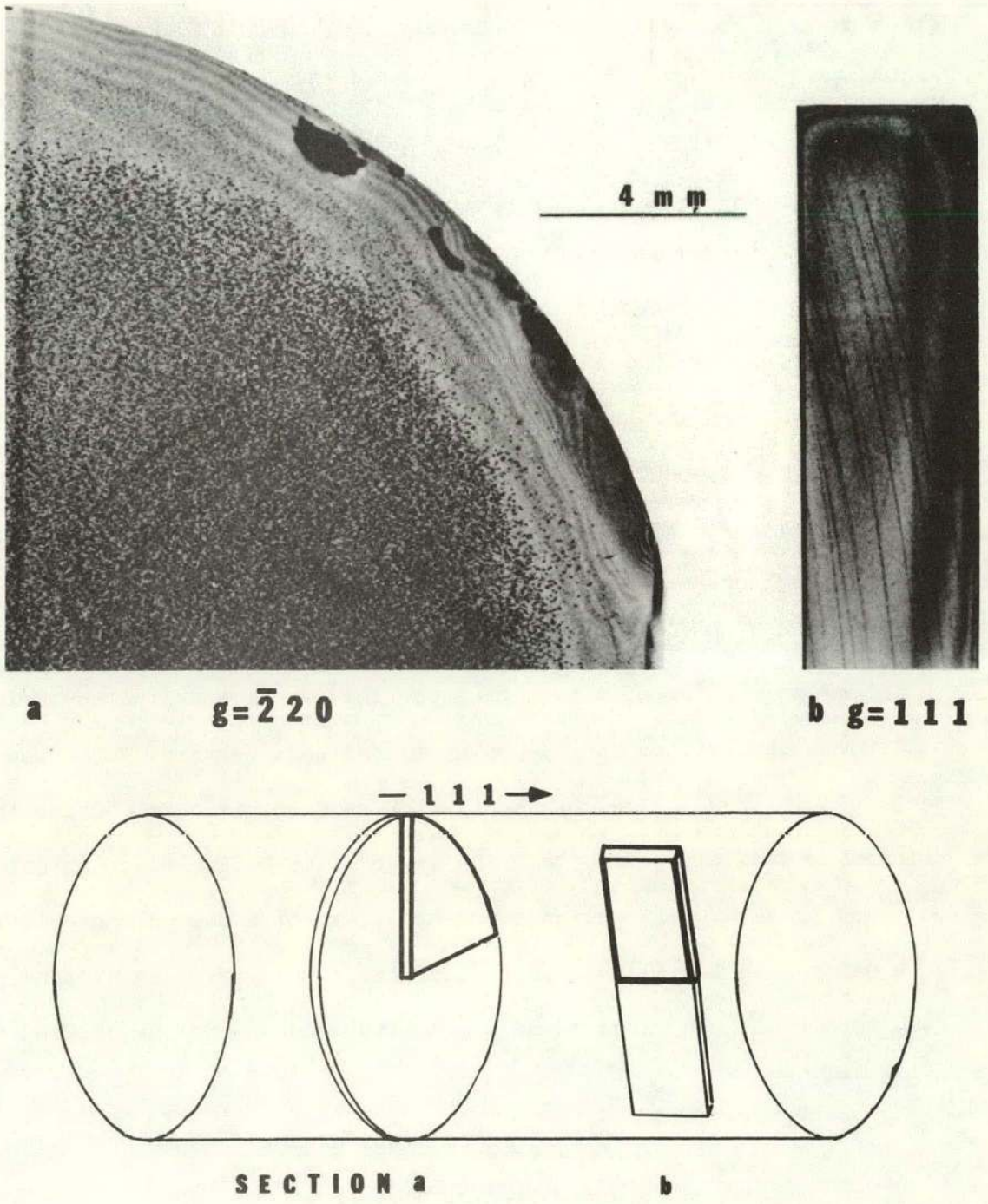

Fig. 5. X-ray diffraction topographs. (a) A (111) wafer annealed at 865°C for 20 minutes, then cooled at a rate of 7°C/sec. (b) A (110) wafer annealed at 820°C for 10 minutes and then cooled at a rate of 7°C/sec.

discs of high colony concentration had a thickness of about 100 μm and they were located a few 100 μm apart. The density of colonies within these areas was about 10^6-10^7 colonies/cm^3. A characteristic feature was the smaller colony sizes and eventually the colony free zone close to the cylindrical crystal surface, Fig. 5.

Long needle shaped precipitates have been observed in some of the x-ray topographs from (111) wafers, Fig. 6a and b. The topograph in Fig. 6a shows two 1.2 mm long precipitates in the [011] direction, both extending from one surface to the other of the 1 mm thick wafer. Figure 6b shows three rod shaped precipitates all about 0.2 mm long and oriented in a $[\bar{1}01]$ direction parallel to the wafer surface. Note the depleted zones surrounding these rod shaped precipitates.

Surface etching of a heat treated (111) wafer show the same ring pattern as observed on the as-grown crystal surface (Fig. 4a). The defect colonies however, give rise to etch tops or hillocks, rather than triangular etch pits, Fig. 4c. The layer distribution of colonies, as observed by x-ray diffraction topography, explains the characteristics etch pattern on the (111) crystal surfaces. The structure of some of the etch tops have been resolved as stars with branches in the 112 directions, Fig. 4d.

3.2 Critical Cooling Rate

The diagram in Fig. 2 shows the heat treatments given to the specimens. The precipitate colonies are formed during the cooling period. If the annealing temperature, T_h in Fig. 2, is above 700°C and the annealing time, t_h exceeds a few minutes, then precipitation will occur if the cooling rate is at least 1°C/sec, or does not exceed several hundred

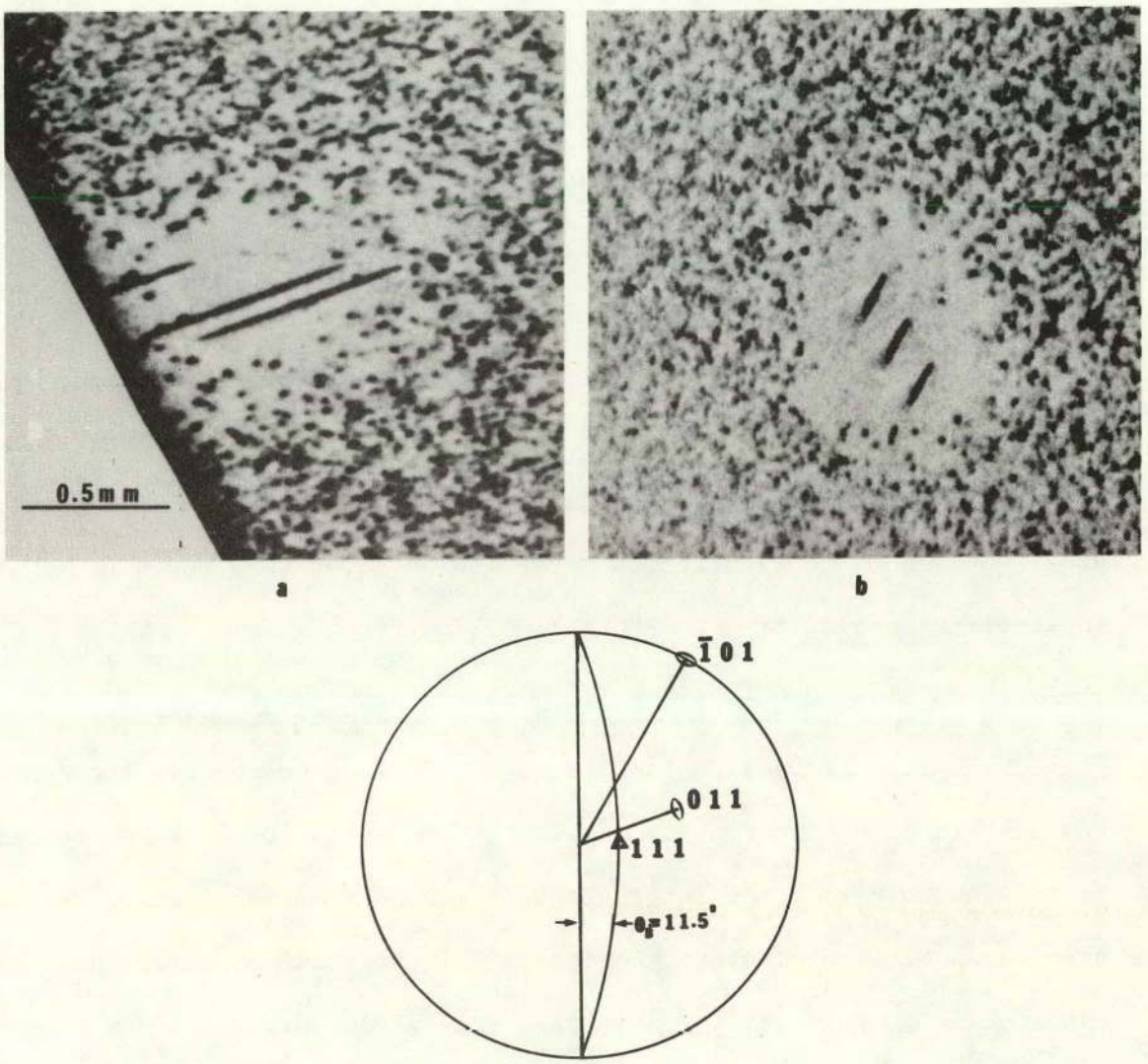

XBB 707-3131

Fig. 6. X-ray diffraction topographs of (111) wafers showing needle-like precipitates in the ($\bar{1}$01) and the (011) directions, $\vec{g} = \bar{2}20$.

degrees per second. Thus, the colony formation is a critical cooling effect.

Precipitation has been observed in specimens cooled from temperatures as low as 723°C. For specimens cooled from temperatures below about 800°C the density of colonies is lower than in specimens cooled from higher temperatures. No systematic change in colony density, size and structure could be related to variation of the annealing temperature in the range 820°C up to 974°C. The general shape and the internal structure of the colonies were not influenced by varying the cooling rate from about 4°C/sec up to 22°C/sec, however the colonies were somewhat bigger in specimens cooled at the 22°C/sec cooling rate.

3.3 Geometrical Structure of the Precipitate Colonies

The x-ray diffraction topographs in Figs. 5 and 6 give the density and distribution of colonies. However, the resolution in these topographs is too low to reveal the internal structure of individual colonies. By using transmission electron microscopy this internal structure has been examined in great detail. The micrographs given in Figs. 7 and 8 show typical colony formations as found in (111) foils. Each colony shows a three dimensional star or dendritic shape, with each arm of the configuration consisting of a nearly planar arrangement of small precipitates. These precipitates appear as small black dots in the micrographs (Figs. 7 and 8). The geometry of the colonies is easily established by examining the schematic drawings in Fig. 9. Figure 9a is a (111) foil with a colony in it. The electron microscope will record a (111) projection of this colony, Fig. 9b. The transmission electron microscope requires thin foils. The actual thickness depends upon the beam voltage, being 1 μm at 100 kV and about 6 μm at 650 kV for silicon.[12] As typical

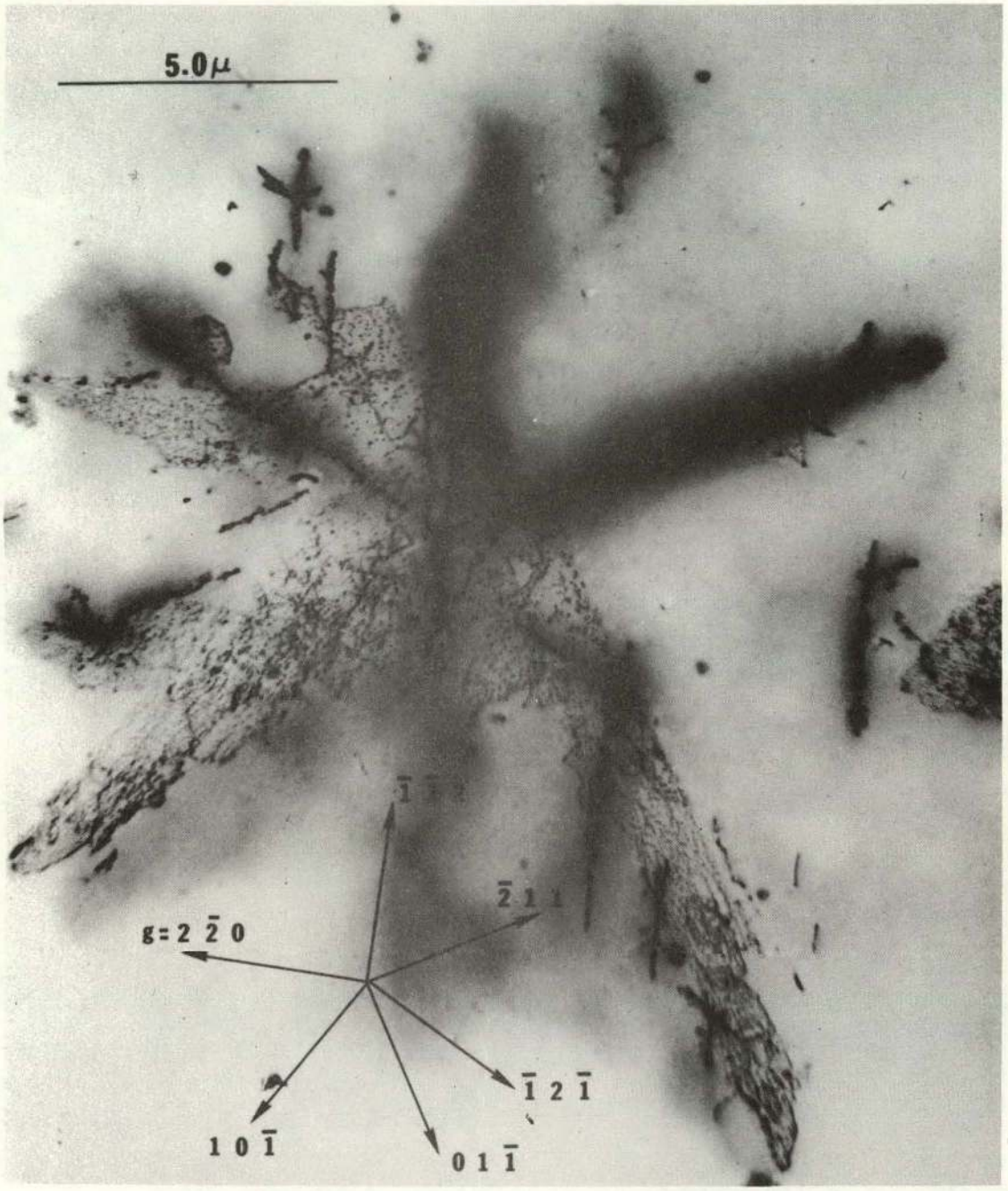

XBB 706-2837

Fig. 7. (100 kV, T_h = 884°C, t_h = 10 min, Q = 22°/sec)* A bright field micrograph of a colony in a (111) foil. The different arms are {110} planar precipitate arrangements.

* 100 kV indicates a micrograph from the Siemens microscope. T_h, t_h and Q gives the heat treatment of the specimen from which the foil has been prepared, see Fig. 2.

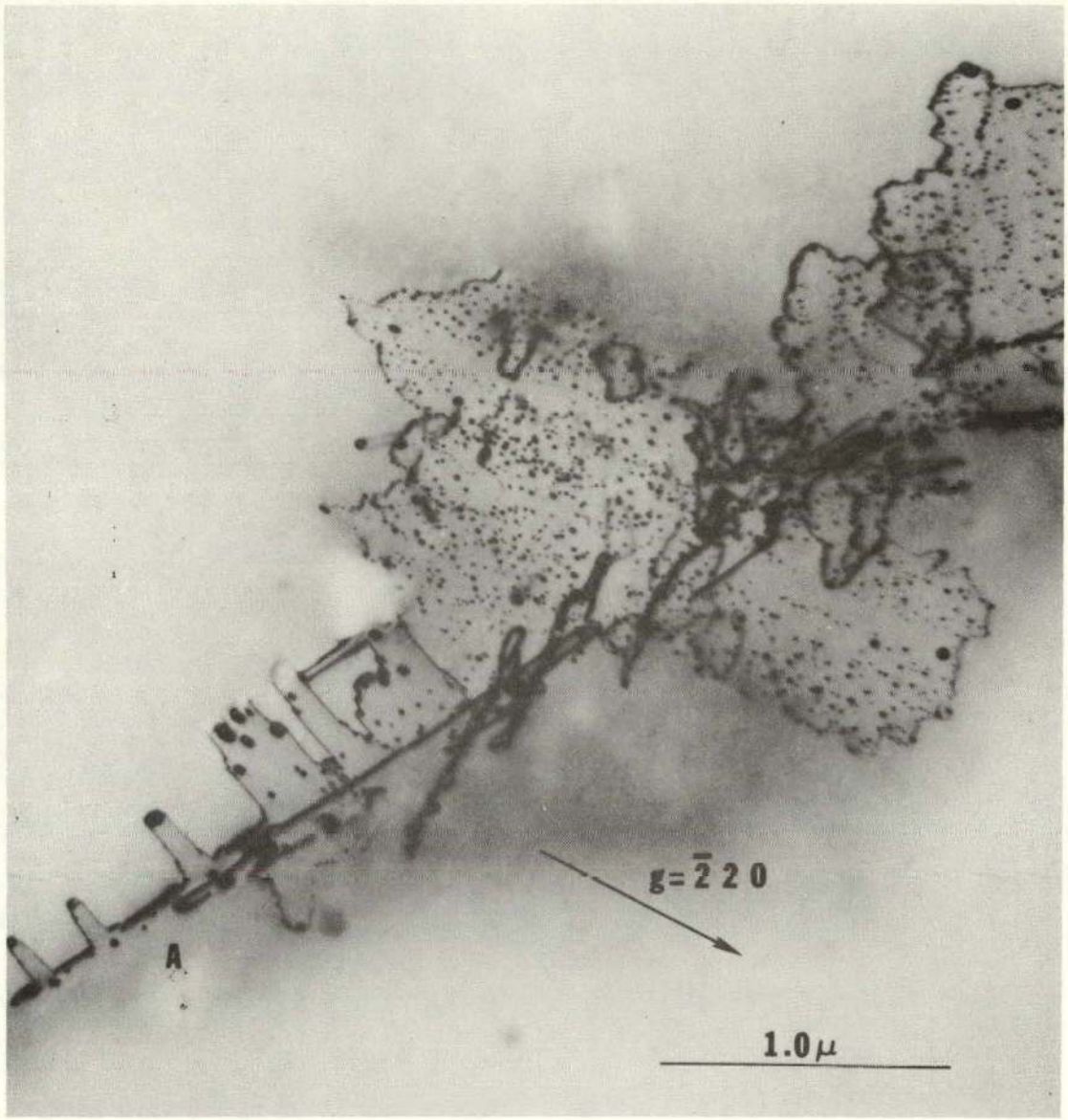

XBB 706-2842

Fig. 8. (100 kV, T_h = 882°C, t_h = 10 min, Q = 6°C/sec) A colony in a (111) foil. The arm marked A is of ⟨100⟩ type, the other arms are of the ⟨100⟩ type.

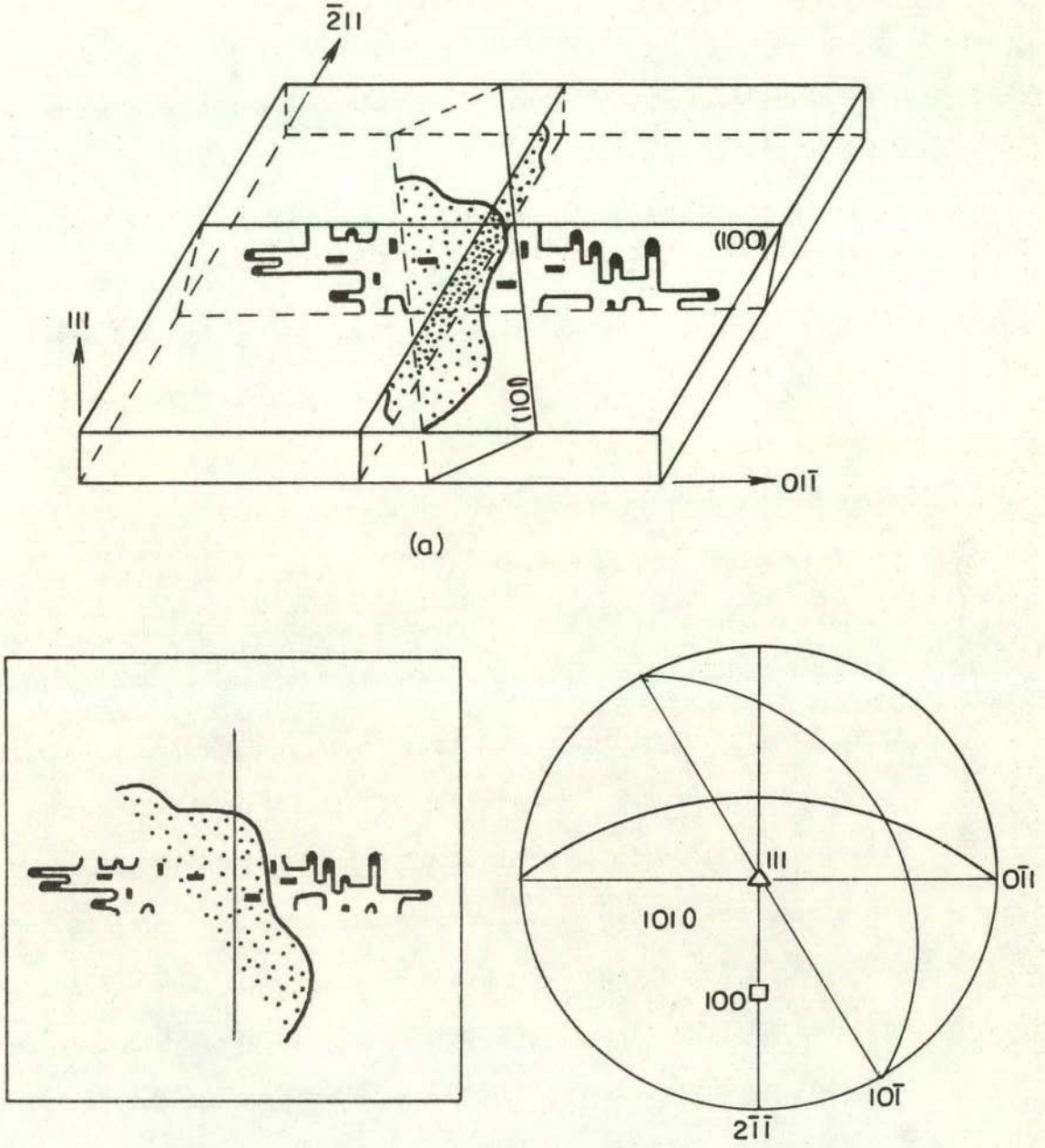

XBL 707-1553

Fig. 9. Sketch showing a colony in a (111) foil.

arm lengths for the configuration are up to 10 μm, only sections of a colony will appear within the surfaces of a foil. Figure 9 indicates that the different arms of a colony configuration are on {110} or {100} type crystallographic planes. The existence of {110} type configurations is easily verified as these planes in a (111) foil either cut the surface in a $\langle 112 \rangle$ or a $\langle 110 \rangle$ direction. The colony shown in Fig. 7 has only {110} type arms. In a (111) foil the coplanar {100} configurations will also cut the surfaces in $\langle 110 \rangle$ directions. To avoid that this configuration is confused with a {110} type, the colony geometry has to be examined in foils with another orientation. However, inspection of the stereographic projection in Fig. 9 shows that in a (111) micrograph the width of the (100) coplanar arrangement will be about half that of the (101) type (provided both arrangements extend from surface to surface of the foil). Based on this geometrical relationship the arm marked A in Fig. 8 is claimed to be of a {100} type, while all other arms in this micrograph are of the {110} type. The existence of {100} type arms are clearly demonstrated by the micrographs in Figs. 12 and 13, which show colonies in (110) foils. Figures 12 and 13 present colony arms either edge on, or inclined, cutting the foil surface in the $[1\bar{1}0]$, or the $[10\bar{1}]$ direction respectively. Simple geometrical considerations show this only applies to a {100} type configuration.

It will be shown in Section 3.5 that the two different types of colony arms are associated with dislocations of different Burgers vector. The dislocations involved in {110} and {100} type colony arms have $\frac{a}{2}\langle 110 \rangle$ and a $\langle 100 \rangle$ Burgers vectors respectively. As a colony arm is more generally described by its Burgers vector, rather than by the

crystallographic plane of the configuration, the direction of the Burgers vector will be used to distinguish between the different types of arms. Thus throughout the rest of this thesis the colonies will be referred to as made up of ⟨110⟩ and ⟨100⟩type arms.

Characteristic differences related to the dislocation structure, precipitate size and distribution are apparent between arms of the ⟨110⟩ and ⟨100⟩ type. In the ⟨110⟩ arms the precipitates appear to be nearly evenly distributed, and bounded by segments of an approximately circular dislocation loop. In the ⟨100⟩ type arms the enveloping dislocation forms long narrow branches in the orthogonal ⟨110⟩ directions, thus giving these arms a dendritic shape, (see the arm marked A in Fig. 8). The precipitates in ⟨100⟩ arms are much bigger in size, and a typical feature is that a precipitate is located at the tips of the dendrite branches.

3.4 The Precipitates

3.4.1 Identification

Selected area diffraction patterns from colonies in foils of different orientations have been examined. This analysis shows that the precipitates can be divided into two categories, that is, precipitates belonging to (1) ⟨110⟩ and (2) ⟨100⟩colony arms. The experimental data related to the two sets of precipitates are presented in separate sections below.

Precipitates belonging to ⟨110⟩ type colony arms

Dark field images and diffraction patterns from ⟨110⟩ type precipitate configurations in foils of (111) and (110) surface orientation are shown in Figs. 10 and 11. The selected area diffraction patterns in Fig. 10 show extra precipitate reflections close to, and in the direction of the

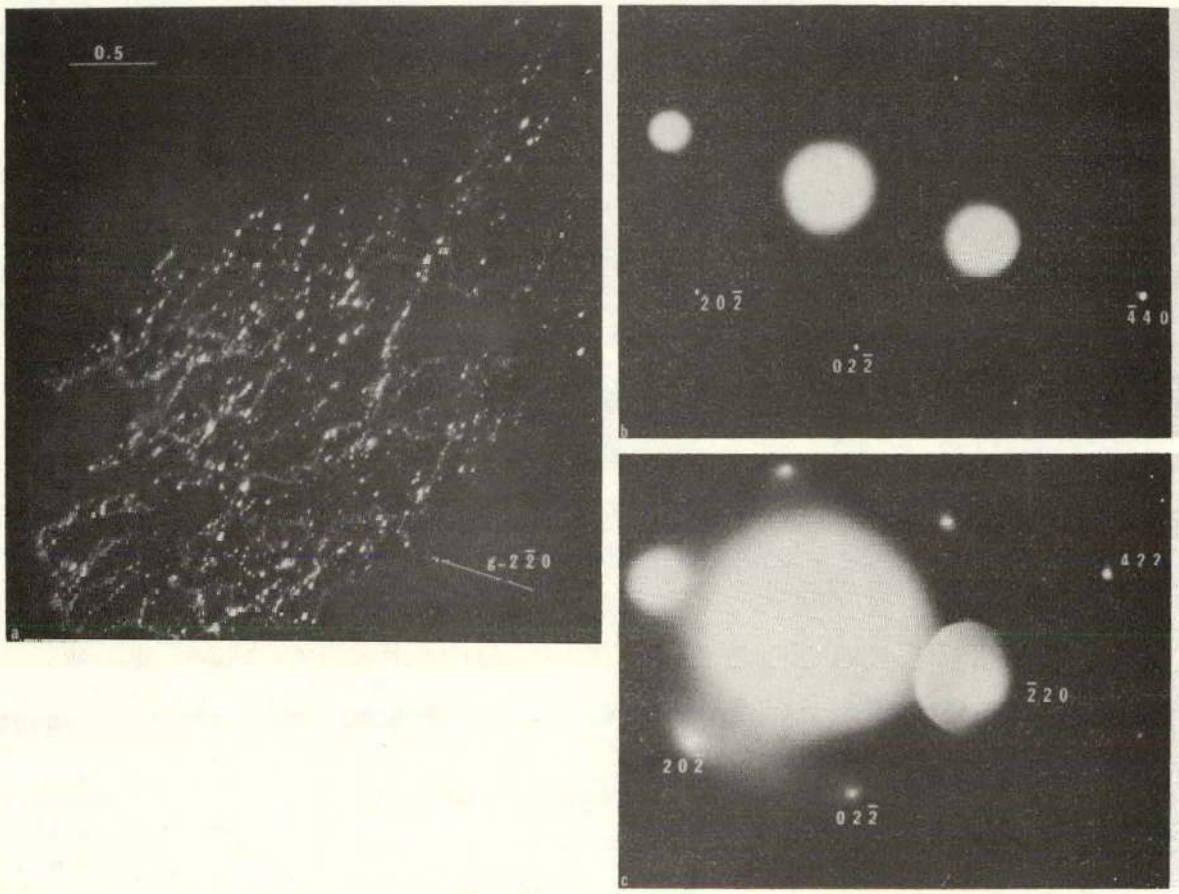

XBB 706-2848

Fig. 10. (650kV,* T_h = 820°C, t_h = 10 min, Q = 7°C/sec) (a) Dark field image of a ⟨110⟩ type colony arm in a (111) foil. (b and c) Selected area diffraction patterns from this arm in slightly different orientations.

* 650 kV indicates micrographs taken on the high voltage Hitachi microscope.

$[02\bar{2}]$ $[\bar{1}40]$ (Fig. 10b) and $[\bar{4}22]$ (Fig. 10c) matrix reflections. Due to the high intensity of the $(\bar{2}20)$ matrix reflection, Fig. 10b, the precipitate reflection associated with it cannot be resolved. However, the moiré analysis* in the subsequent paragraph suggests the presence of a strong precipitate reflection close to the $(\bar{2}20)$ matrix spot. Thus the strong precipitate dark field contrast, Fig. 10a, is due to electrons scattered by the precipitate lattice. The extra spots close to the $\langle 220 \rangle$ matrix reflections correspond to a precipitate lattice spacing of 2.00 ± 0.01 Å (the spacing of {220} silicon lattice planes are 1.92 Å). The spot near the $[\bar{1}22]$ matrix reflection gives a precipitate lattice spacing 1.16 ± 0.01 Å.

Close inspection of the photographic plate representing the micrograph in Fig. 10 shows that many of the precipitates contains moiré fringes. Moiré fringes appear as a result of interaction between electron waves scattered by the precipitates and the matrix. By measuring the fringe spacing, and by knowing the lattice spacing of the scattering matrix planes, then the spacing of the scattering precipitate planes can be calculated from the following relation.[13]

$$D = \frac{d_1 d_2}{d_1^2 + d_2^2 - 2d_1 d_2 \cos \gamma)^{1/2}} \quad \cdots\cdots \qquad (3.1)$$

$$\sin \phi = \frac{D}{d_2} \sin \gamma$$

where D is the moiré fringe spacing, d_1 and d_2 are the lattice spacings of the {220} matrix planes and the reflecting precipitate planes respectively, γ is the angle of rotation of the scattering precipitate planes

---

*The moiré fringes cannot be detected in the low magnification print in Fig. 10a, they are, however, easily detected on the photographic plate.

with respect to the matrix reflection, and ϕ is the observed angle between the moiré fringes and the direction normal to the matrix scattering vector. D = 55 Å and d_1 = 1.92 Å (cos γ=1), this gives d_2 = 1.86 or 1.99 Å. As the precipitate reflection is on the inside of the matrix spot d_2 = 1.99 Å represent the precipitate lattice spacing. This value is in excellent agreement with the results calculated from the diffraction pattern; 2.00±0.01 Å. The majority of the observed moiré patterns were oriented normal to the matrix scattering vector, corresponding to $\gamma = 0$. For the fringes with $\phi \neq 0$ all observed cases gave $\gamma < 1°$.

The diffraction patterns in Fig. 10 demonstrate that in the (111) matrix plane, crystallographic directions in the precipitates and the matrix coincide. This epitaxy in the (111) plane may involve a precipitate lattice belonging to either the cubic, the tetragonal or the hexagonal system. Diffraction analysis of colonies in other foil orientation may solve this selection problem. Figure 11 shows a colony consisting of three 110 colony arms marked A, B, and C, in a (110) foil. The arm A is parallel to the (110) foil surface and the arms B and C are on (011) planes. The stereographic projection in Fig. 11 shows the orientation of the different colony branches in the matrix. The strong precipitate contrast in the $[\bar{2}\bar{2}0]$ dark field image is assumed to be due to a precipitate reflection close to the $[2\bar{2}0]$ matric reflection. Unfortunately the selected area diffraction pattern obtained from this configuration was to thin for reproduction. The plate, however, shows extra reflections close to, and in the direction of the $[\bar{2}20]$ and the $[\bar{2}24]$ matrix reflections. The corresponding lattice spacings are 2.00±0.01 Å and 1.16 ± 0.01 Å respectively. Note the strong precipitate contrast in all the three colony arms in the $\bar{2}20$ dark field image, Fig. 11.

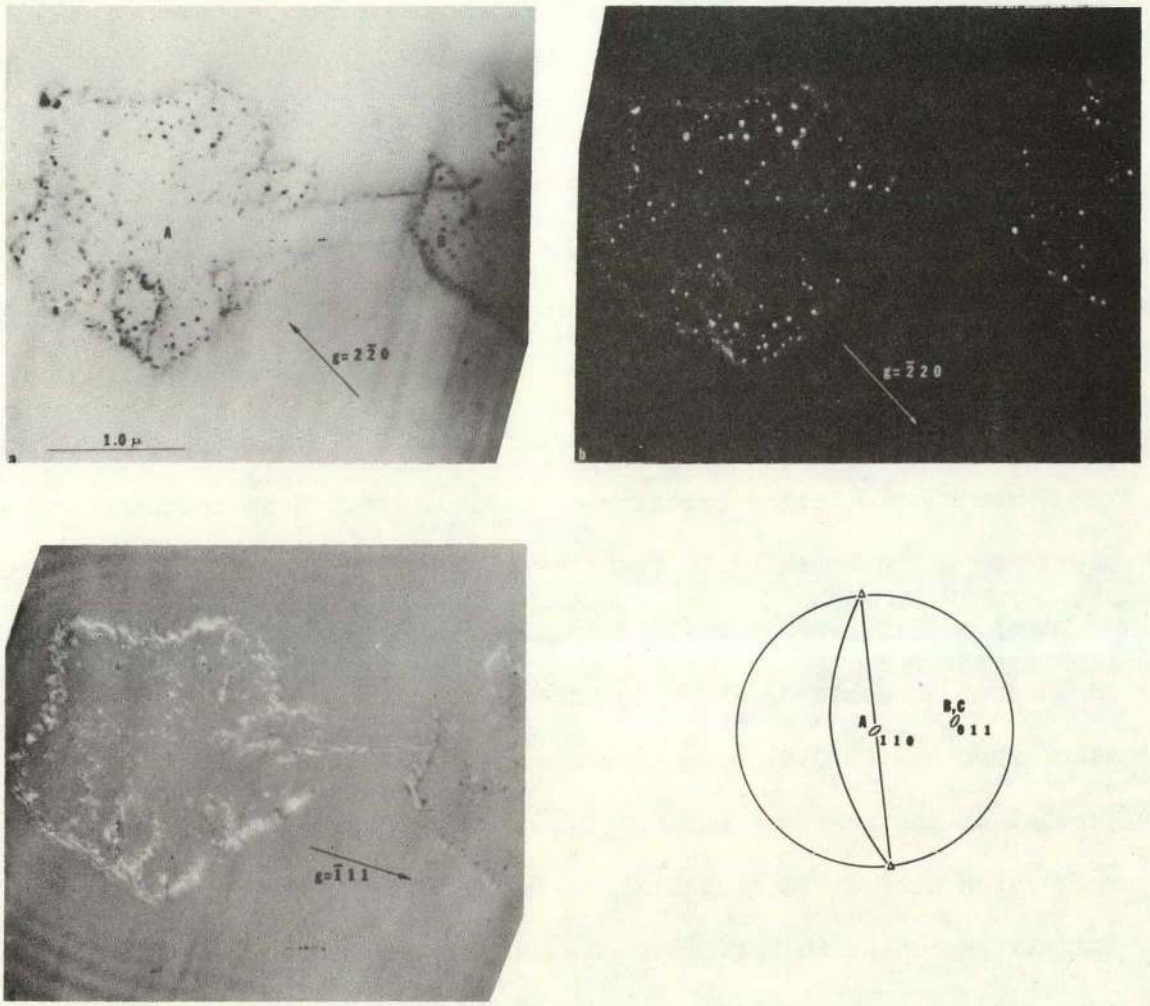

XBB 706-2834

Fig. 11. (650 kV, T_h = 924°C, t_h = 10 min, Q = 8°C/sec) ⟨110⟩ type arms in a (110) foil. (a) Bright field image, the orientation of the arms A, B and C is shown in the stereographic projection. (b and c) Dark field images.

Precipitates belonging to ⟨100⟩ type colony arms

Precipitates belonging to the ⟨100⟩ type arms show a more complicated orientation relationship with the matrix. Figures 12 to 14 show [100] arms in (110) and (111) foils. In each of these cases the orientation of the foil is such as to bring one crystallographic direction in the precipitates into strong diffracting condition. Figure 12 presents a [001] arm, edge on in a (110) foil. One strong precipitate reflection appears in the diffraction pattern (Fig. 12). This spot is located in a direction at an angle of 60° from the $[\bar{1}10]$ matrix direction. The extra spot corresponds to a precipitate lattice spacing of 2.00±0.01 Å. Note how the precipitates lights up in the dark field image of this reflection, Fig. 12b. Figure 13 gives a [010] arm in a (110) foil. One extra diffraction spot is located at an angle of 77° from the $[1\bar{1}\bar{1}]$ matrix direction. This spot also gives a 2.00±0.01 Å lattice spacing. Note that only the precipitates located on the branches in the $[10\bar{1}]$ direction light up in the precipitate reflection dark field image, Fig. 13b. A [001] colony arm in a (111) foil is presented in Fig. 14. A strong precipitate reflection appears in the $[22\bar{4}]$ matrix direction. This reflection corresponds to a precipitate lattice spacing of 1.41±0.01 Å.

Structure analysis

In order to identify the precipitating phase, the observed precipitate lattice spacings, i.e., 2.00±0.01 Å, 1.41±0.01 Å and 1.16±0.01 Å were checked out with the lattice parameters of all the listed silicides and silicon compounds in the ASTM file. This search selected the cubic α-Fe_3Si phase. The unit cube dimension in the iron silicide lattice is, $a = 5.655$ Å.[14] A fully ordered α-Fe_3Si unit cell, DO_3 structure, is

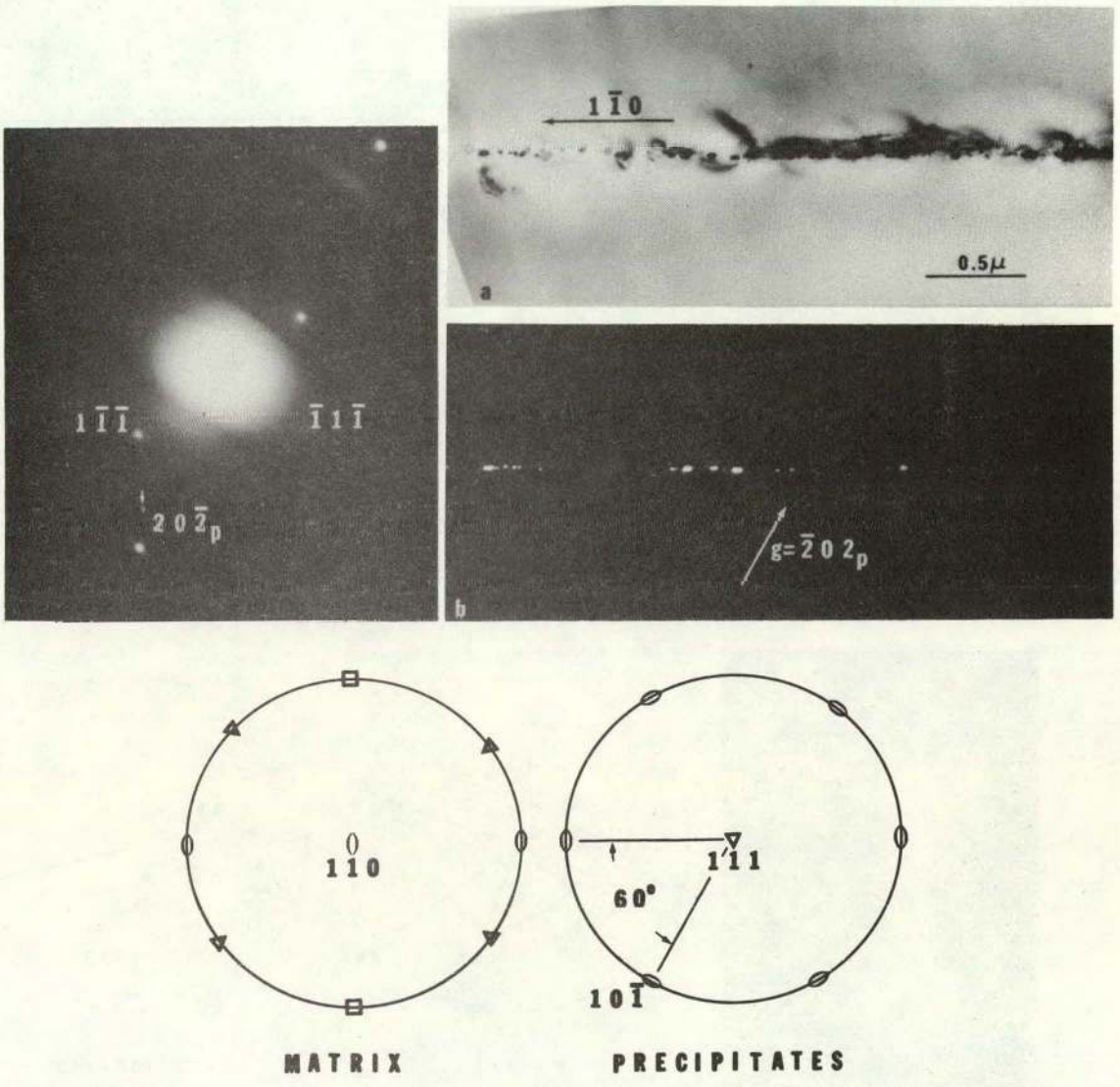

XBB 707-3133

Fig. 12. (650 kV, T_h = 976°C, t_h = 10 min, Q = 8°C/sec) A [001] colony arm seen edge on in a (110) foil. (a) Bright field image. (b) Dark field precipitate reflection image. The matrix and precipitate orientations are given by the stereographic projections.

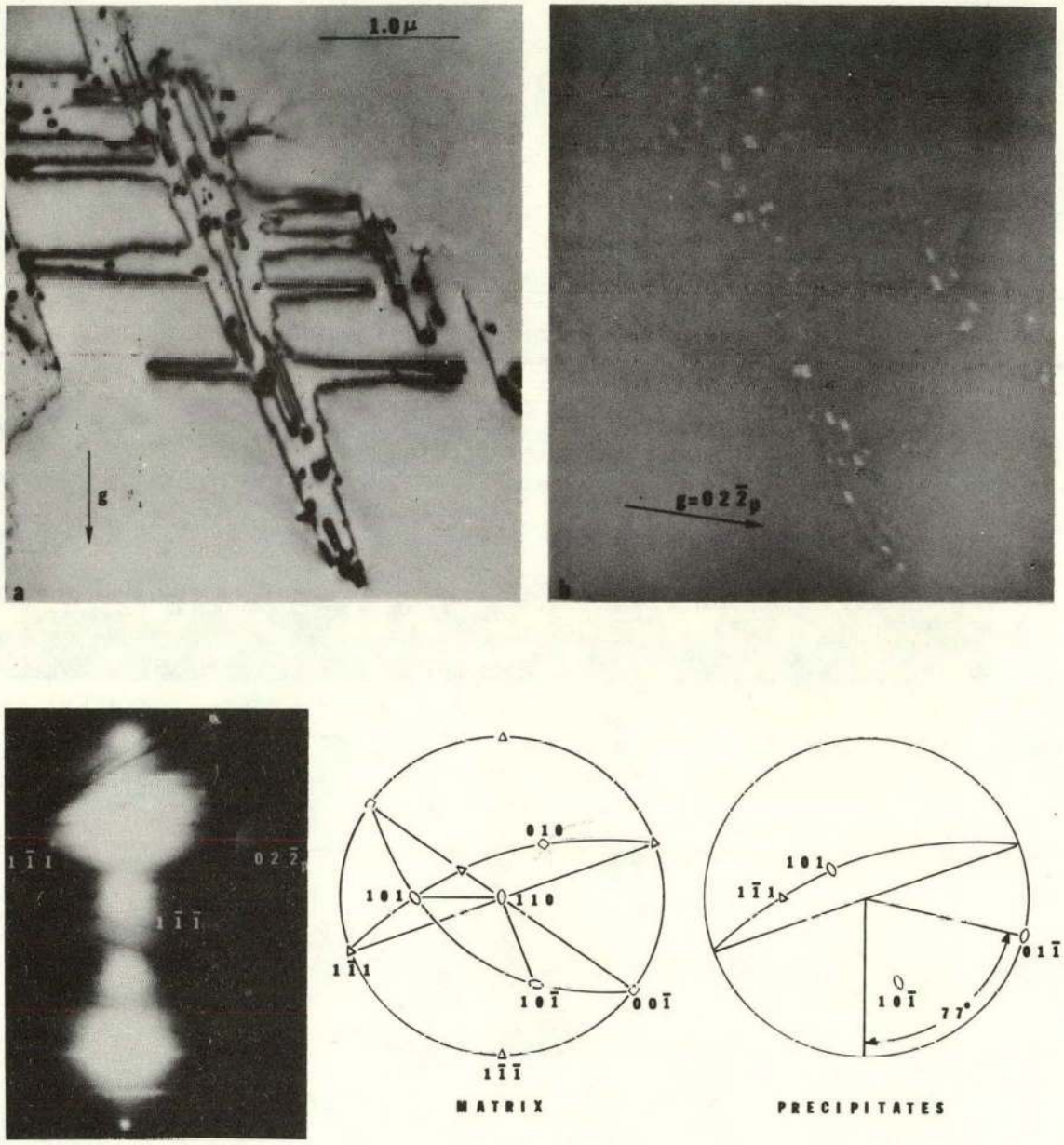

XBB 706-2833

Fig. 13. (650 kV, T_h = 976°C, t_h = 10 min, Q = 8°C/sec) A [010] colony arm in a ($\bar{1}$10) foil. (a) Bright field reflection (b) Dark field precipitate reflection image. The (02$\bar{2}$) precipitate reflection can easily be seen in the diffraction pattern. The stereogrpahic projections give the orientation of the matrix and the precipitate lattices.

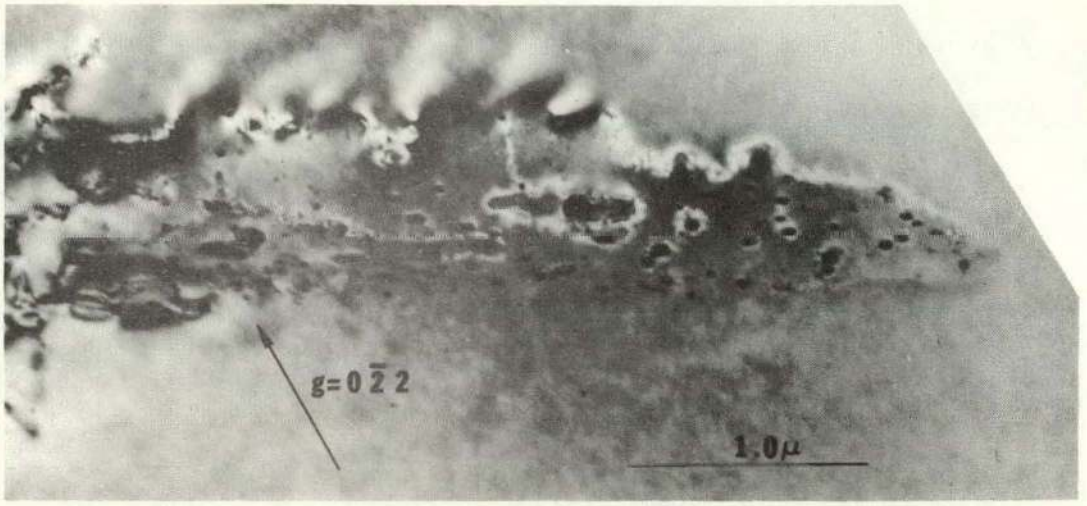

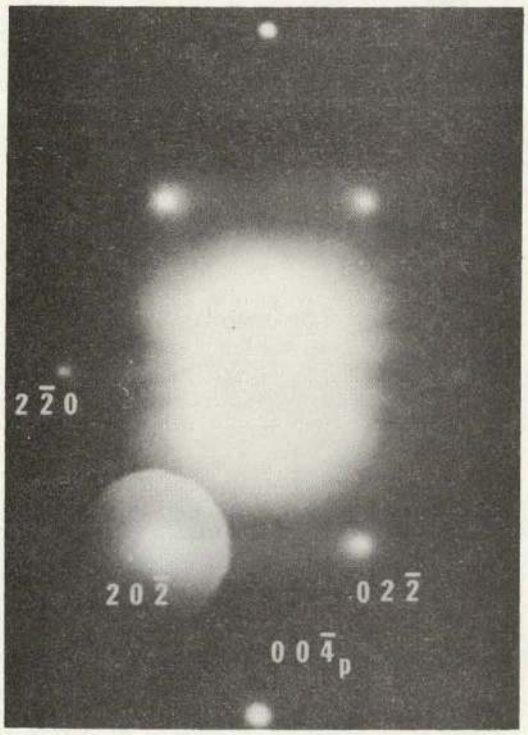

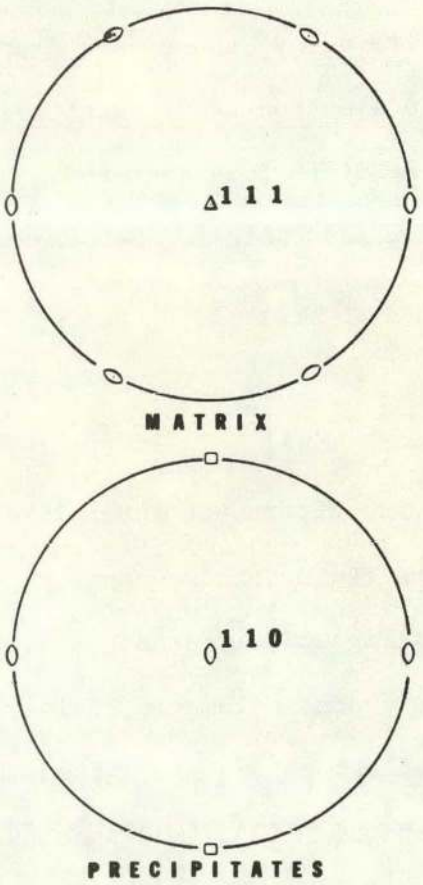

XBB 706-2832

Fig. 14. (650 kV, T_h = 879°C, t_h = 10 min, Q = 8°C/sec) A [001] colony arm in a (111) foil. A strong (00$\bar{4}$) precipitate reflection can be seen in the diffraction pattern. The orientation of the matrix and the precipitates is given by the stereographic projections.

presented in Fig. 15, the cell contains 16 atoms, 12 iron and 4 silicon atoms.

In order to interpret the electron diffraction experiments the structure factor for different α-Fe_3Si reflections have been calculated. The calculation is based upon the assumptions that the α-Fe_3Si phase is fully ordered* and of stoichiometric composition. T he structure factor for a given (hkℓ) reflection can be written.[17]

$$F_{hk\ell} = \sum_i f_i(\theta)\,\mathrm{Exp}{-2}\,\pi i(hu_i + kv_i + \ell w_i) \qquad (3.2)$$

where u_i, v_i and w_i are fractional coordinates of atom i, and $f_i(\theta)$ is the electron atomic scattering amplitude for atom i. The DO_3 structure of α-Fe_3Si is face centered, thus the structure factor will be zero for planes of mixed indices. For the other various special cases Eq. (3.2) gives

$|F_{hk\ell}|^2 = 16[f_{Fe}-f_{Si}]$ when (h+k+ℓ) is odd or an odd multiple of 2.

$|F_{hk\ell}|^2 = 16[3\,f_{Fe}-f_{Si}]$ when (h+k+ℓ) is an even multiple of 2.

As the diffracted intensities are proportional to the square of the structure factor, this quantity is given in the above equations. $|F_{hk\ell}|^2$ for a series of different reflections are presented in Table 3.1, third column. The second column in Table 3.1 gives the α-Fe_3Si lattice parameters. In the last column are listed the observed precipitate reflections. Note that the [220], [400] and [422] iron silicide reflections have a substantially higher value for $|F_{hk\ell}|^2$ than the other reflections.

---

*The α-Fe_3Si phase of nearly stoichiometric composition is completely ordered for all temperatures below the melting point.[15,16] For temperatures below 1000°C the structure is fully ordered when the silicon content exceeds about 15 atomic percent. The ordering is reported to be extremely rapid.[16]

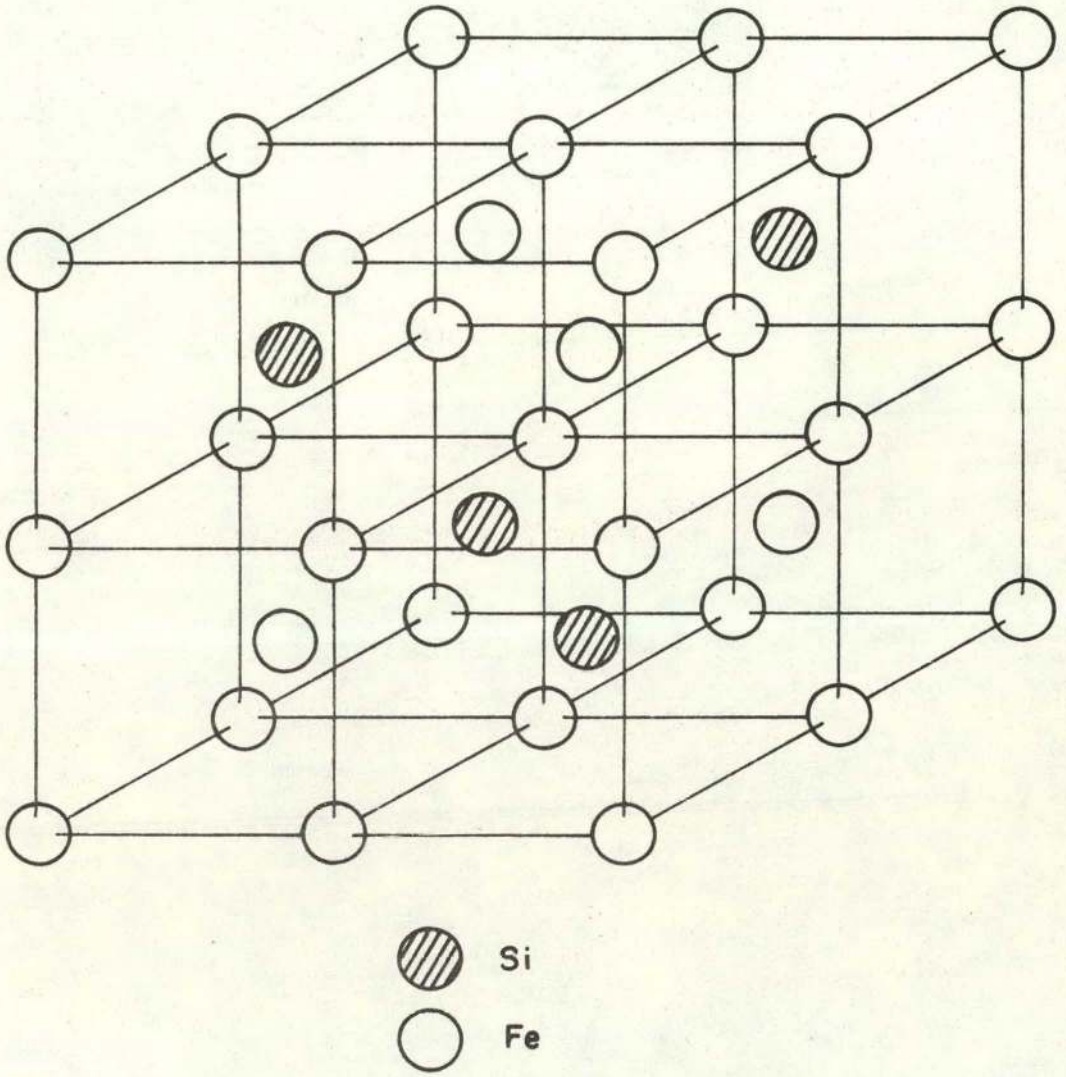

XBL 707-1560

Fig. 15. The crystal structure of α-Fe_3Si.

Table 3.1. The lattice spacings for different crystallographic directions in the cubic α-Fe_3Si structure are given in column 2. The square of the structure factor is given in column 3, and the observed precipitate reflections are listed in the last column.

(hkℓ) Fe_3Si	$d_{hk\ell}$[Å] Fe_3Si	$[F_{hk\ell}]^2$[Å^2] Fe_3Si	Observed Precipitation reflections [Å]
111	3.26	16	
200	2.83	15	
220	2.00	1840	2.00
311	1.71	13	
222	1.63	13	
400	1.41	920	1.41
422	1.16	560	1.16

Although three reflections are too few for a complete structure analysis, it is interesting to note that the observed three reflections are the only ones with reasonably high structrue factors, i.e. only the (220), (400), and (422) reflections, Table 3.1. A complete structure analysis would require a systematic examination of precipitates in a series of foil orientations. The present investigation includes only two orientations, i.e. (111) and (110). The (110) foils should, however, be the most informative.

No other silicide or silicon compound, listed in the ASTM file, fit the observed d-values. Thus it is concluded that the precipitating atoms most probably are iron atoms, and the precipitating phase α-Fe_3Si. According to the iron silicon phase-diagram the α-phase is stable only in the iron rich part of the diagram, and it follows that in this case the α-phase is in a metastable form.

3.4.2 Orientation Relationship

The diffraction analysis presented in the foregoing section shows that in the case of the precipitates belonging to the $\langle 110 \rangle$ colony arms, the two cubic lattices involved, i.e. the DO_3 structure of the precipitates and the diamond structure of the matrix, both have the same orientation.

For the case of the precipitates belonging to the $\langle 100 \rangle$ colony arms the three precipitate reflections in Figs. 12 to 14 define the complete orientation relationship between these precipitates and the matrix as follows:

$$(112)_p \quad || \quad (001)_m$$

$$[110]_p \quad || \quad [110]_m \text{ or } [1\bar{1}0]_m$$

where p and m indicate precipitate and matrix respectively. The $[1\bar{1}0]_p$ direction can be aligned with either of the two ⟨110⟩ directions in the (001) matrix plane. The direction selected will be given by the direction of the branch on which the precipitate is located. Thus, in a ⟨100⟩ type colony arm, precipitates on orthogonal ⟨110⟩ branches will have lattice orientations rotated 90° with respect to each other. This explains why only the $[10\bar{1}]$ precipitates contributed to the precipitate dark field contrast in Fig. 13.

This orientation relationship is illustrated in the stereographic projections in each of the Figs. 12 to 14. A ⟨100⟩ colony arm, seen edge on, in a (110) foil, will according to the above orientation relationship have the (111) precipitate planes parallel to the (110) matrix surface. This gives a $[20\bar{2}]$ precipitate reflection 60° from the $[\bar{2}20]$ matrix direction as observed in Fig. 12. For precipitates located on $[10\bar{1}]$ branches in a (110) foil, Fig. 13, the $[02\bar{2}]$ precipitate direction will appear in the (110) matrix plane 77° from the $[1\bar{1}\bar{1}]$ matrix reflection. This is in agreement with observations. Finally for the (001), $[\bar{1}10]$ precipitates in Fig. 14, the (110) precipitate planes will be parallel to the (111) foil surface so that $[00\bar{1}]_p \| [11\bar{2}]_m$. This is also consistent with the diffraction spots that were observed.

3.4.3 Morphology

Precipitates belonging to ⟨110⟩ type colony arms

Figures 16a and b show details from ⟨110⟩ colony arms in (111) and (110) foils. In both micrographs the precipitate images have a hexagonal form. In the (111) foil, Fig. 16a, the hexagonal sides are normal to ⟨112⟩ directions and in the (110) foil they are normal to ⟨111⟩ and ⟨100⟩ directions, Fig. 16b. The hexagonal forms in these two different projections

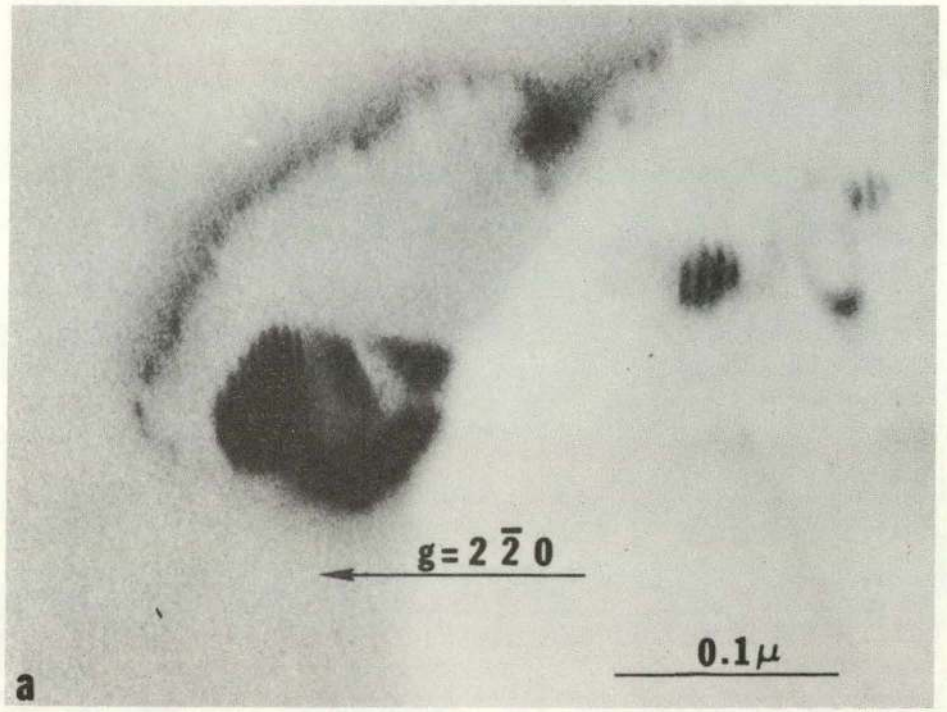

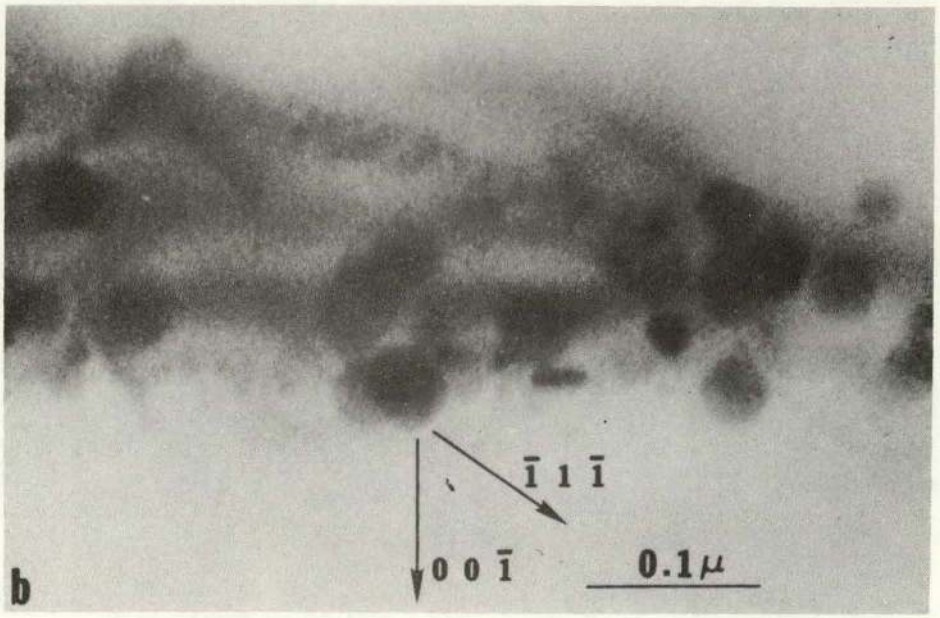

XBB 706-2836

Fig. 16. (650 kV, a; T_h = 820°C, t_h = 10 min, Q = 7°C/sec b; T_h = 976°C, t_h = 10 min, Q = 8°C/sec). (a) Precipitates belonging to a ⟨110⟩ arm in a (111) foil. (b) Precipitates on a ⟨110⟩ arm in a (110) foil.

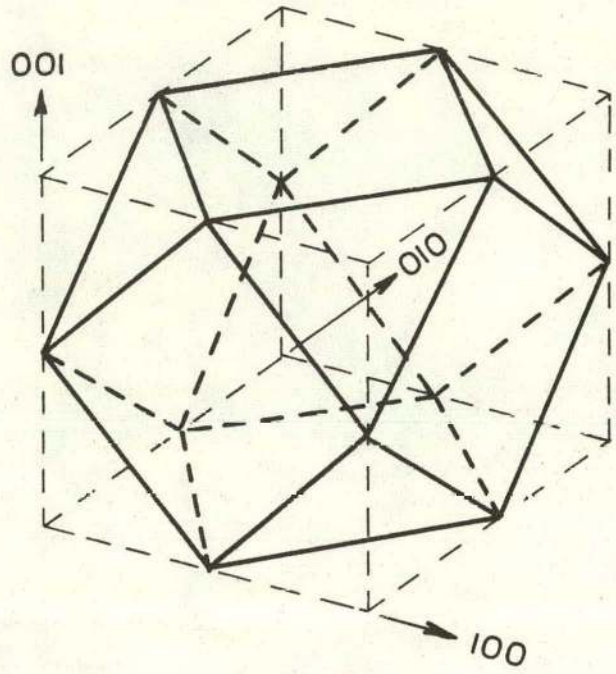

(a)

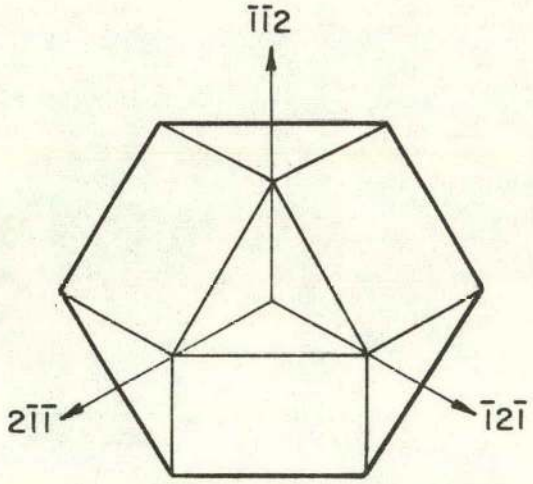

111 PROJECTION

(b)

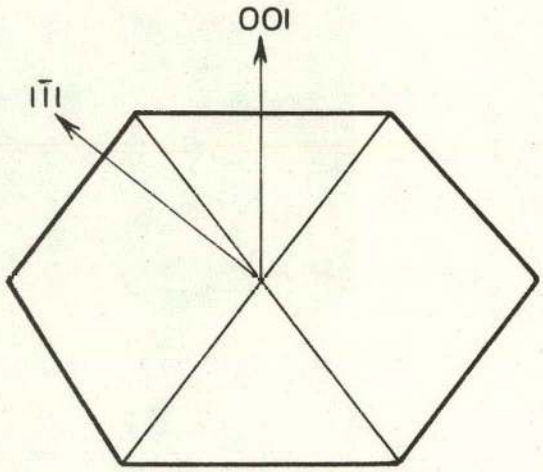

110 PROJECTION

(c)

XBL 707-1552

Fig. 17. (a) The geometrical shape of the ⟨110⟩ type precipitates. (b and c) (111) and (110) projections of the figure a.

suggest, together with the characteristic change in the orientation of the projected precipitate-matrix interface, that the precipitates have a three-dimensional volumetric morphology, rather than being of a plate shape. These two projections suggest that the basic geometrical shape of the precipitates is a truncated cube with $\langle 100 \rangle$ and $\langle 111 \rangle$ faces as shown in Fig. 17a. The [111] and [110] projections of this cube, Fig. 17b and c, correspond to the precipitate images in the (111) and (110) foils respectively (Fig. 16a and b).

Precipitates belonging to $\langle 100 \rangle$ type colony arms

Figure 18a and b show details from $\langle 100 \rangle$ colony arms in (110) foils. The precipitates in Fig. 18a are of the kind (001), [110], that is, precipitates on $[1\bar{1}0]$ dendrite branches belonging to a (001) colony arm seen edge on in a (110) foil. Figure 18b shows (010), $[10\bar{1}]$ precipitates. If the geometry of Fig. 17a is extended along one of the $\langle 110 \rangle$ axis, the resulting geometrical shape will be like Fig. 19a. This geometry describes the $\langle 100 \rangle$ type precipitates. (The crystallographic directions in Fig. 19 refer to matrix orientations.) Figures 19b and c are projections of Fig. 19a in orientations corresponding to the precipitates in Figs. 18a and b. These predicted images fit the observed ones very well.

3.4.4 The Precipitate Strain Field

The precipitates in the $\langle 110 \rangle$ arm in Fig. 26 have virtually no elastic strain contrast associated with them. Other micrographs, however, show precipitates belonging to $\langle 110 \rangle$ type configurations exhibiting strong strain contrast, Fig. 20. Close examination of the precipitate image in Fig. 20 show a line of no contrast normal to the direction of the scattering vector (g-vector). Note how this line of no contrast rotates with

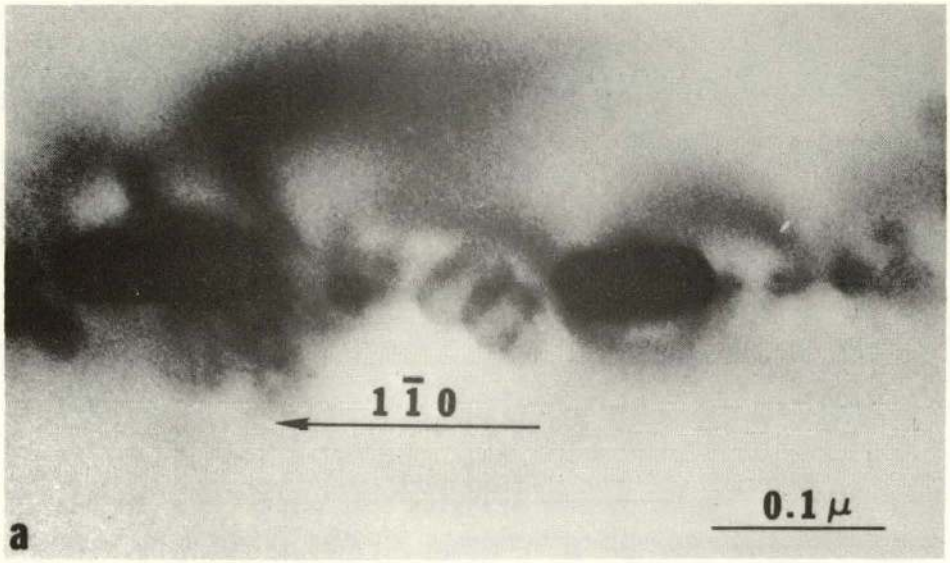

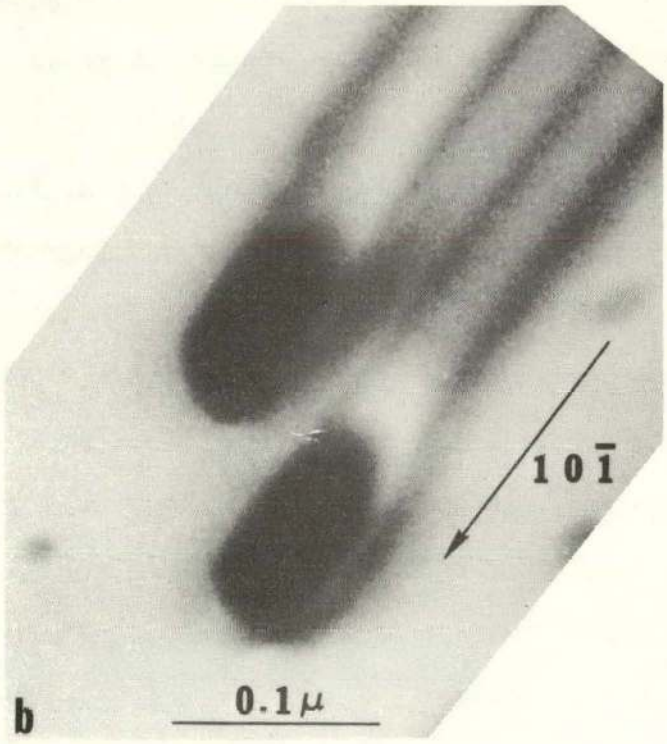

XBB 706-2838

Fig. 18. (650 kV, T_h = 976°C, t_h = 10 min, Q = 8°C/sec)
(a) Precipitates on a [001] arm in a (110) foil.
(b) Precipitates on a [010] arm in a (110) foil.

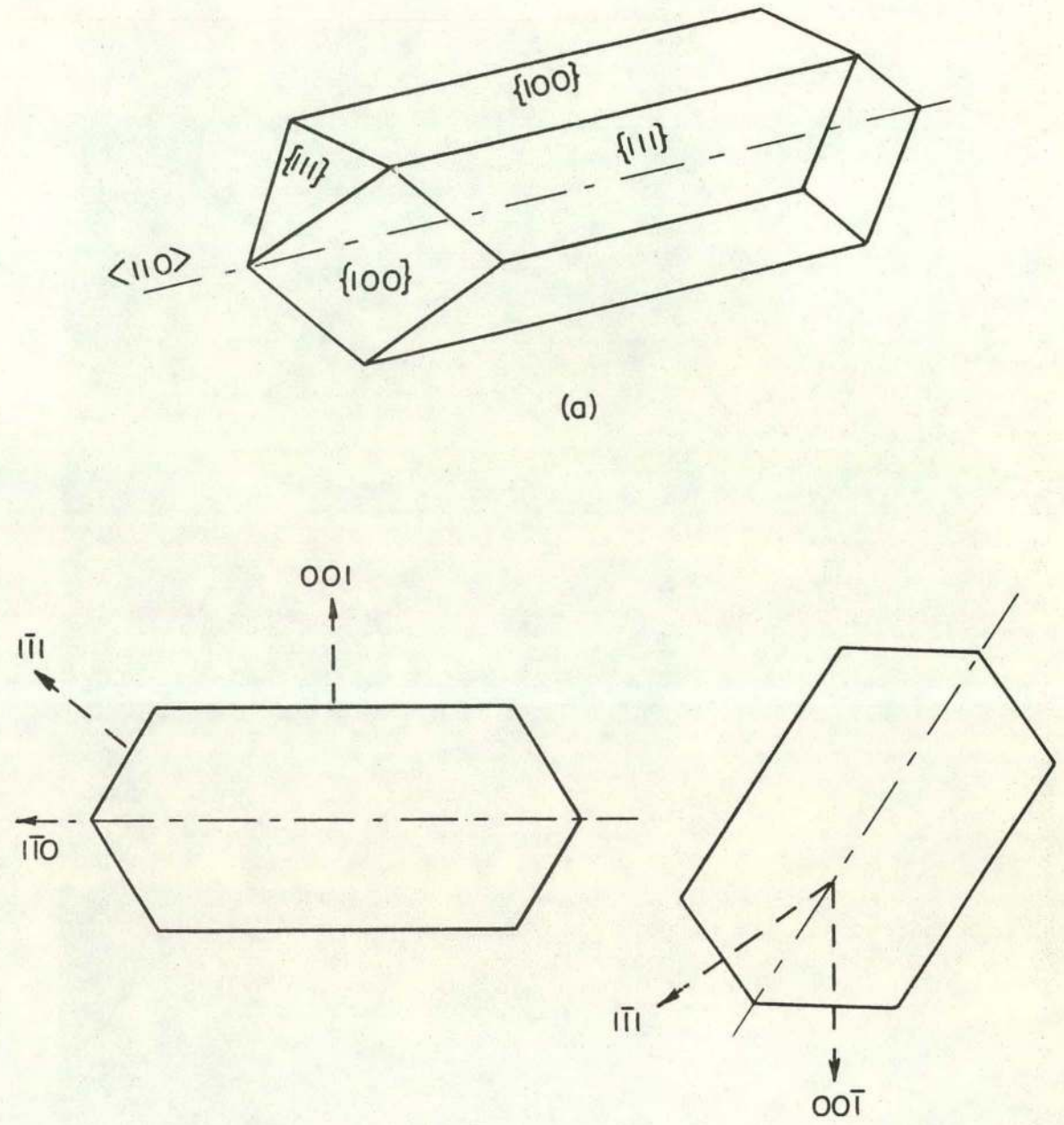

Fig. 19. (a) The geometrical shape of the precipitates belonging to the ⟨100⟩ colony arms. (b and c) (110) projections of ⟨100⟩ precipitates with its long axis in the [1$\bar{1}$0] and [10$\bar{1}$] directions.

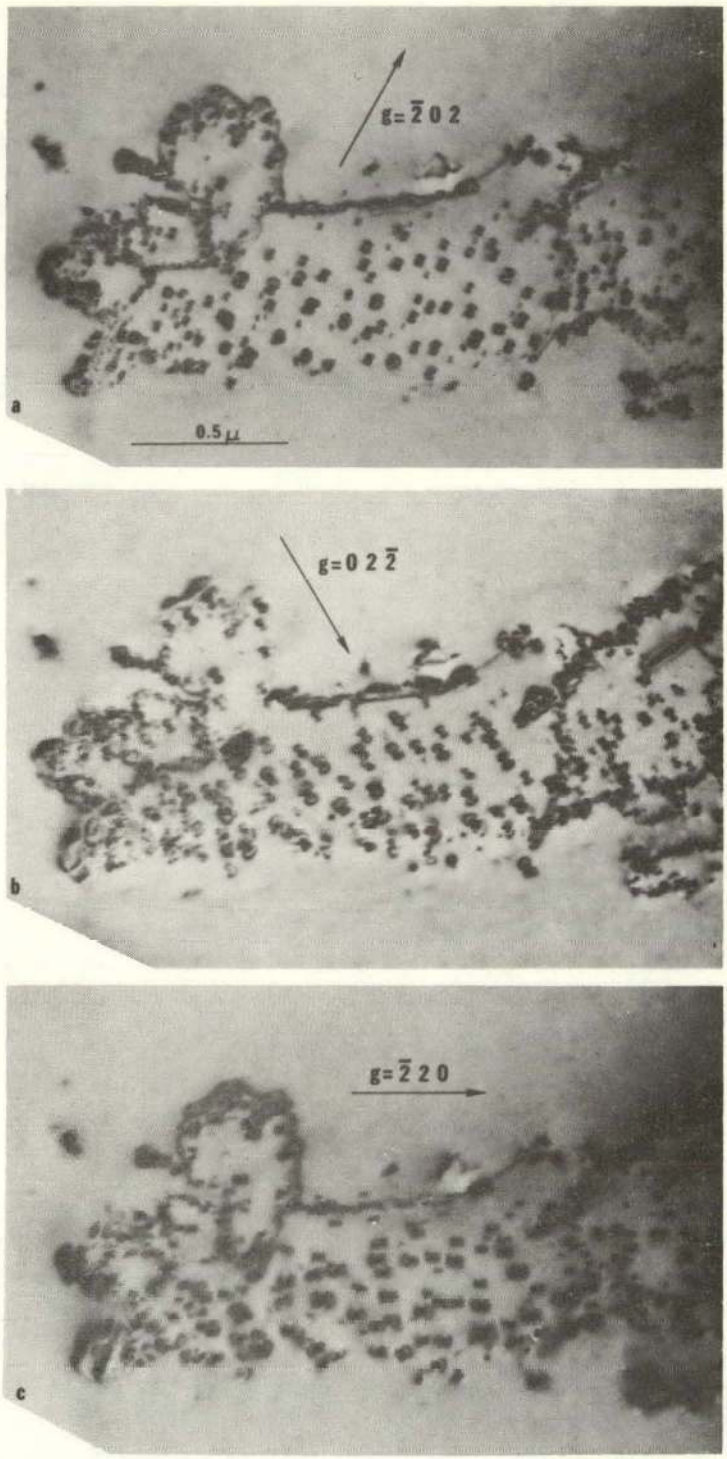

XBB 706-2850

Fig. 20. Two beam bright field images of a ⟨110⟩ type arm in a (111) foil. Note how the line of no contrast in the precipitate image rotates with the $\vec{g}$-vector.

the direction of g. This contrast effect indicates that the precipitates are surrounded by a spherical stress field.[18] This type of stress field was expected, as the cube-cube orientation relationship, Section 3.4.2, between the matrix and the precipitates together with the volumetric morphology of the precipitates suggest the generation of a strain field of spherical symmetry.

The stress field surrounding the precipitates in the (001) configuration in Fig. 21 give rise to a nearly circular image when the g-vector is in the $(20\bar{2})$ or $(0\bar{2}2)$ direction. No strain contrast appears for the $(\bar{2}20)$ g-vector contained in the (001) plane of the configuration. As will be discussed in detail in Section 3.5, this contrast variation is consistent with a stress field similar to that surrounding an edge dislocation loop. The contrast analysis given in Section 3.5, further shows that the precipitate stress field is compressive in nature. This stress field suggests a plate-shaped morphology of the precipitates. However, as demonstrated in the foregoing section, the precipitates have a volumetric shape. The strong 100 directional character of this strain field is most probably caused by the special orientation relationship between precipitates and matrix, i.e. $(112)_p||(001)_m$.

To summarize these two paragraphs: The precipitates on $\langle 110 \rangle$ type arms give rise to a strain field of spherical symmetry. The $\langle 100 \rangle$ arm precipitates have a strain field analogous to that of an interstitial dislocation loop with Burgers vector perpendicular to (100).

Some of the strain energy is within the precipitates. For the smaller precipitates this can cause a measurable change in the lattice parameters. This change can be detected in the moiré fringe spacing. The two smaller

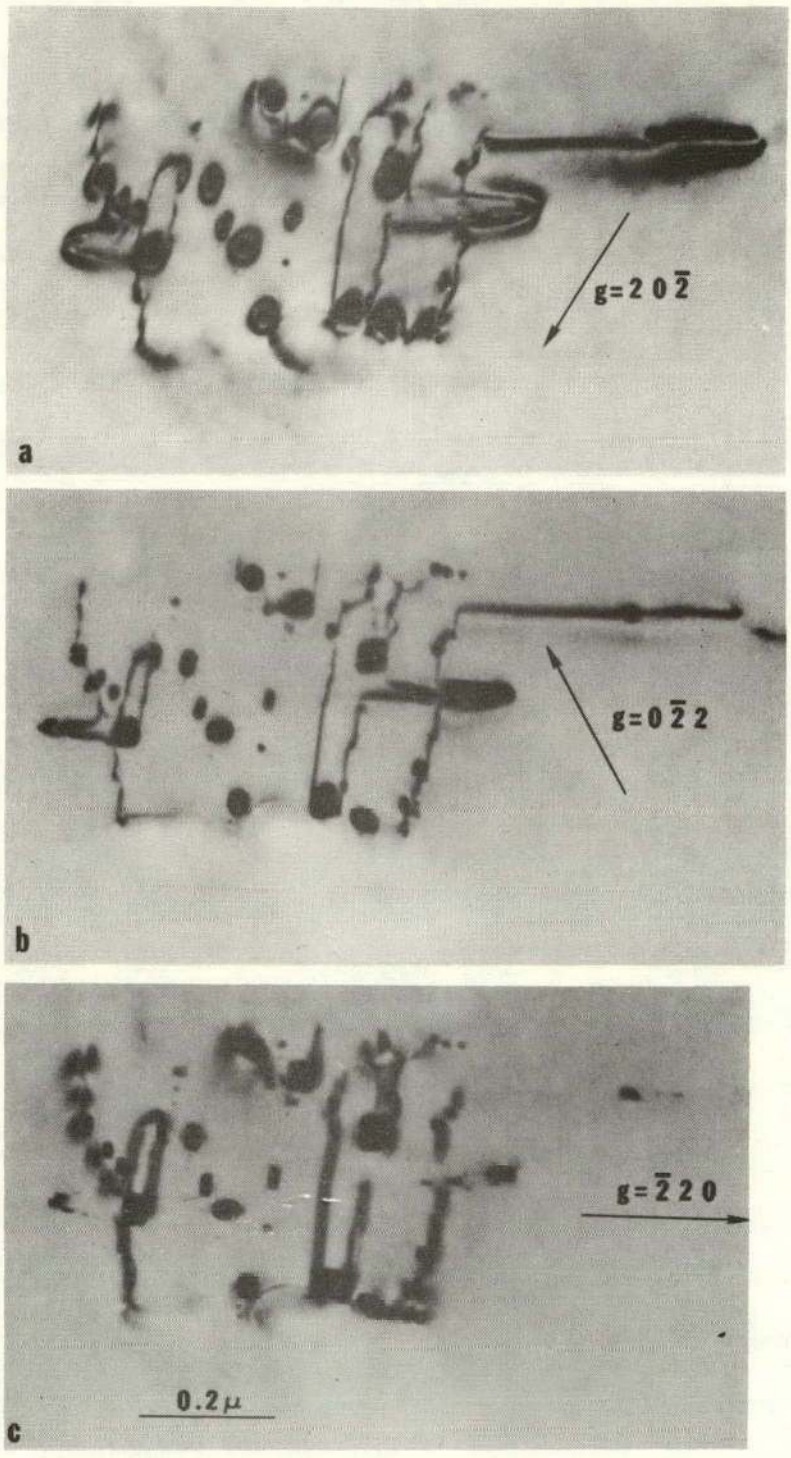

XBB 706-2845

Fig. 21. (100 kV, T_h = 882°C, t_h = 10 min, Q = 6°C/sec) Two beam bright field micrographs of a [001] arm in a (111) foil. (a and b) The precipitates are surrounded by a nearly circular strain contrast image. (c) No precipitate strain contrast.

precipitates in Fig. 16a have a moiré fringe spacing of 80 Å compared 55 Å for the large precipitates. By inserting D = 80 Å in Eq. (3.1) a lattice parameter of 1.97 Å is obtained. Thus, there is a difference in the spacing of the ⟨220⟩ planes between the small and the large precipitates of about 0.02 Å, or a relative change of about 1%.

3.4.5 Distribution of Precipitates

In Section 3.3 the ⟨110⟩ type arms were characterized as a coplanar arrangement of evenly distributed precipitates, bounded by a dislocation loop. The transmission electron micrographs show that this statement is true in general, however, there are some interesting irregularities in the distribution of the precipitates within ⟨110⟩ colony arms. Long precipitation free zones are frequently observed within the {110} planar arrangements, Figs. 22a and b. These depleted zones are always elongated in the ⟨110⟩ directions and there is always a large precipitate at the end of the zone nearest to the enveloping dislocation. Note that two new dislocation loops have been nucleated from the large precipitate in Fig. 22a.

3.5 Dislocation Structure

As outlined in a previous Section (3.3) each arm of a colony consists of a nearly coplanar group of precipitates enveloped by a dislocation loop. The Burgers vector for dislocations in ⟨110⟩ type arms can be found from Figs. 23a to c, representing three 220 two-beam reflections from a (111) foil. The micrographs show a colony consisting of two arms, A-A and B-B, located on (110) and (011) planes respectively. Note that no dislocation contrast appears in that arm which contains the g-vector. From simple $g \cdot b = 0$ considerations it can be concluded that the dislocations

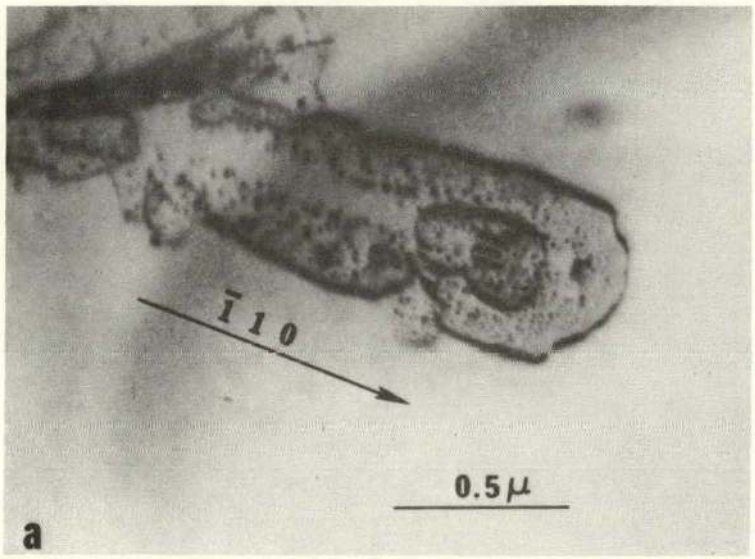

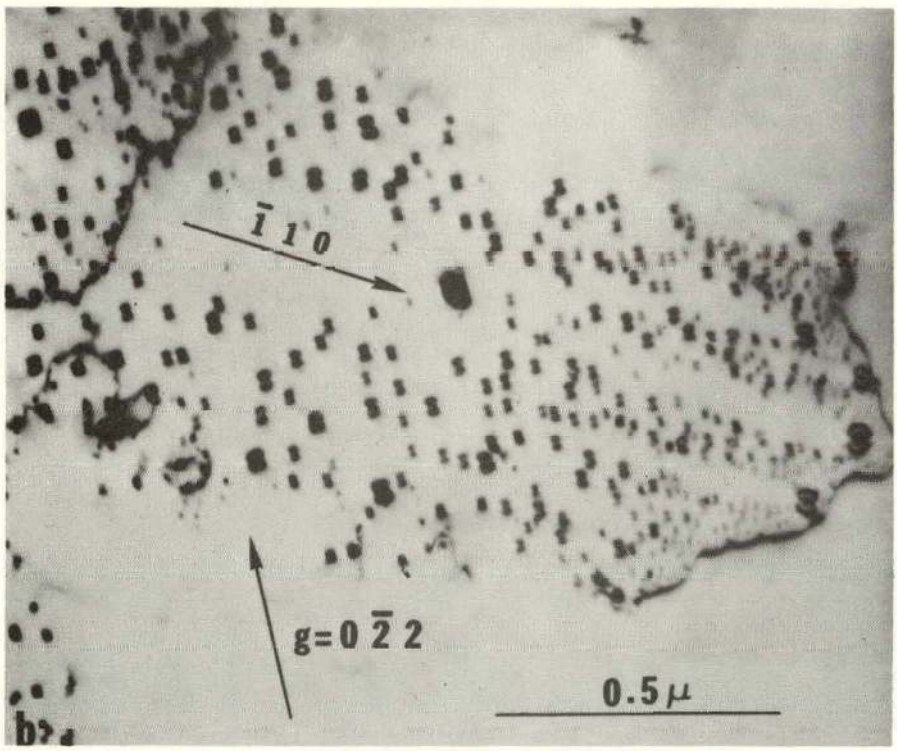

XBB 706-2839

Fig. 22. (100 kV, a; T_h = 974°C, t_h = 10 min, Q = 10°C/sec. b; T_h = 884°C, t_h = 10 min, Q = 22°C/sec) Depleted zones in the ⟨110⟩ type precipitate colony arms.

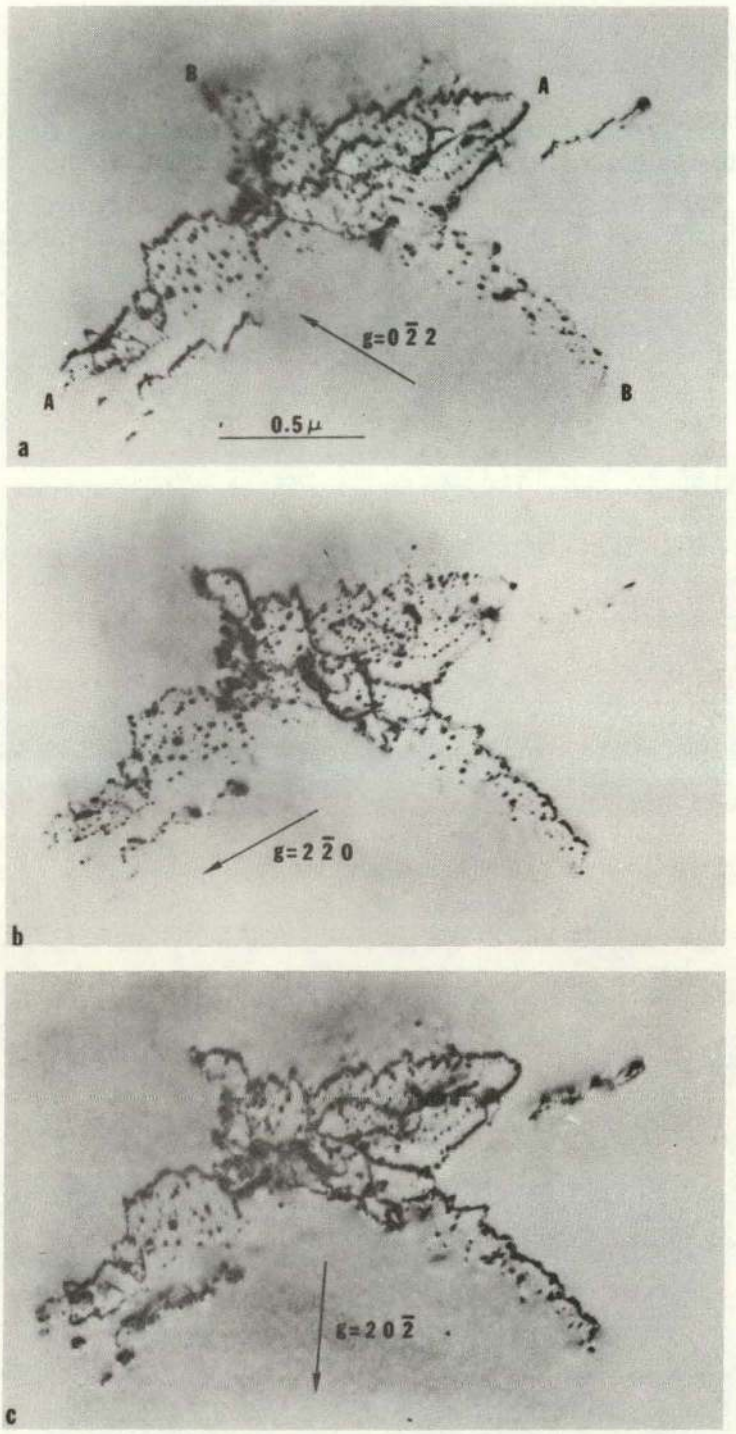

XBB 706-2847

Fig. 23. (100 kV, T_h = 820°C, t_h = 10 min, Q = 10°C/sec) Three two-beam bright field micrographs of two ⟨110⟩ type arms in a (111) foil. The A-A and B-B arms are located on (110) and (011) crystallographic planes respectively. The dislocations are out of contrast in the branch which contains the $\vec{g}$-vector.

in the A-A arm have a [110] Burgers vector and the B-B arm a [011] Burgers vector. Thus the dislocations observed are parts of perfect edge dislocation loops.

Figure 24a to c represent three 220 two beam case micrographs of a (001) precipitate, dislocation congiguration. As the dislocation segments parallel to the g-vector are out of contrast in Fig. 24c, it can be concluded that the dislocations Burgers vector is confined to some direction in the [110] plane. If the dislocations are perfect, i.e., have a a/2 110 Burgers vector, then the only available direction would be [110]. This direction is in the (001) plane of the configuration, consequently the whole dislocation structure would be in a glide orientation with [110] screw dislocation segments. However, as the [110] dislocation segments are not out of contrast in Fig. 24c, b = a/2[110] can be excluded as a possible Burgers vector. Close inspection of the [110] dislocation segments in Fig. 24c shows a double image. This double image is characteristic for an edge dislocation when $g \cdot b = 0$ and is called "residual"contrast.* This"residual"contrast effect is even more pronounced in Fig. 21c. The contrast variation with different reflections in Fig. 24 (and Fig. 21) is thus consistent with an edge dislocation structure. The {100} dislocation configurations have a Burgers vector of the type a ⟨100⟩.

---

*To get a dislocation out of the contrast in a two-beam case the following requirements have to be fulfilled.[19] (1) $g \cdot b = 0$, (2) $g \cdot b \times u = 0$, where g is the scattering vector, b is the Burgers vector of the dislocation and u is a unit vector in the direction of the dislocation line. Thus, contrast from an edge dislocation can occur even if $g \cdot b = 0$. This contrast effect, called"residual"contrast, is characterized by a double image of the dislocation line.

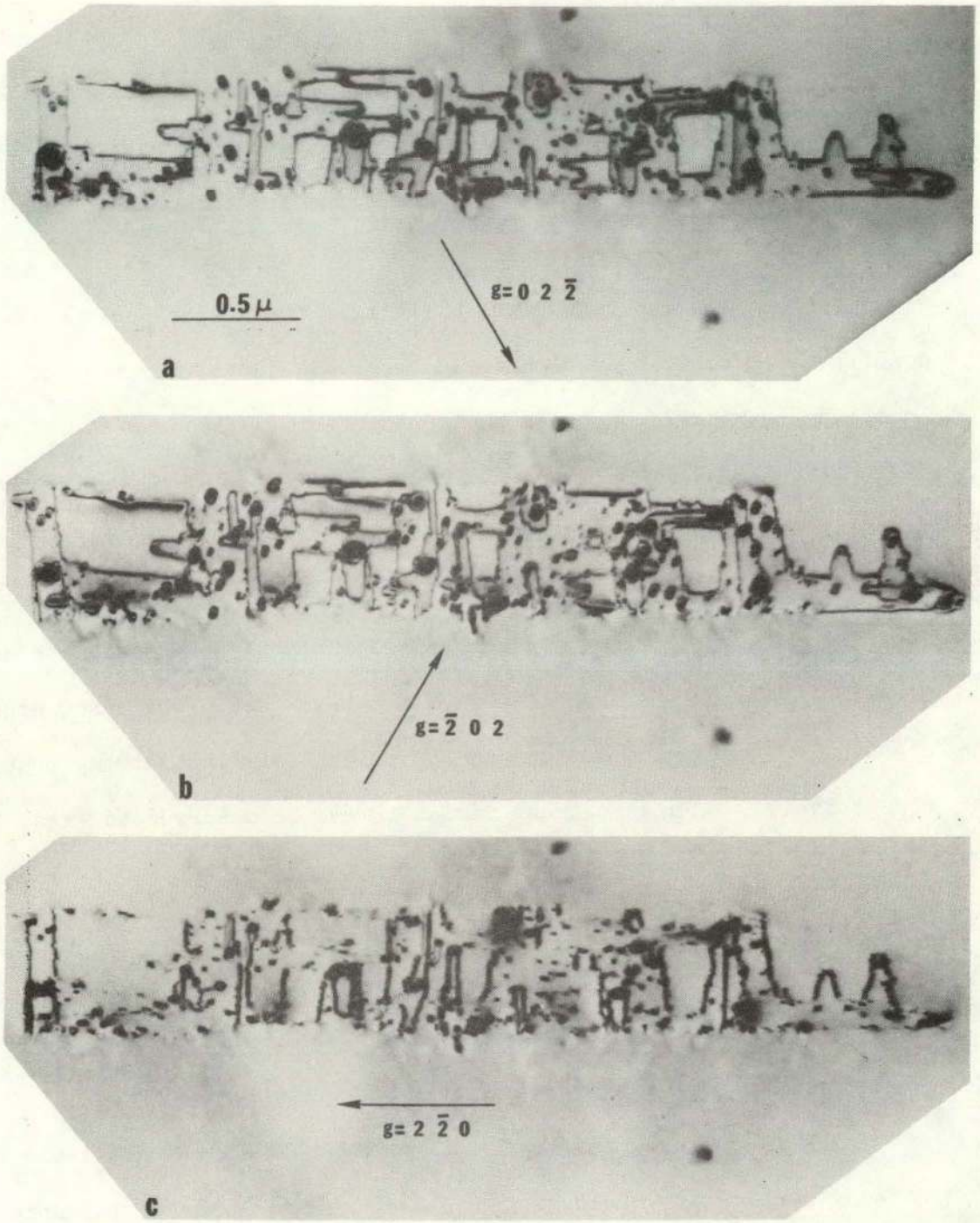

XBB 706-2841

Fig. 24. (100 eV, T_h = 893, t_h = 10 min, Q = 6°C/sec) Two-beam bright field micrographs of a [001] type colony arm in a (111) foil. (a and b) Strong dislocation contrast. (c) The dislocation segments parallel to the [1$\bar{1}$0] direction is out of contrast. Note the double image of the [110] segments.

A very important result related to the nature of the dislocations is that the dislocation loops surrounding the precipitates are all of an interstitial character, i.e. each arm of a colony represents at least two extra planes of silicon atoms. Evidence for this can be obtained from Figs. 25 and 26 representing ⟨100⟩ and ⟨110⟩ type configurations respectively. Changing the sign of s, where s is the deviation from the Bragg condition, in a two beam dark field case will cause the image of a dislocation to switch from one side to the other of the true position of the dislocation line.[20-23] Thus, a dislocation loop will expand or contract by changing the sign of s, while keeping g the same. By knowing the crystallographic plane of the loop this effect can be used to determine if the loop is of interstitial or vacancy type. This slope can also be determined by changing the sign of s in a two beam dark field case, because $s > 0$, $s < 0$ bring the bottom and top of the foil into strong contrast respectively.[24] This contrast variation can be observed in Figs. 25 and 26. Thus, the planar configurations run through the foils as indicated in Figs. 25a and 26a. Knowing this slope of the configurations with respect to the g-vector, and by observing that the branches, marked A in Figs. 24 and 25, shrinks from $s > 0$ to $s < 0$, it can be concluded that the enveloping dislocations are of interstitial character.

In Section 3.4.4 above it was reported that the stress field surrounding precipitates belonging to ⟨100⟩ type arms was of the same type as that of interstitial dislocation loops. This statement is verified by observing that the precipitate images, marked B in Fig. 25, shrinks when s is changed from $s > 0$ to $s < 0$.

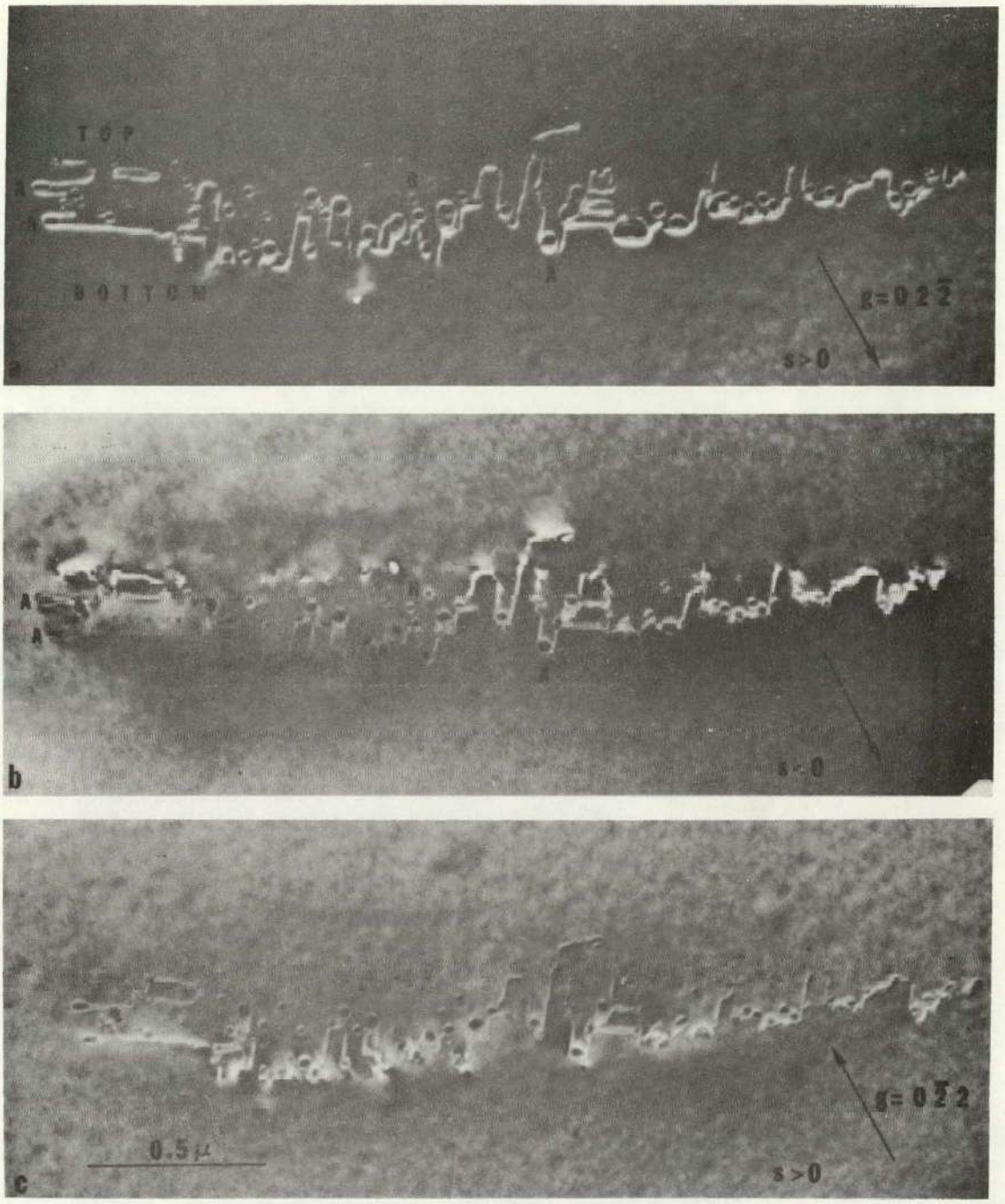

XBB 706-2840

Fig. 25. (100 kV, T_h = 903°C, t_h = 10 min, Q = 6°C/sec) Two-beam dark field images of a [001] arm in a (111) foil. (a and b) The configuration intersects the foil surfaces as indicated by the TOP and BOTTOM signs. Note how the branches marked A shrinks by changing from s > 0 to s < 0. The same change in s brings the bottom and top of the foil into strong contrast respectively.

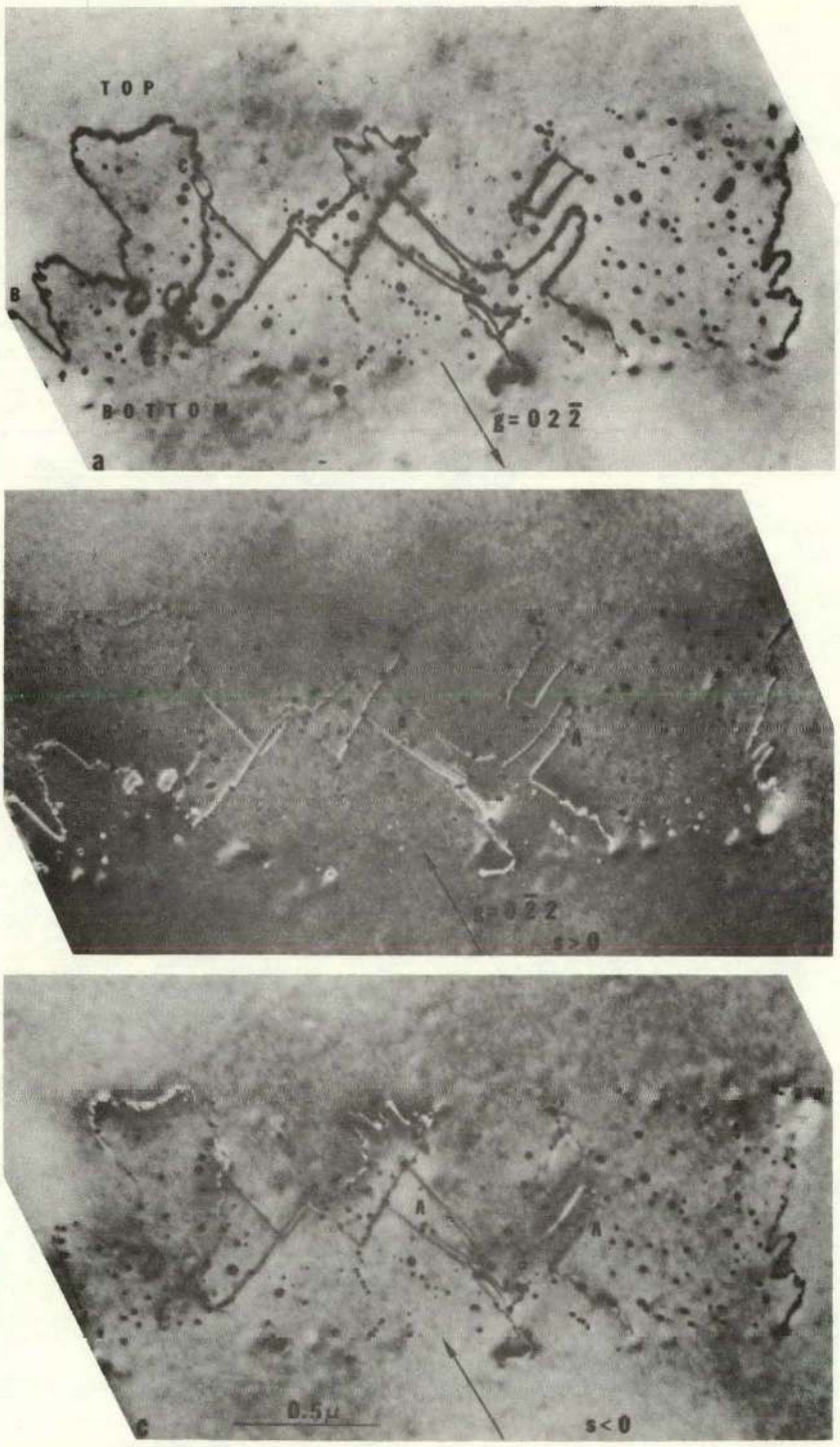

XBB 706-2843

Fig. 26. (100 eV, T_h = 940°C, t_h = 10 min, Q = 4°C/sec) A [110] colony arm in a (111) foil. (a) Bright field image, the configuration intersects the foil surfaces as indicated by the TOP and BOTTOM signs. (b anc c) Two beam dark field images. The branches marked A shrink by changing from s > 0 to s < 0.

It was pointed out during the general description of the colonies in Section 3.3 above that the precipitate arrangements on {110} crystallographic planes, i.e. 110 colony arms, were bounded by nearly circular dislocation loops. Figure 26 shows that irregularities in this dislocation contour may occur, and that long and narrow dislocation protrusions or branches are formed also on {110} planes. In Fig. 25 the branches are aligned in ⟨112⟩ directions.

3.6 Growth of Precipitate Colonies

In order to study the growth of the precipitate colonies a series of specimens were given a heat treatment as indicated by the heavy broken line in Fig. 2; from the holding temperature, T_h, the specimens were cooled cooled at a speed, Q, which is known to give defect clusters. By interrupting thie "normal" cooling by a rapid quench at the temperature T_Q, the specimens should retain the clusters at the stage of development given by this quenching temperature. By choosing an appropriate series of temperatures, T_Q, one should be able to follow the growth of the clusters.

Two series of experiments have been performed. One starting with a holding temperature, T_h, at about 925°C and the other with T_h about 850°C. In both cases the subsequent cooling rate was about 8°C/sec. For different specimens this cooling rate was interrupted at different temperatures, T_Q, selected at 25°C intervals from the holding temperatures down to about 600°C.

It was found that the precipitation started at about 800°C whether the holding temperature was 925°C or 850°C. This is in agreement with the results presented in Section 3.2; that varying the holding temperature in

the range 820°C to 974°C caused no change in precipitate colony sizes. Thus the concentration of the precipitating species corresponds to that given by the solid solubility at about 800°C.

In the early stages of growth the two types of precipitate arms, i.e. ⟨110⟩ and ⟨100⟩ types, have the same general form. Both appear as narrow elongated loops on the {100} planes. However, even in the earliest observed stages the two growth modes exhibit important differences.

3.6.1 Growth of ⟨110⟩ Type Colony Arms

A typical example of a 110 arm at an early stage of development is presented in Fig. 27. This dislocation dipole-precipitate configuration was interrupted in its growth at 773°C. The elongated loop is oriented in the $[01\bar{1}]$ direction. The dislocation is almost out of contrast in the $[1\bar{1}\bar{1}]$ reflection, Fig. 27b, while in strong contrast in the $[2\bar{2}0]$ and [004] reflections; this is consistent with a a/2[101] Burgers vector. Figure 27b shows that the precipitates are aligned as a bead string along the dislocation. At this stage of development only one precipitate has been left inside the part of the half loop contained in the foil.

The transition from this elongated loop configuration into the familiar {110} planar precipitate arrangements is demonstrated in Figs. 28* and 29.

The growth in these two cases was stopped at 725°C and 701°C respectively. In Fig. 28 the initial elongated loop is partially preserved. The sketch in Fig. 28 shows the initial shape of the dislocation loop, broken line; at this stage the whole configuration is located in the (100)

*The unsharp image was caused by a malfunctioning of the objective lense in the Siemens IA microscope.

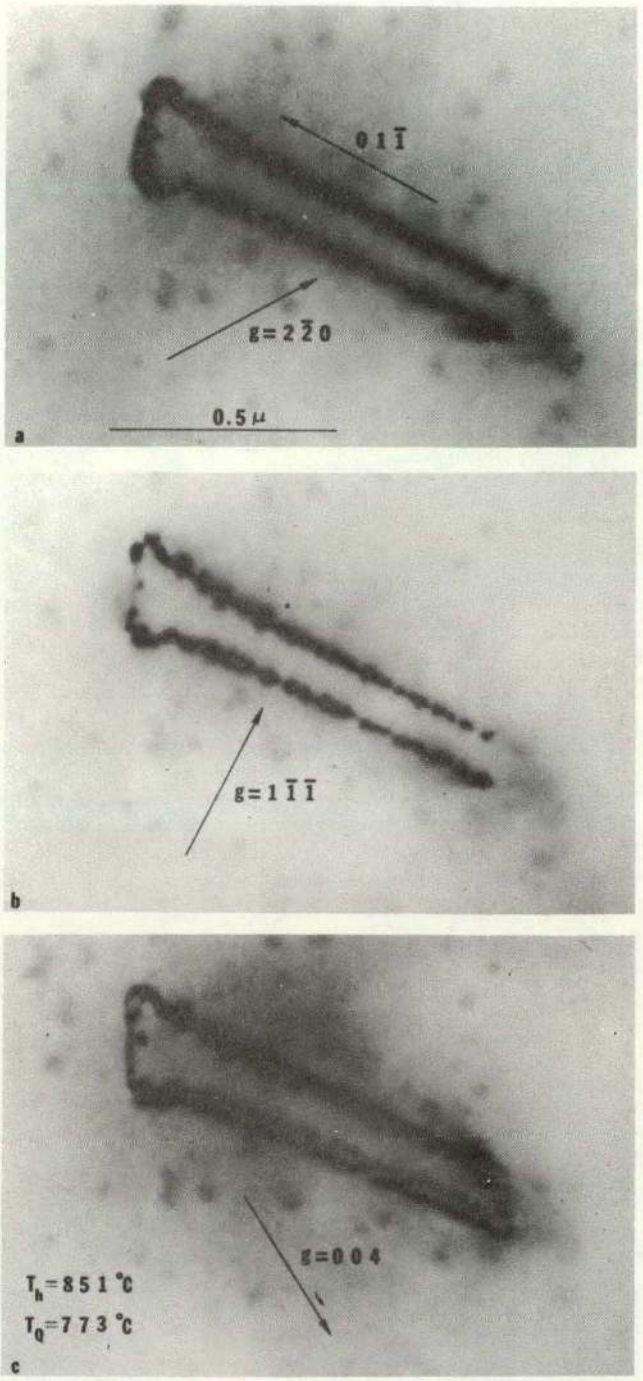

XBB 708-3632

Fig. 27. (160 kV) A ⟨110⟩ colony arm in a (110) foil. The plane of the configuration is (100). The colony was stopped in its growth at T_Q = 773°C. (a) Strong dislocation contrast. (b) The dislocation is nearly out of contrast, strong precipitate contrast. (c) Strong dislocation contrast.

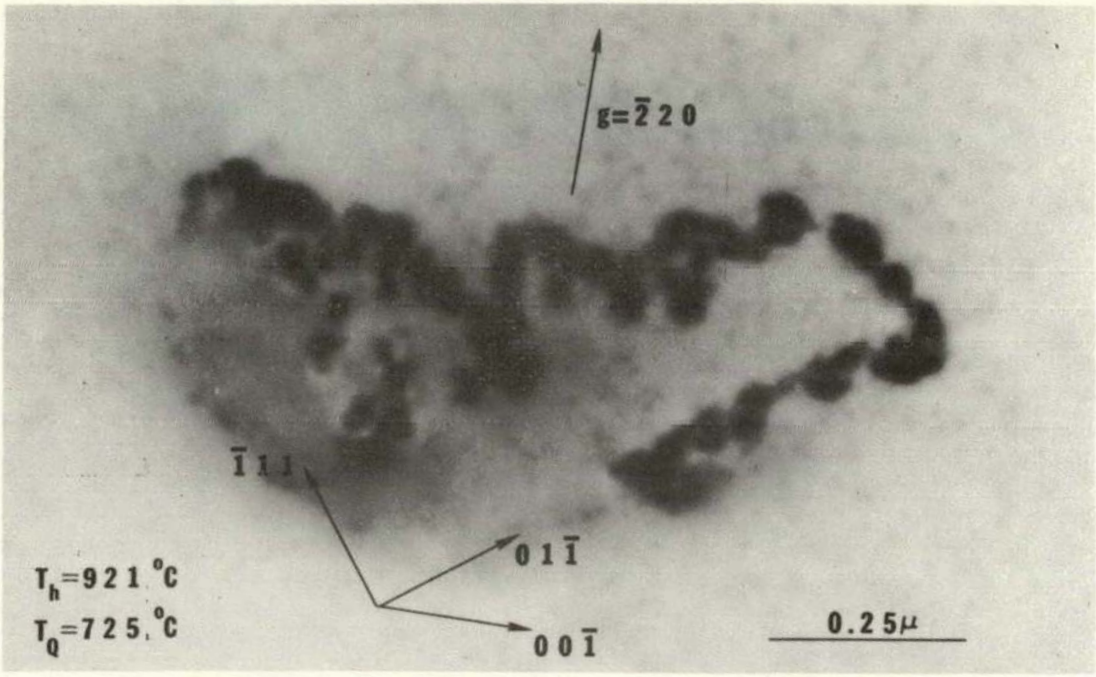

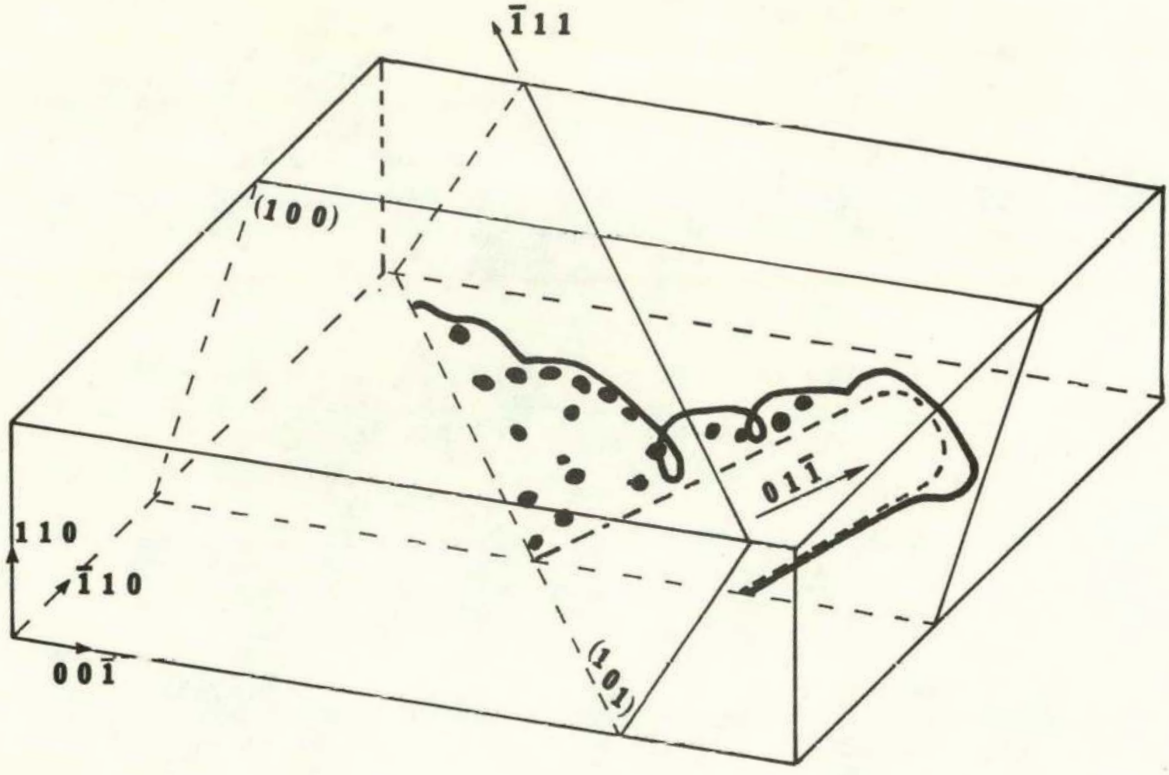

XBB 707-3132

Fig. 28. (100 kV) A [101] colony arm in a (110) foil. The colony was stopped in its growth at T_Q = 25°C. Note the transition from growth on (100) planes to a helical expansion on (101) planes.

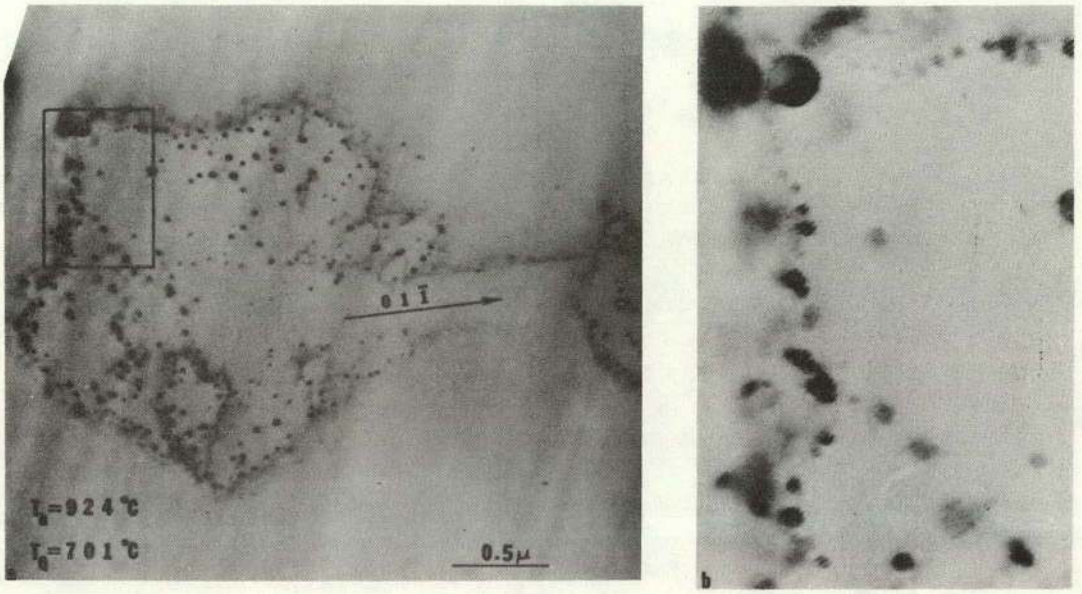

XBB 708-3633

Fig. 29. (650 kV) A [101] colony arm in a (101) foil. The colony was stopped in its growth at T_Q = 701°C. (a) The contours of the initial (100), [$01\bar{1}$] configuration is still visible. (b) Note the decrease in precipitate sizes close to the big precipitate.

plane. Thus during the initial stage of growth the dislocation loop is not in pure edge orientation; consequently the growth is partially a glide, partially a climb process. The left part of the half loop, Fig. 28, has started to climb on the (101) planes into a helical configuration, leaving precipitates behind.

Figure 29 shows a ⟨110⟩ arm interrupted in its development at temperature 24°C below that of the one in Fig. 28. Thus a more developed (101) arrangement is obtained, however, the contours of the initial elongated loop configuration, oriented in the $[01\bar{1}]$ direction and located in the (100) plane, is still clearly visible.

Note the depleted zone with the large precipitate at the end of the zone close to the dislocation, Fig. 29b. (See Section 3.4.4). An interesting detail is the gradual decrease in the precipitate size close to this large precipitate.

3.6.2 Growth of ⟨100⟩ Type Colony Arms

Figures 30* and 31 represent early stages in the development of two [010] type precipitate arms. Both are oeiented in the [101] direction and both have a [010] Burgers vector.**

---

* The unclear image is caused by precipitation along the dislocation lines due to electron radiation damage in the high voltage microscope, see Section 3.8.

** The three two-beam bright field reflections in Fig. 31 show that the dislocations are nearly out of contrast in the $[00\bar{4}]$ reflection while in contrast in the $[2\bar{2}0]$ and $[\bar{1}1\bar{1}]$ reflections. This is consistent with a [010] Burgers vector.

The growth of these precipitates were interrupted at 762°C and 707°C respectively. The configuration in Fig. 30 ends (or begins) in a big precipitate inside the foil, while the configuration in Fig. 30 runs through the entire foil.

Even if the two types of colony arms, i.e. of ⟨110⟩ and ⟨100⟩ type, in the initial stage both appear as elongated loops oriented in the 110 directions, several characteristic differences are apparent in comparing precipitation on climbing 110 dislocations and on climbing 100 dislocation. Contrary to the ⟨110⟩ case where small precipitates appeared closely distributed along the dislocation lines, the 100 arms have larger precipitates, more widely spaced and connected by segments of very narrow dislocation dipoles.

Figure 30 illustrates the beginning of the dendritic character of the ⟨100⟩ colony arms as a freshly formed branch is oriented in the $[\bar{1}01]$ direction. Note that the image of this branch can be followed as a line of no contrast through the large precipitate, Fig. 30a. One of the precipitates in Fig. 31b has a weak line of no contrast in the $[\bar{1}01]$ direction which suggests the very beginning of a branch in this direction.

Figure 32 presents a section of a ⟨100⟩ colony arm in a (110) foil. This precipitate colony was stopped in its growth at 629°C. The sizes of the colonies observed in this foil were in the same range as in foils prepared from specimens cooled at a "normal" speed down to room temperature. Thus at 630°C the precipitate colonies are fully developed.

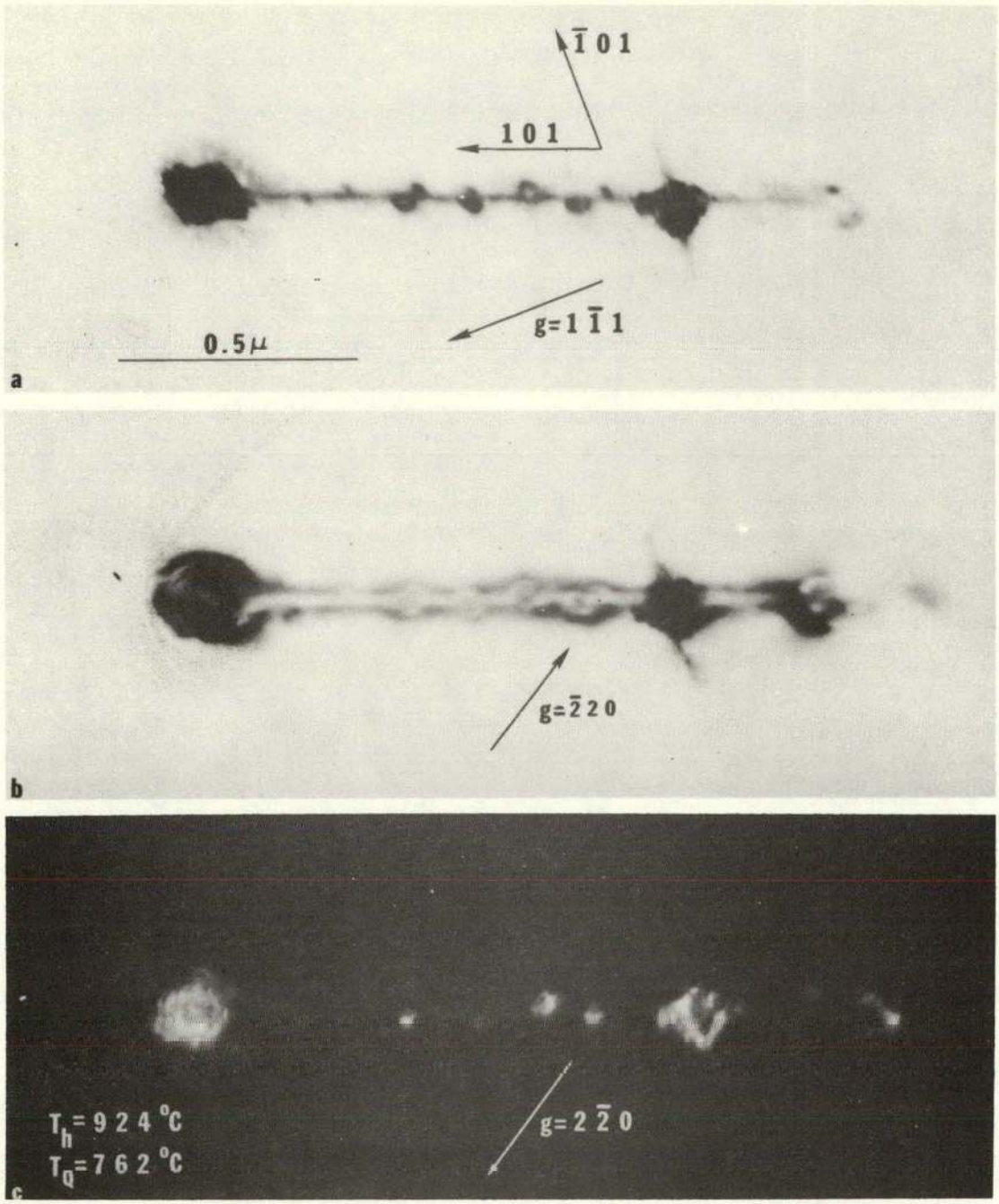

XBB 708-3631

Fig. 30. (650 kV) A [010] colony arm in a (110) foil. The colony was stopped in its growth at T_Q = 762°C. The big precipitates are connected by narrow dislocation dipoles. A new branch is growing in the [$\bar{1}$01] direction.

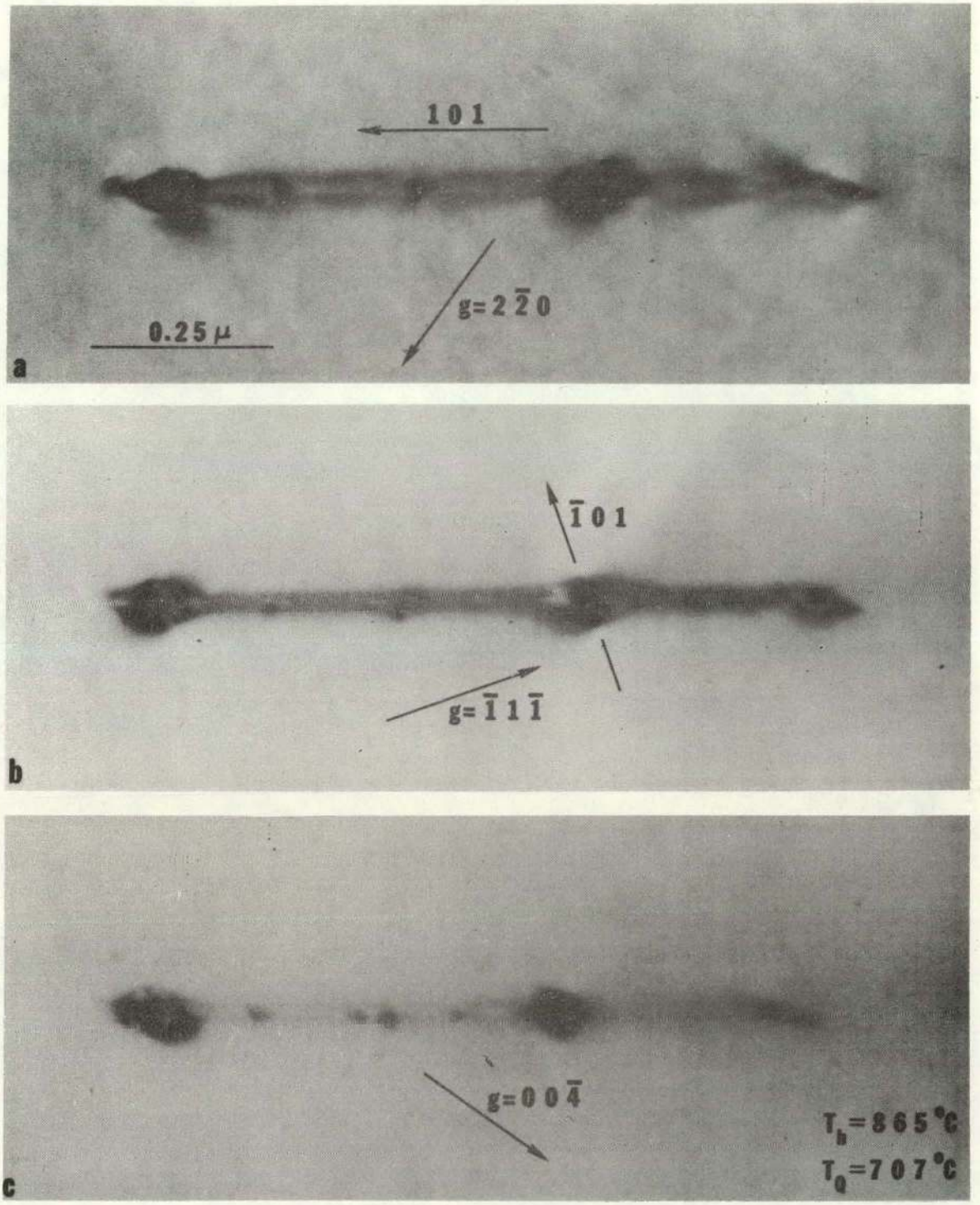

XBB 707-3126

Fig. 31. (100 kV) Two beam bright field micrographs of a [010] colony arm in a (110) foil. The colony was interrupted in its growth at T_Q = 707°C. (a) The dislocations are in contrast. (b) The dislocations are in contrast, a weak line of no contrast in the [1̄01] direction can be detected in one of the precipitates. (c) The dislocations are out of contrast.

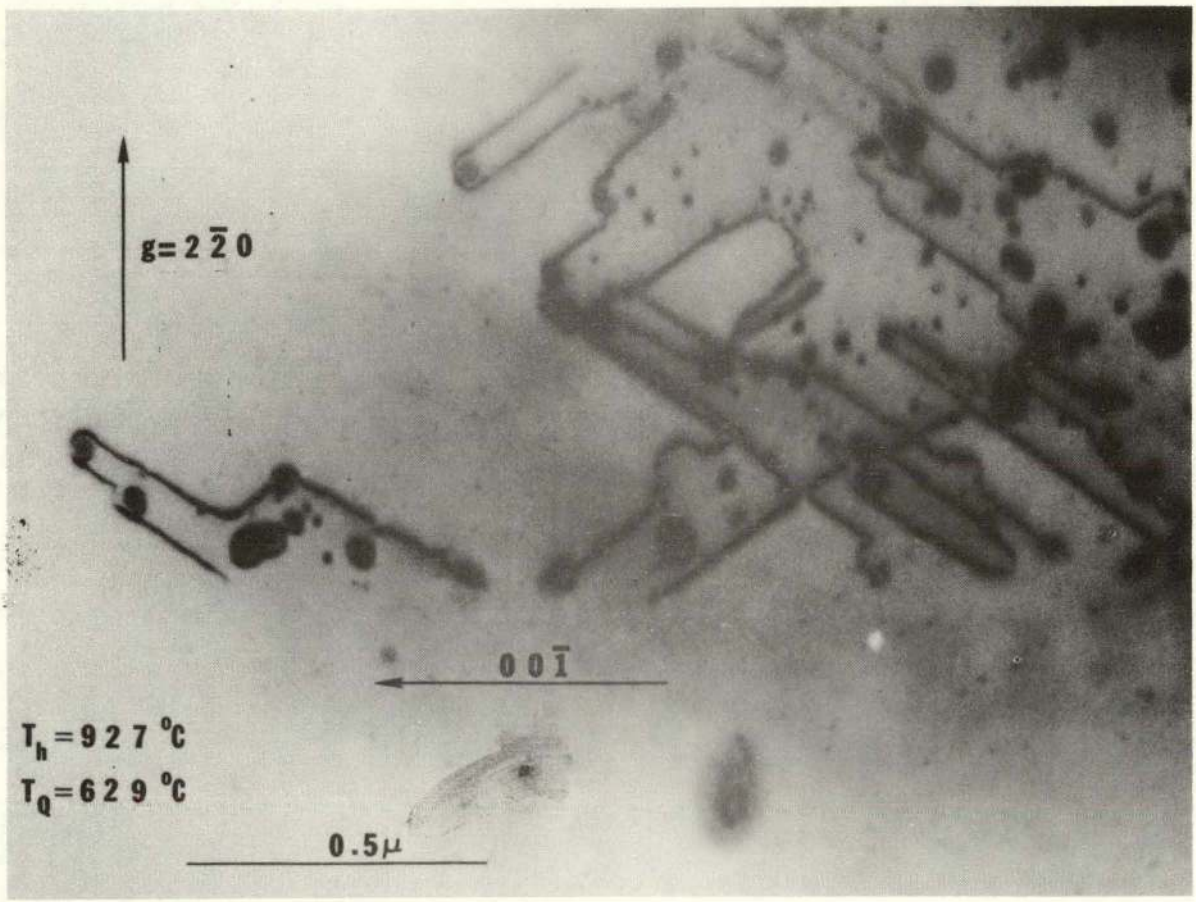

XBB 707-3124

Fig. 32. (100 kV) A [010] colony arm in a (110) foil. The colony was interrupted in its growth at T_Q = 629°C.

3.7 Copper and Iron Concentrations

The iron and copper content in heat treated silicon specimens have been analyzed.

The copper content was by neutron activation analysis* measured to be, 0.095± 0.0025 ppm. This copper concentration corresponds to the solid solubility in silicon[25] at about 650°C.

Spark source mass spectrometry† gave the iron concentration as less than 0.2 ppm. To account for the present effect in terms of iron precipitation an iron concentration of only about 0.02 ppm** is required.

3.8 Precipitation Due to Radiation Damage in the High Voltage Microscope

3.8.1 Precipitation on Dislocations

The high voltage electron beam causes additional precipitation along the dislocations. This effect is illustrated by the micrographs presented in Fig. 33a to c. As this precipitation is limited to areas of the foil illuminated by the electron beam only, it is concluded that this effect is caused by the high energy electrons. The micrographs in Fig. 33 are all recorded within a period of about 10-15 minutes, and at a beam voltage of 650 kV. This voltage is far above the threshold voltage required for an electron to eject a silicon atom from a lattice position by direct collision. For silicon this threshold energy is about 170 keV.††

---

*Analysis performed by Gulf General Atomic, Incorporated.

†Analysis performed by Bell and Howell.

**The solid solubility of iron[26] in silicon at about 800°C.

††The threshold energy is approximately proportional to the atomic weight of the target atom, being 166 keV for aluminum and about 500 keV for copper.[27]

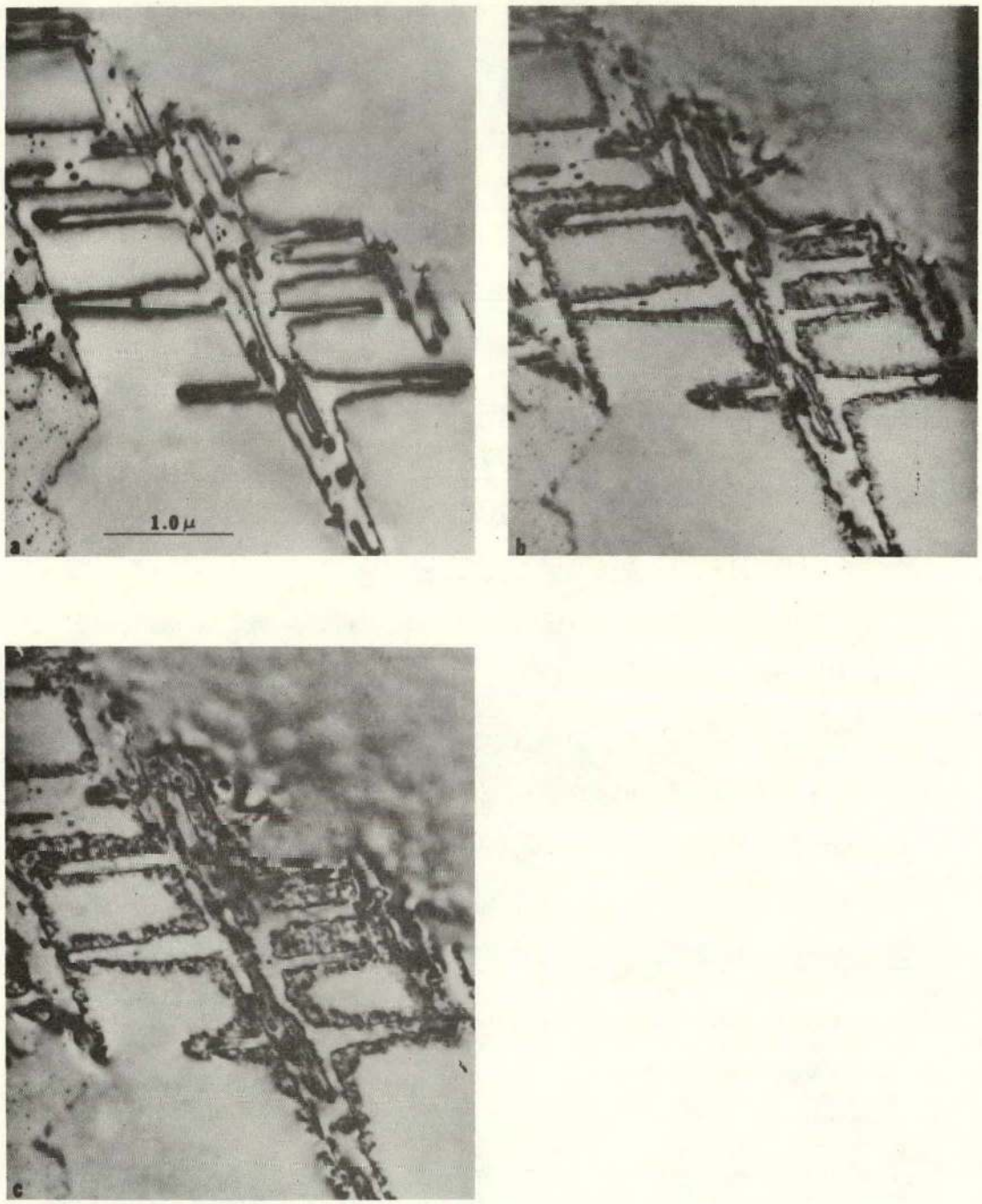

XBB 706-2844

Fig. 33. (650 kV) Precipitation along the dislocations due to electron radiation damage. The colony arm is of ⟨100⟩ type and the three micrographs were exposed at time intervals of a few minutes.

The time intervals between the three exposures in Fig. 33 are only a few minutes. Considering that the foil temperature at most is a few 100°C, the precipitation has occurred very rapidly. This rapid development imposes serious limitations on dislocation contrast studies at higher beam voltages. Note that the precipitates are formed on the outside of the enveloping dislocation line only, i.e. on the tension side of the interstitial edge loops. The stress field may cause this preferential precipitation outside the loops, in addition the inside of the dislocation is already depleted of the precipitating species. Probably because of the larger Burgers vector, this effect is much more pronounced for [100] than for [110] dislocations.

Individual precipitates cannot be resolved, but a whisker like structure can be recognized in the heavily precipitated areas in Fig. 32b and c, which indicates a high density of small needle like precipitates. The direction of the needles is normal to that of the dislocation protrusion along which they are formed.

3.8.2 Radiation Damage at Higher Temperatures

A different mode of radiation induced precipitation occurred during annealing of the foil in the high voltage electron microscope hot stage. Typical results are presented in Figs. 34a to d. Figure 34 shows that a high density of long needles have been formed after annealing for about one hour and fifteen minutes at 700°C. This foil contained, in addition to the colony shown in Fig. 34, several other precipitate colonies, needles however, were only formed in the colonies illuminated by the electron beam. Thus, this precipitation effect, like the one described above, is caused by electron radiation damage.

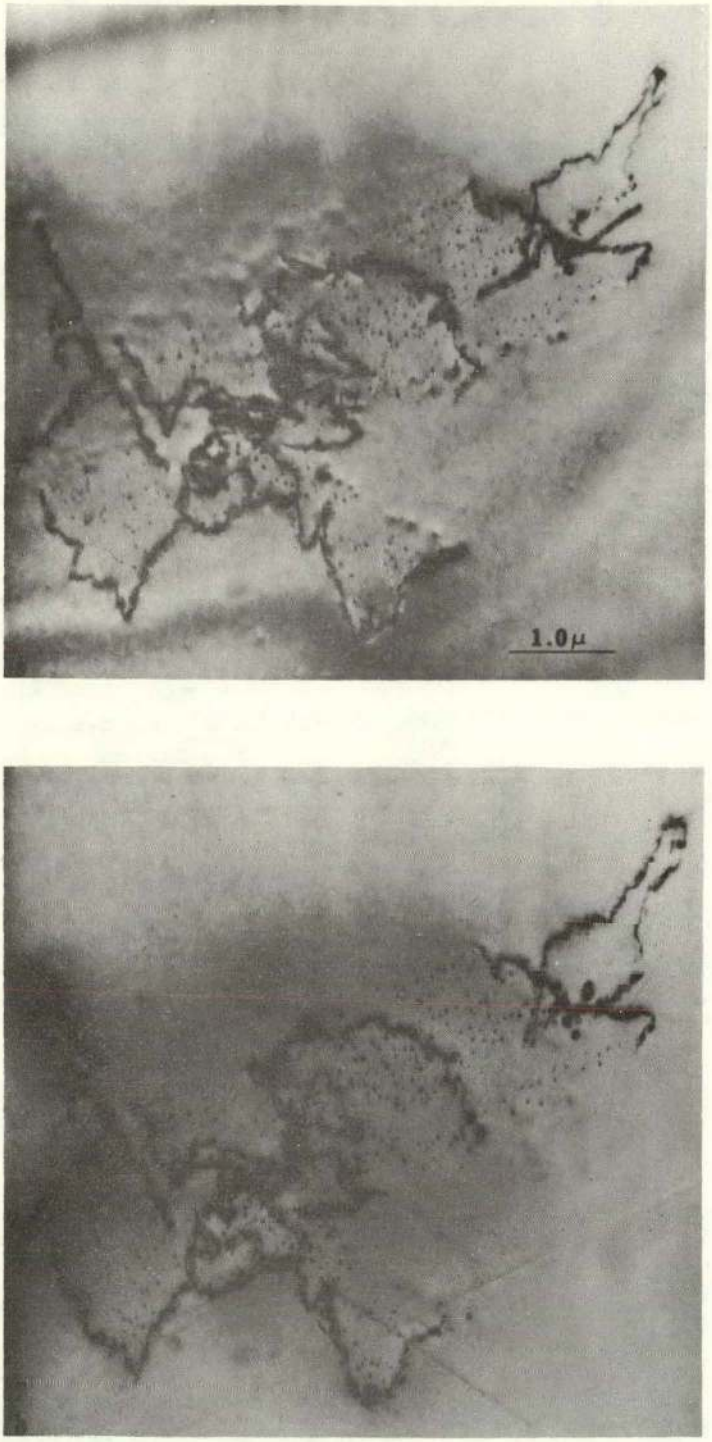

XBB 706-2846

Fig. 34. (650 eV) Hot stage observation of the formation of needle-like precipitates due to radiation damage. (a) 110 type colony in a (111) foil, the micrograph is taken before the heating started. (b) After annealing the foil for about 60 minutes at 680°C.

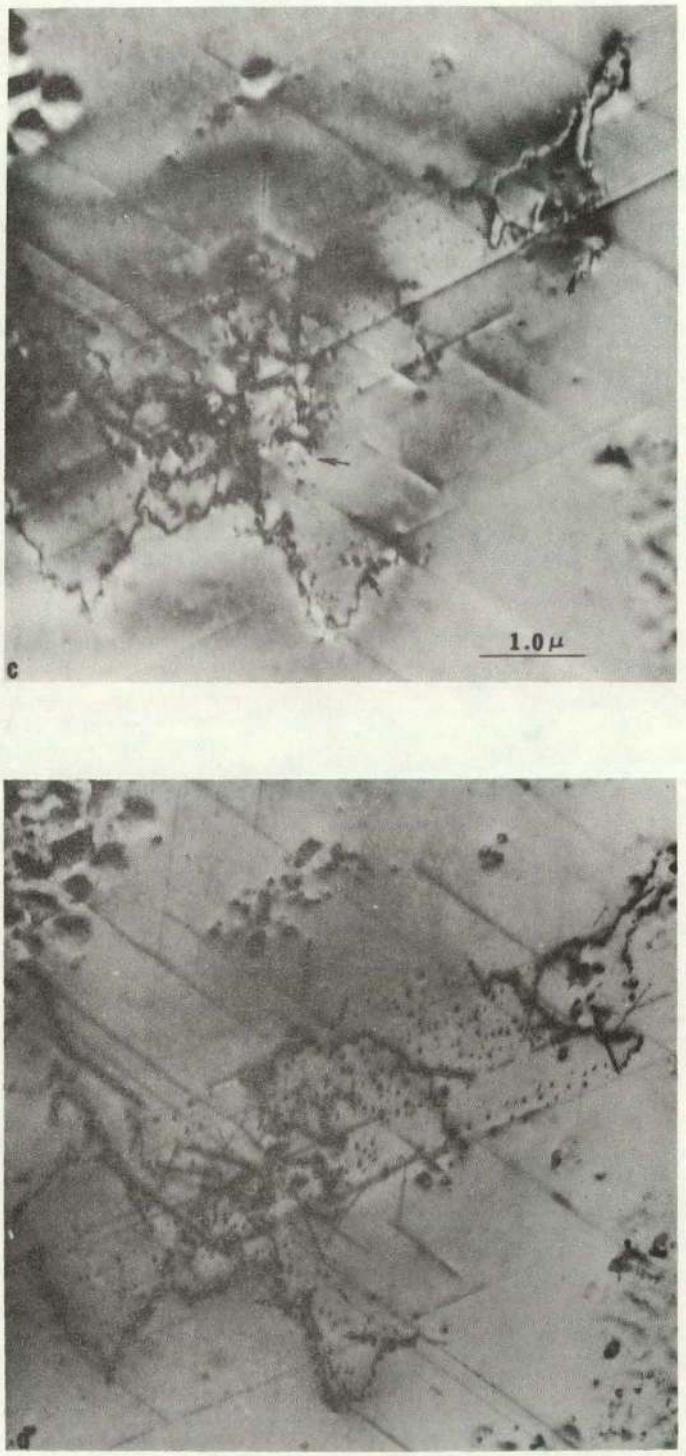

XBB 706-2849

Fig. 34. (c) Taken about 10 minutes later than exposure b at 750°C, note the contrast oscillations along the needles marked by arrows. (d) Taken after cooling down to room temperature.

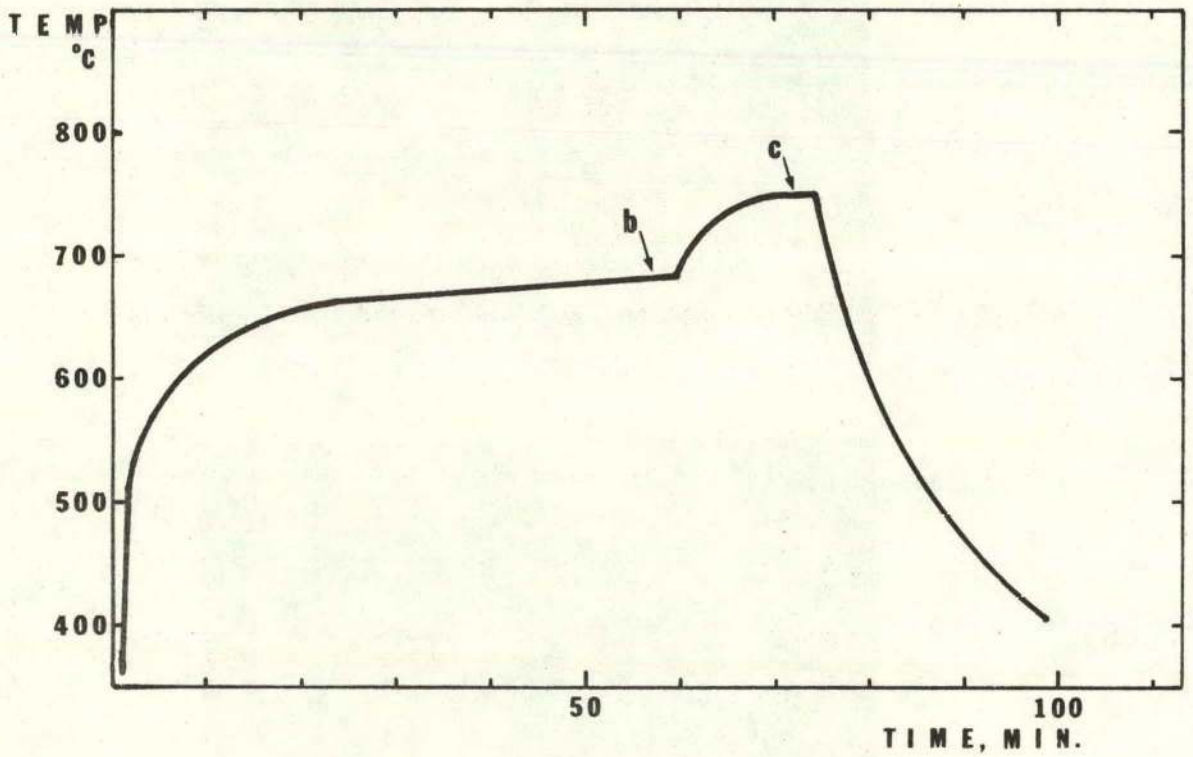

XBL 707-1557

Fig. 34. (e) Diagram showing the heat treatment of the foil.

The needle precipitation rate is strongly temperature dependent. The diagram in Fig. 34e shows the heat treatment given to the foil. Figures 34a and d are taken before and after the heat treatment respectively, the time for the other exposures are indicated in the diagram. The micrograph in Fig. 34b was recorded after about 60 minutes at 670°C, only a few needles have developed. By raising the temperature to about 750°C the nucleation rate of the needles was drastically increased, Fig. 34c.

The contrast oscillations along the needles marked by arrows in Fig. 34c show that these needles are strongly inclined to the foil surfaces. All needles are oriented in ⟨110⟩ crystallographic directions, with the very long needles parallel to the foil surfaces. Some of the needles are up to 10 μm long, the diameter varies from about 40 Å to about 200 Å. Figure 34b suggests that the needles may be nucleated at the dislocation line.

3.9 Summary

1. The colonies have a star or dendritic shape.

2. Each arm of a star represents a planar arrangement of precipitates, surrounded by an interstitial edge dislocation loop. Most colonies contain two different kinds of arms: associated with a ⟨100⟩ and a/2 ⟨110⟩ dislocations respectively.

3. ⟨110⟩ type arms are bounded by nearly circular dislocations and lie on the {110} plane perpendicular to the Burgers vector of the dislocation. ⟨100⟩ arms are dendritic in shape with branches in ⟨110⟩ directions that lie in the plane perpendicular to the Burgers vector.

4. The colonies are distributed in a periodic array of layers which are normal to the growth axis. Colony density within the layers is 10^6-10^7 cm^{-3}.

5. The precipitates have a cubic lattice structure, a = 5.65±0.01 Å.

6. The precipitates have tentatively been identified as α-Fe_3Si.

7. Orientation relationships:

   Precipitates belonging to ⟨110⟩ arms: A cube to cube symmetry

   Precipitates belonging to ⟨100⟩ colony arms:

   $(11\bar{2})_p \parallel (001)_m$

   $[1\bar{1}0]_p \parallel [1\bar{1}0]_m$ or $[110]_m$

8. The precipitate colonies are formed during cooling from higher temperatures. Nucleation of the colonies starts at about 800°C.

9. A critical cooling rate is required.

10. ⟨110⟩ type colony arms first appear as elongated loops on {100} planes with the Burgers vector at an angle of 45° with the loop plane. Pure climb expansion of the dislocation loop starts at about 730°C.

11. In the initial stage the ⟨100⟩ colony arms contain larger precipitates connected by very narrow dislocation dipoles. The dislocations are in pure edge orientation. Branches in different ⟨110⟩ directions start to develop around 770°C.

12. Both types of colony arms are fully developed by the time the temperature has dropped to about 650°C.

4. DISCUSSION

4.1 The Solubility and Diffusivity of Iron in Silicon

Previous work on the solubility and diffusivity of iron atoms in pure silicon is scarce.[26,28,29] The solubility curve presented in Fig. 35 is taken from a review article by Trumbore,[26] on the solubility of impurities in silicon. The iron solubility in silicon as measured by Struthers[28] and Collins and Carlson,[29] disagree by as much as two to three orders of magnitude for temperatures below 1200°C. However, as pointed out by Collins and Carlson who checked Struthers tracer experiments at 1200°C, the amount of iron used in the tracer experiments might have been insufficient to obtain the equilibrium solubility. Trumbore therefore, draws the solubility curve of iron, Fig. 35, arbitrarily to favor Collins and Carlson's data.

Iron atoms diffuse in the silicon lattice with an activation energy 0.86 eV,[28] and the diffusivity constant $D_0 = 6.20 \times 10^{-3}$ cm^2/sec. Collins and Carlson[29] indicate that two species of iron might be present; a fast and a slow diffusing. The fast and slow diffusing species are interpreted as iron atoms interstitially and substitutionally dissolved respectively.

From the present investigation the minimum iron concentration at about 800°C can be estimated by observing that each colony contains about 10^8-10^9 iron atoms, and that the bulk density of clusters is about $10^6 cm^{-3}$. By distributing the iron atoms evenly throughout the bulk, this gives a minimum iron concentration prior to precipitation, $C_{Fe} > 10^{14}$ $atoms/cm^3$. Figure 35 gives the iron solubility at 800°C to about 2×10^{15} $atoms/cm^3$.

The colony configuration in Fig. 21 contains about 10 precipitates

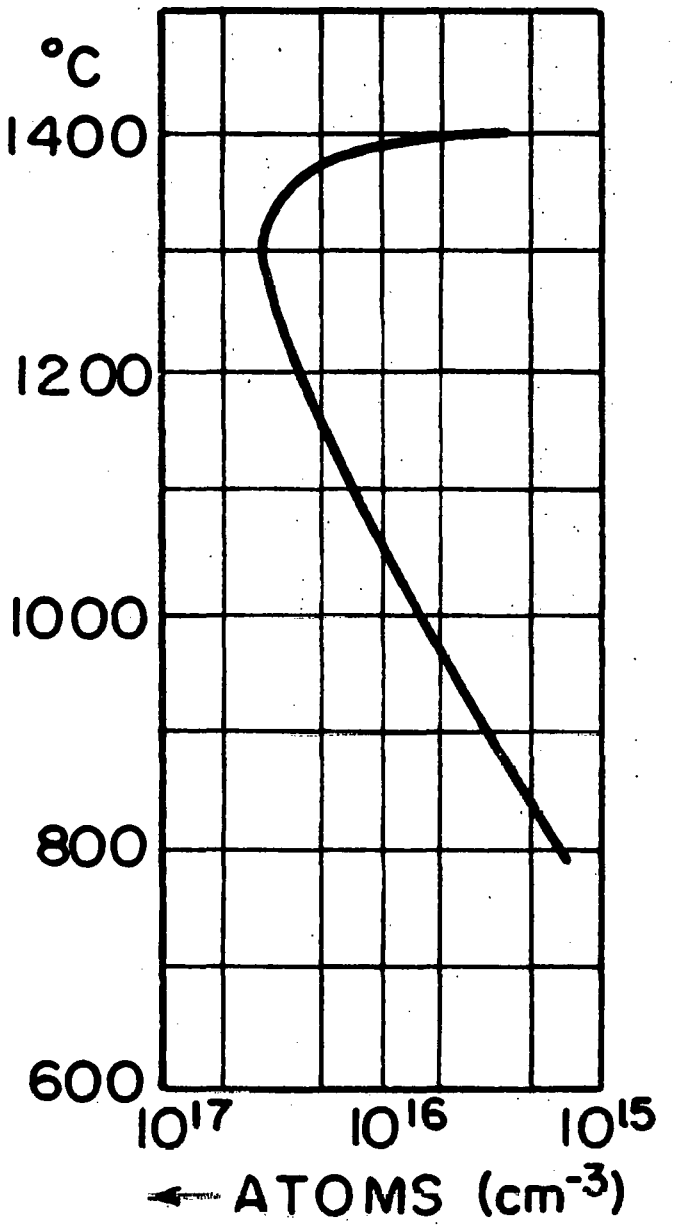

XBL 707-1551

Fig. 35. The solid solubility of iron in silicon.

representing $2X10^7$ iron atoms. If the iron concentration is about $2X10^{15}$ atoms/cm^3 a spherical volume of 10 μm has to be drained to account for this number of iron atoms. A rough estimate of the iron diffusivity necessary to explain the formation of this colony can be found from the relation, $X^2 = Dt$, where X is the radius of the drained volume, i.e. 10 μm, D is the average diffusivity for the cooling period, taken to be that at 800°C with a corresponding time, t, about 10 sec. This gives $D_{Fe} > 10^{-7}$ cm^2/sec. The iron diffusivity at 800°C as measured by Struthers[28] is $6.2X10^{-7}$ cm^2/sec.

4.2 General Model for the Growth Mechanism

As the lattice parameters and structure of a precipitating phase in general are different from that of the matrix, the growth of a precipitate usually causes a severe local strain. The exchange of point defects between the particle and the matrix can partially relieve the mismatch. It has been pointed out[30-33] that if there are no dislocations, grain boundaries or other sources of vacancies the growth of a precipitate may cause the nucleation of a dislocation loop.

This theory will be applied to explain the formation of the present precipitate colonies. The proposed growth mechanism is schematically illustrated in Figs. 36a to d. The mismatch strain field is reduced by generation of vacancies at the particle matrix interface. The results in the nucleation of a small dislocation loop which grows out from the precipitate acting as a source of vacancies which move to the growing precipitate by pipe diffusion along the dislocation. As it climbs away from the initial precipitate the loop tends to act as a heterogeneous nucleation site for new precipitates,[34,35] Figs. 36c and d.

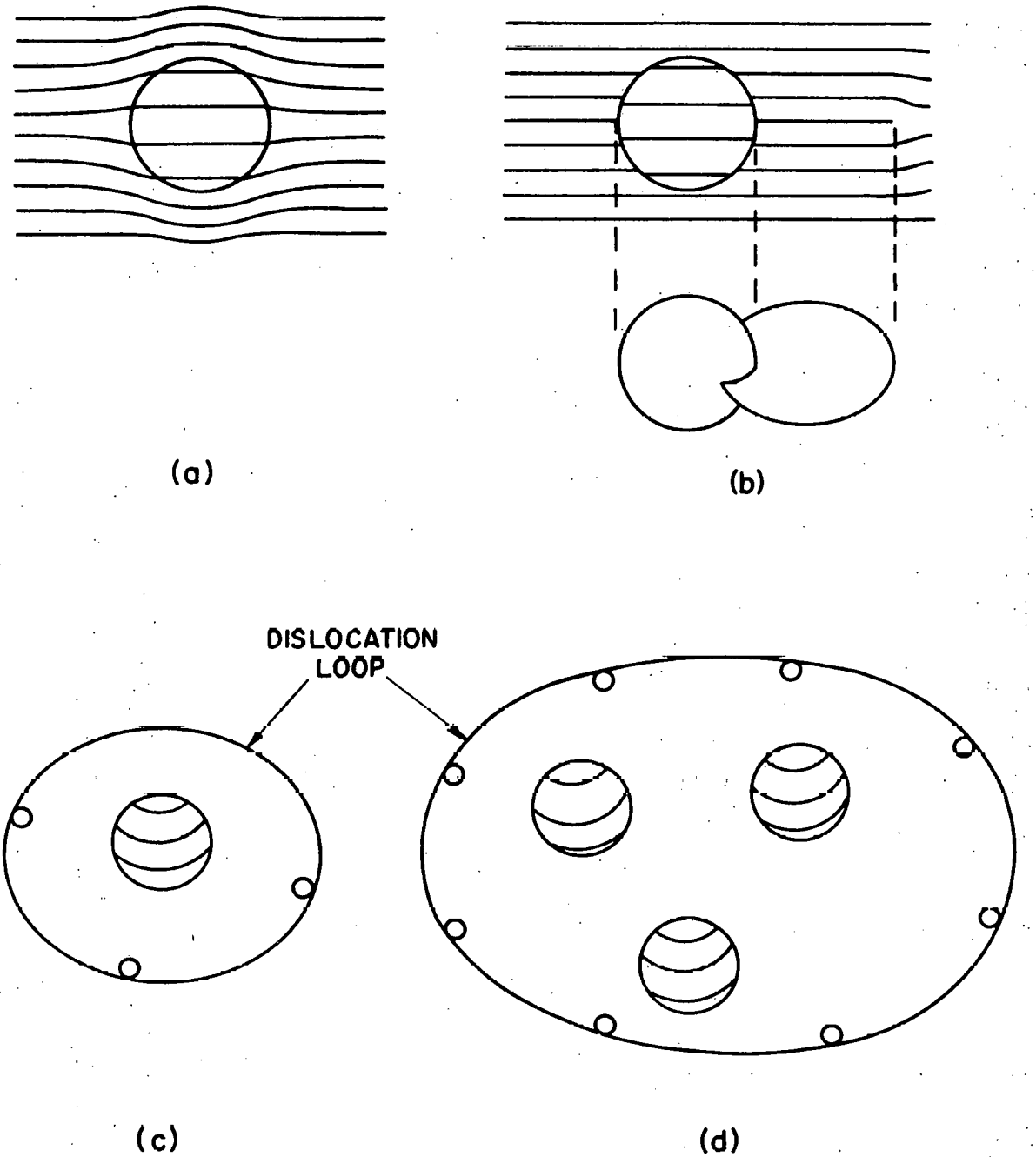

Fig. 36. Sketch showing the growth of a precipitate colony.

This simple model explains the following three fundamental characteristics of the colony branches.

(a) The nearly planar layers of precipitates that make up the colony arms.

(b) The presence of a surrounding dislocation loop.

(c) The interstitial edge character of the dislocation loop.

This model suggests that the number of atoms making up the extra layers of silicon in a colony corresponds to the number of vacancies absorbed by the growing precipitates. By observing the difference in the volume per silicon atom in the matrix and in the Fe_3Si, DO_3 structure, it follows that to account for the number of vacancies absorbed it is necessary to assume that the iron atoms are interstitially disolved.

4.3 The Nucleation Centers

The ring patterns on etched as grown crystal surfaces, Fig. 4a and b, suggest that very small previpitates or point defect clusters are present in the as-grown state even though they have not been observed experimentally. As the bulk distribution of large precipitate colonies is identical to the distribution of these unidentified centers, this suggests that the nucleation of colonies is purely heterogenous in nature. This heterogeneous nucleation mechanism will be discussed in Section 4.4. In the following paragraph the chemical nature of the nucleation centers will be discussed in some detail.

The periodic distribution of nucleation centers in slightly curved layers is interpreted as being a result of the growth process. The layers follow a growth ring pattern, with the curvatrue of the layers reflecting the morphology of the solid liquid interface. To retain this distribution

during the slow cooling, required in the growth process, and through subsequent annealing treatments and to explain the formation of only very small defect clusters even after slow cooling, the diffusivity of the impurities involved must be very small. The diffusivity of iron atoms in silicon is relatively rapid therefore the possibility of having the iron atoms remain segregated into periodic layers can be disregarded. The long needle precipitates, running from surface to surface of the 1 mm thick wafer, Fig. 6a, indicates that the precipitating iron atoms are evenly distributed, independent of the distribution of nucleation centers.

Special attention will be focused on the elements oxygen and carbon. The diffusion of these elements are very slow.[36-38] It is well established that both oxygen and carbon will be present in measurable quantities even in materials graded as of super purity.[6,39-41] Patel[39] has demonstrated that oxygen precipitation occurs during high temperature annealing (above 1000°C) of floating zone silicon crystals presumably "oxygen free". Fiermans and Vennik[6] claim to have detected traces of carbon and oxygen in the centers of star-like copper precipitates formed during quenching of copper saturated low oxygen Lopex silicon. These observations demonstrate that even in the purest available silicon crystals, oxygen can be expected in concentrations exceeding 10^{17} atoms/cm^3.

Kaiser[42] reports that the oxygen concentration in silicon crystals varies periodically in a band structure following the growth rings. By copper decoration of silicon crystals Dash[1] observed the same growth ring pattern. The zones are reported convex toward the melt and attributed to oxygen segregation. This growth ring structure is consistent with the present observations. As no such distribution has been reported for

carbon atoms in silicon, and as the formation of small silica (SiO_2) precipitates are observed[40] during high temperature annealing of silicon, it is believed that the nucleation centers for the iron precipitate colonies are small silica particles.

4.4 Nucleation of Colonies

The precipitate formation requires a critical cooling rate. Fiermans and Vennik[4] found a similar cooling rate effect for precipitation of copper in silicon. However, they pay no attention to this in their explanation of the formation of copper colonies. These authors claim that silica particles in the matrix act as indentation centers during cooling. The indentation is caused by the difference in expansion coefficients between the SiO_2 precipitates and the matrix. This indentation mechanism is disputed for the following reasons: (1) this effect would require silica particles in the as grown material with a diameter of at least 1 μm or more (2) the mechanism is not able to explain the critical cooling effect.

Instead of having dislocations generated by thermal stresses, a model for the heterogeneous nucleation of precipitate colonies based on a vacancy condensation model will now be considered.

4.4.1 Condensation of Thermal Vacancies

If there is no exchange of point defects between the iron silicide nucleus and the matrix, the growing embryo will cause the generation of a severe strain field. Even if the nucleation of the first precipitate of a colony is at a pre-existing defect, most likely minute silica particles, the strain field associated with a coherent nucleus may cause the energy barrier for nucleation to be so high that the nucleation rate is still

virtually zero. A significant drop in this nucleation barrier is expected if the mismatch between the embryo and the matrix is accommodated by simultaneous vacancy condensation. A schematic representation of the free energy of a coherent precipitate in the matrix as a function of particle size is given in Fig. 37. ΔG^* and r^* are the critical nucleus size and activation free energy respectively. If vacancy condensation occur concurrently the free energy curve might be indicated by the broken line.

The concentration of thermal vacancies in silicon at 900°C is very low.[43] However, the number may be sufficient for this nucleation step, i.e. to create iron precipitates with a radius $r > r^*$. In order to establish a nucleation model based on vacancy coprecipitation, the concentration of thermal vacancies has to be evaluated and compared to the number of vacancies required to form supercritical nuclei of a density given by the observed final density of precipitate colonies.

The number of vacancies required to accommodate a spherical particle (α-Fe_3Si) of radius r in the silicon matrix are:

$$N_v = \frac{32}{3} r^3 \left(\frac{1}{a_\alpha^3} - \frac{1}{2a_\beta^3} \right) \qquad (4.1)$$

where a_α and a_β are the linear dimensions of the silicon and α-Fe_3Si unit cells respectively. The critical nucleus radius, r^*, can be estimated from the transmission electron micrographs. Taking the smallest observed precipitates as an upper limit for the critical size gives $r^* \leq 15$ Å. Inserting this value for r in Eq. (4.1) gives $N_v \leq 400$ vacancies. As the cluster concentration is about 10^6 cm^{-3} a vacancy concentration of about 10^8 cm^{-3} is needed.

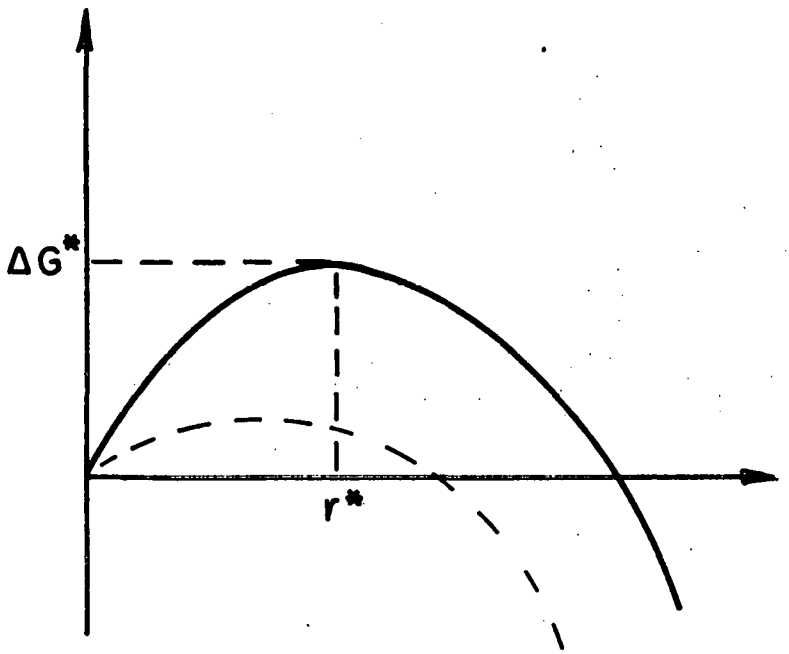

XBL 707-1556

Fig. 37. Schematic representation of the energy barrier for nucleation of colonies. Solid line; no vacancy condensation. Broken line; nucleation with simultaneous vacancy condensation.

The number of vacancies in high temperature thermal equilibrium is much lower in silicon than in metals. As pointed out by Seeger and Swanson,[44] upper and lower limits, may be deduced from the self-diffusion data. Their relations give the equilibrium concentration of vacancies at 900°C in the range 10^7-10^{10} vacancies/cm^3. The upper limit represent a vacancy concentration about two orders of magnitude bigger than required.

4.4.2 The Critical Cooling Effect

Contrary to the case of metal where the equilibrium concentration of vacancies exceeds that of interstitials by a large factor, the high temperature concentration of vacancies and interstitials in silicon are in the same range. At about 900°C the contribution of vacancies and interstitials to the self-diffusion is about equal.[43] Consequently annihilation of vacancy interstitial pairs should be the most effective way of reducing excess point defect concentration. In addition, since the mobility of silicon vacancies and interstitials are very high,[45] the thermal vacancies are expected to anneal out very quickly during a cooling process. This effect may explain why a critical cooling rate is necessary for the nucleation of clusters.

The stress field surrounding small silica particles will attract the silicon vacancies. Also vacancy-impurity centers have been observed in silicon, especially oxygen-vacancy centers (A-centers) have been extensively studied. The A-centers, however, disappear upon annealing abobe 575°C.[46,47] As the number of iron atoms dissolved in the silicon lattice exceeds that of vacancy-interstitial pairs (at about 900°C) by about 6 orders of magnitude, a vacancy might be expected to spend part of its time in association with an interstitial iron atom. The concentration

of iron-vacancy centers during the cooling period would be expected to be proportional to: (1) the binding energy for vacancy-interstitial iron pairs, (2) the cooling rate. The driving force for the nucleation process would be the supersaturation of iron-vacancy pairs. This model appears to have the elements required to explain the observed critical cooling rate effect. If the cooling rate is too slow the vacancies are expected to anneal out and the vacancy-iron pair supersaturation will not reach a value necessary for nucleation of colonies. If the cooling rate is too fast there will be no time for the colonies to develop.

4.5 Growth of Precipitate Colonies

The nucleation step is followed by the generation of an interstitial dislocation loop, as described in the foregoing section. This dislocation loop can supply needed vacancies for further growth of the nucleus and act as nucleation sites for new precipitates.

The growth model for the precipitates as presented in Section 4.2 is too general to adequately explain all of the experimental observations. In order to account for the different habit planes for the two types of precipitate colonies, and the characteristic differences in their growth kinetics, a more refined model will now be developed.

The following three sections present first a discussion of the initial stages of growth, and then the growth kinetics of the two different growth modes.

4.5.1 The Initial Stage

By the initial stage is understood the stage immediately following the nucleation step, that is, the transition from a nucleus precipitate to a precipitate with an edge dislocation loop around it. The question

to be answered is, how does a growing precipitate, having a misfit with the matrix but which is initially fully or partially coherent, lose coherency during growth? One mechanism would be the punching out of prismatic loops. This mechanism has most recently been treated by Weatherly.[33] He concludes that loss of coherency by the punching mechanism is in most cases very unlikely. The interfacial structure of semi-coherent precipitates have been experimentally investigated by Weatherly and Nicholson.[48] They report that coherency is lost either by the climb or glide of dislocations from an exterior source to the precipitate-matrix interfaces, or by the growth of small loops inside the precipitates. a third possible mechanism may be the accumulation of point defects from the matrix.[32,33]

The loss of coherency and the subsequent formation of a precipitate dislocation loop configuration has in the present investigation not been observed experimentally.

For the colony growth experiments, Section 3.6, the first appearance of the colonies were always as elongated dislocation loops containing many precipitates, Figs. 27, 30 and 31. The earliest history of the two colony types, i.e. ⟨110⟩ and ⟨100⟩, might appear as shown in Figs. 38a and 39a. The two different Burgers vectors may have been nucleated directly or the a ⟨100⟩ type dislocation may be formed by a reaction between two a/2 ⟨110⟩ type loops.[31]

4.5.2 Growth of ⟨100⟩ type Colony Arms

After being nucleated the dislocation loop grows quickly into a configuration like Fig. 38b. A model showing the interaction between the growing precipitates which have been nucleated along the line and

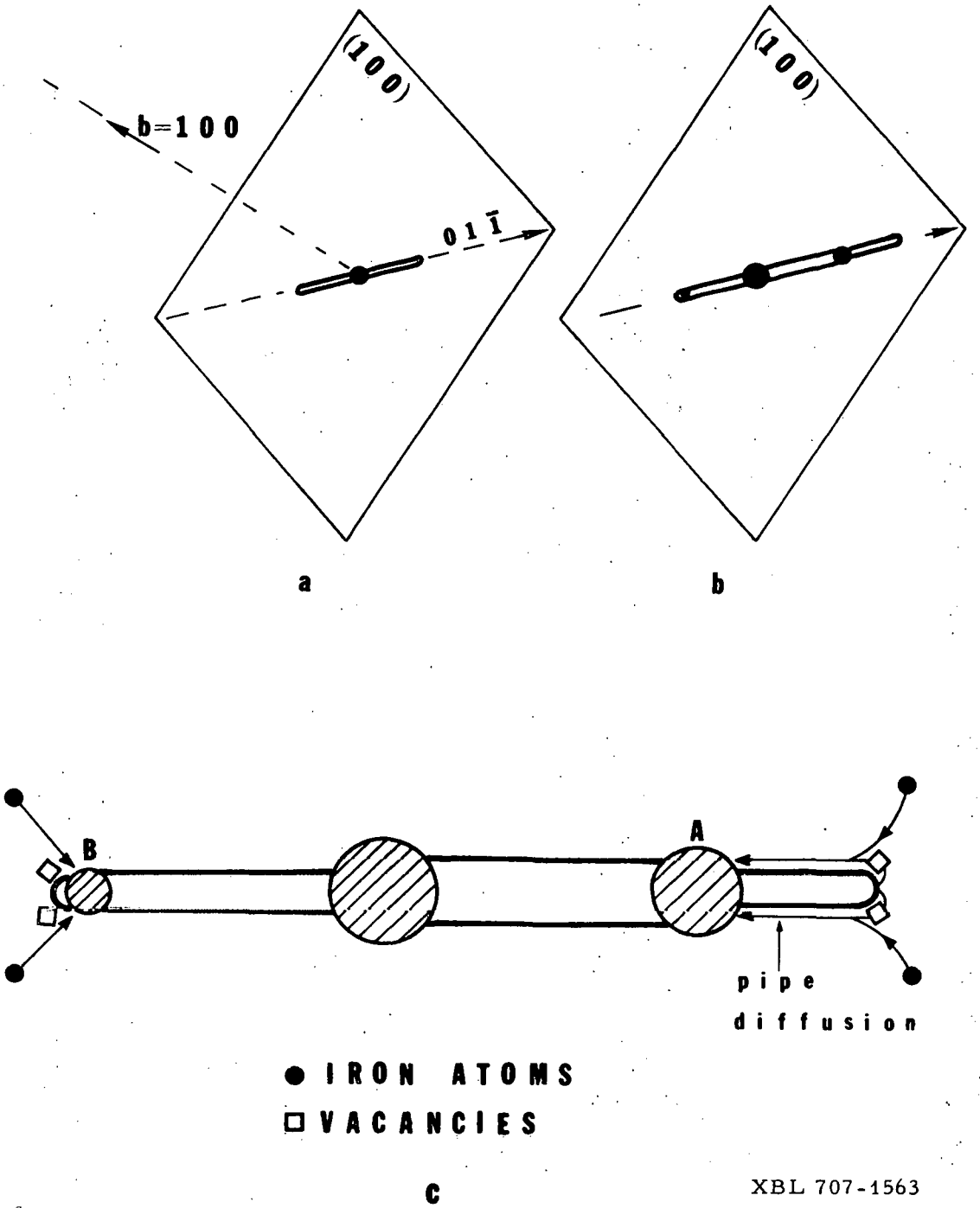

Fig. 38. Schematic representation of the growth of a ⟨100⟩ type colony arm during the initial stages.

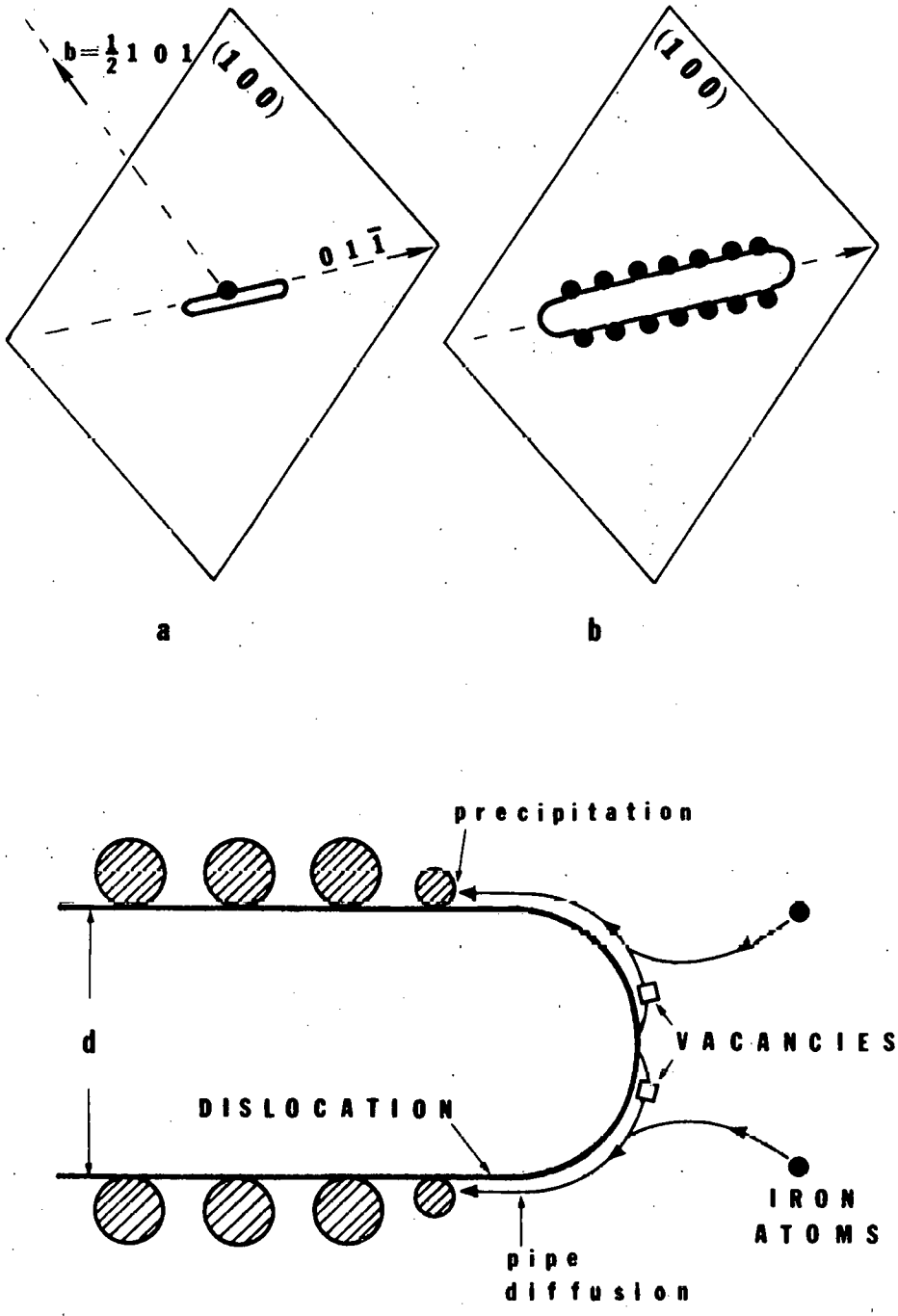

XBL 707-1561

Fig. 39. Schematic representation of the growth of a ⟨110⟩ type colony arm in the initial stage.

the expanding loop is presented in Fig. 38c. The iron atoms in the supersaturated solid solution condense on the tip of the dislocation loop. As explained in Section 4.2 this precipitate growth requires vacancies. The vacancies are also formed at the tip causing dislocation climb. Both vacancies and iron atoms move to the growing precipitates, marked A and B in Fig. 38c, by pipe diffusion. The strongly elongated shape of the loop is a dendritic growth phenomenon. The loop ends have a more favorable diffusion geometry than the rest of the loop, thus by assuming this shape the loop ends will always reach into undepleted regions of high supersaturation. The densely packed 110 crystallographic directions are most probably preferred as they represent low energy directions for the dislocation.

The stage of development shown in Figs. 38b and c is followed by two more steps in Figs. 40b and c. Figure 40a illustrates the early start of a branch in the [011] direction. Configurations like Fig. 40a have been observed experimentally, Figs. 30 and 31. Continued growth of this structure will, followed by nucleation of additional branches, result in a configuration like Fig. 40b. The structure of the freshly formed branches have not been determined. It could be a very narrow elongated loop growing out from the larger precipitates as described above. However, another possibility is that a new branch is nucleated as a needle which at a later stage breaks up in a precipitate dislocation dipole configuration. The radiation induced precipitates observed at higher temperatures, Section 3.8.2, indicate a tendency to form needle shaped precipitates.

A characteristic feature of the ⟨100⟩ colony arms observed at lower temperatures is that large precipitates are located on the tips of the

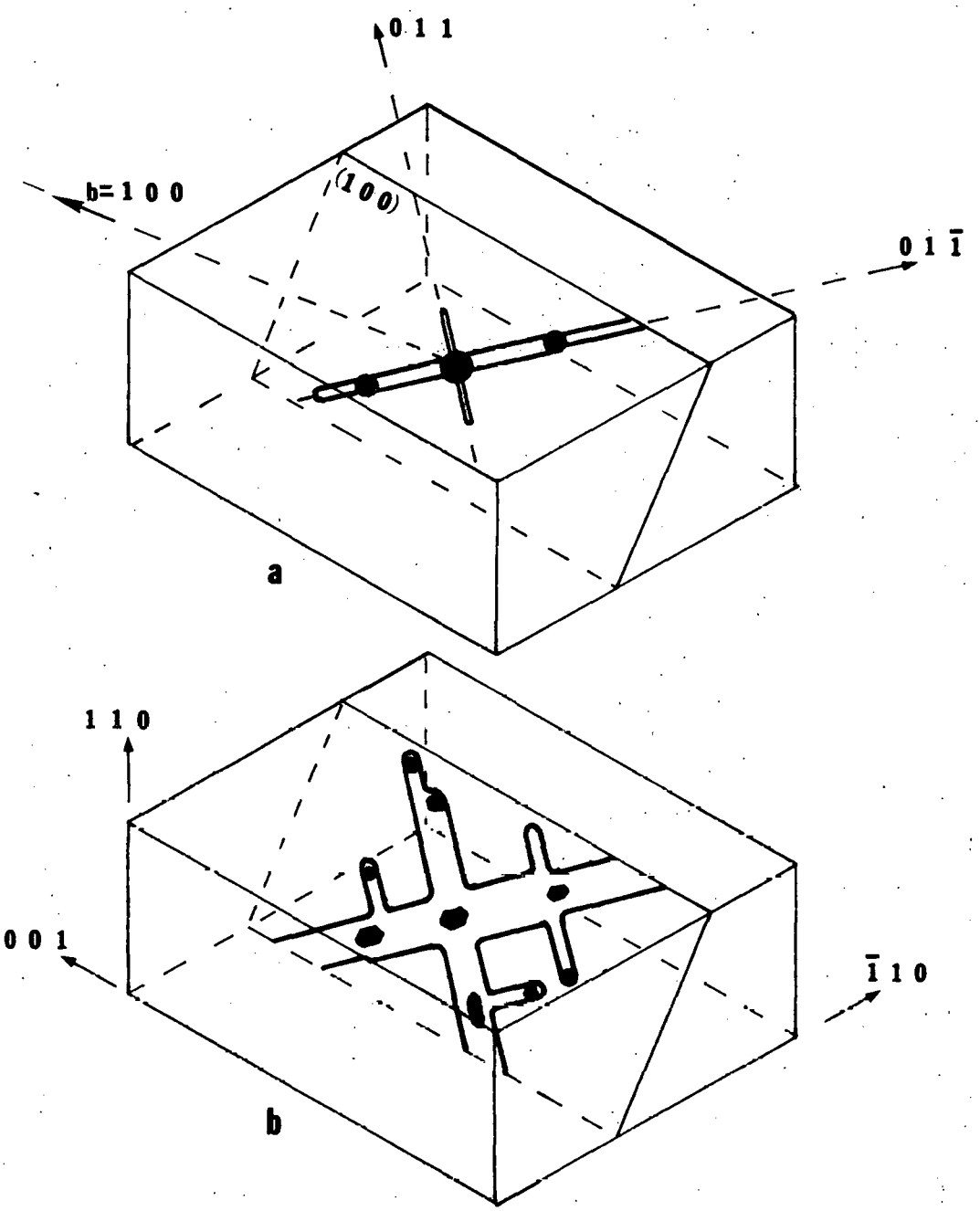

Fig. 40. Sketch showing the growth of ⟨100⟩ type colonies.

dislocation protrusions, Fig. 32. The growth of these precipitates have not been observed experimentally. They are, however, believed to be formed in the following way.

During the last stages of growth the tendency to dendritic like growth may well be counter balanced by the amount of energy being dissipated in dislocation production. Instead of forcing out new dislocation loops, the precipitation may cause a widening of the existing branches. This process will result in a shortening of the total length of the high energy dislocations involved in the ⟨100⟩ configurations. This effect may explain why the protrusions observed at lower temperatures are rather wide compared to the very narrow dipole segments connecting the precipitates at higher temperatures.

4.5.3 Growth of ⟨110⟩ Type Colony Arms

The big difference in the growth kinetics between the ⟨110⟩ and ⟨100⟩ growth modes is probably due to the difference in Burgers vectors involved. The larger Burgers vector for the ⟨100⟩ configurations may facilitate pipe diffusion along the dislocation core. The iron atoms and the silicon vacancies can be transported over long distances along the pipe, thus causing the precipitates to grow larger and to be spaced farther apart.

Although the growth of ⟨110⟩ type colony arms may be characterized by a more or less radially expanding dislocation loop, which leaves behind an even density of precipitates as illustrated in Section 4.2, this model fails in explaining several important features in the observed growth of ⟨110⟩ arms, Sections 3.4.5 and 3.6.1. That is (1) the two stages of growth, i.e. first as an elongated loop occupying a {100} plane followed by pure climb expansion on {110} planes, (2) the frequent formation of depleted zones observed within the ⟨110⟩ colony arms.

After being nucleated the ⟨110⟩ dislocation loop grows quickly into a configuration like Fig. 39b. The growth mechanism for this loop, Fig. 39c, is in principle the same as that described for the precipitation on ⟨100⟩ dislocations in the foregoing section. The plane of the loop is at an angle of 45° to the Burgers vector. The long axis is oriented in a ⟨110⟩ direction, thus the end sections of the loop are the only ones in pure edge orientation. These end sections of the loop are the most effective sources of vacancies, combined glide and climb of these tips may cause the elongated shape of the loop.

The growth rate of the loops can be estimated from the observations that several μm long loops have been formed at temperatures as high as 770°C. As the cooling rate is about 8°C/sec and the precipitation is observed to start at about 800°C this gives a growth rate in the long direction of the loops of about 0.5 μm/sec.

Why the ⟨110⟩ arms initially preferred to grow on {100} planes cannot be considered established. This configuration is energetically unstable in terms of the balence between the increase in dislocation length compared to the amount of vacancies needed for the growth of the precipitates. Consequently this elongated loop shape was observed to break down, Section. 3.6.1. This transition from the elongated loop configuration into the familiar ⟨110⟩ type colony arms is illustrated in Figs. 41a to c. Figure 41a shows a (101) type configuration at the same stage of development as shown in Fig. 39b. Continued growth causes nucleation of helical turns on (101) planes, Fig. 41b. By pure climb the configuration expands forming parallel (101) arms, Fig. 41c. This growth could have taken place on a series of parallel planes resulting in a helical dislocation,

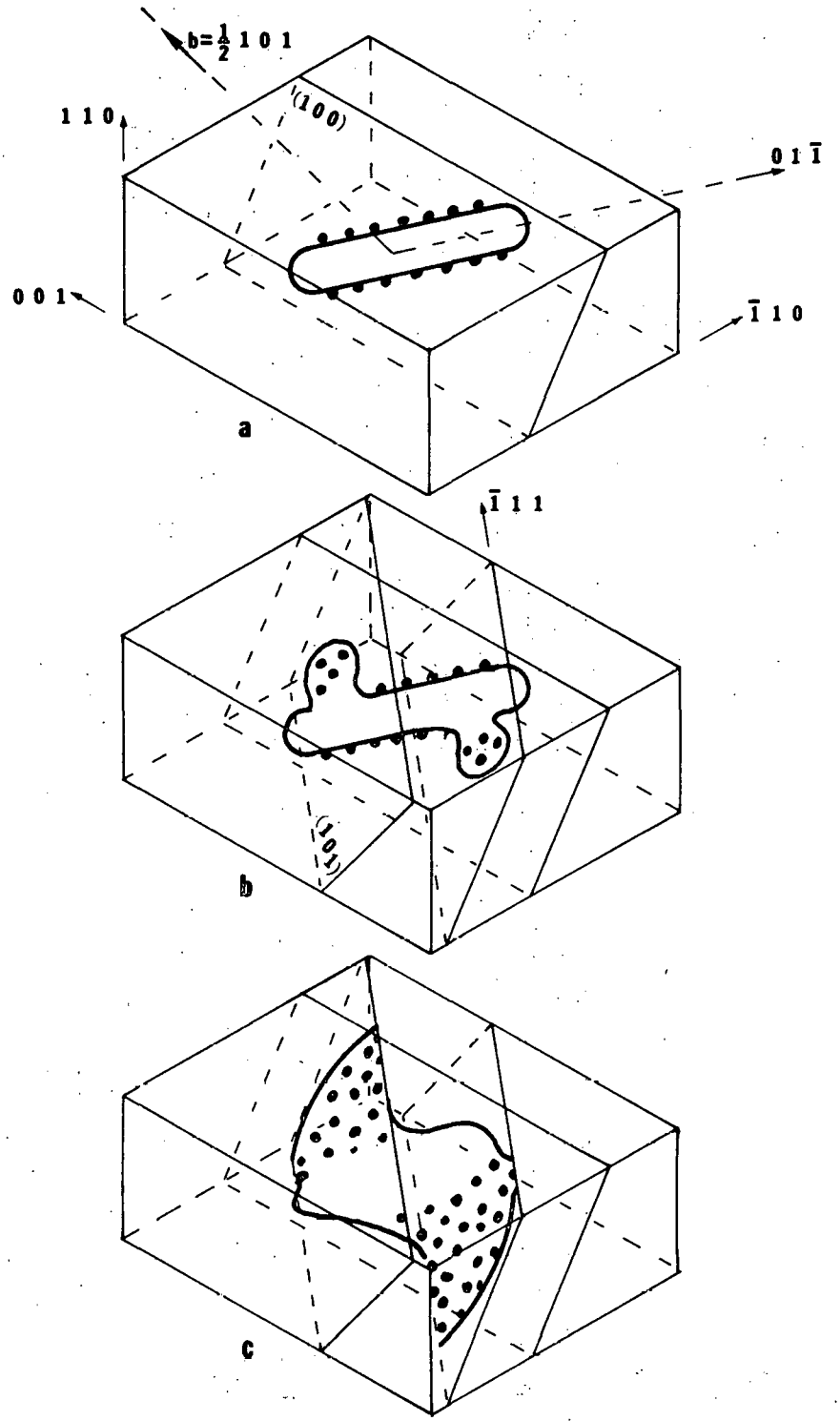

XBL 707-1558

Fig. 41. Schematic representation of the transition from (a) a (100) planar configuration into, (b and c) [101] type colony arms.

precipitate configuration. An indication of such growth is shown in Fig. 28. As this helical configuration is rarely observed in specimens cooled at a "normal" rate down to room temperature, the first helical turns to be formed must expand very fast, leaving small chances for extra turns to develop, thus stretching the configuration out on only a few parallel planes.

As outlined in Section 3.4.5 the ⟨110⟩ arms frequently contain depleted zones with a larger than average precipitate in the zone end closet to the climbing dislocation. The development of these zones has not been observed experimentally. Based on the observed tendency to dendritic growth the following mechanism is suggested to explain the effect. The formation of the depleted zones can be understood in terms of the same model as used to describe the growth of the elongated loops, Fig. 39c. A schematic step by step model for the formation of a depleted zone is presented in Figs. 42a to d. Figure 42a illustrates a section of a growing {110} branch, the climbing dislocation leaves behind a nearly uniform distribution of precipitates. At one point, A, along the dislocation line a small bow out appears. Small irregularities in the growth may result in such bow outs. As described above this bow out section of the dislocation will have a more favorable diffusion geometry and therefore start to climb ahead faster than the rest of the dislocation. The result is a dislocation protrusion like in Fig. 42b. The growth mechanism for this protrusion is the same as schematically illustrated in Fig. 39c. This protrusion is stopped in its growth by some unidentified obstacle at B. As the precipitate formed at the tip of the protrusion can drain a nearly spherical volume around it for

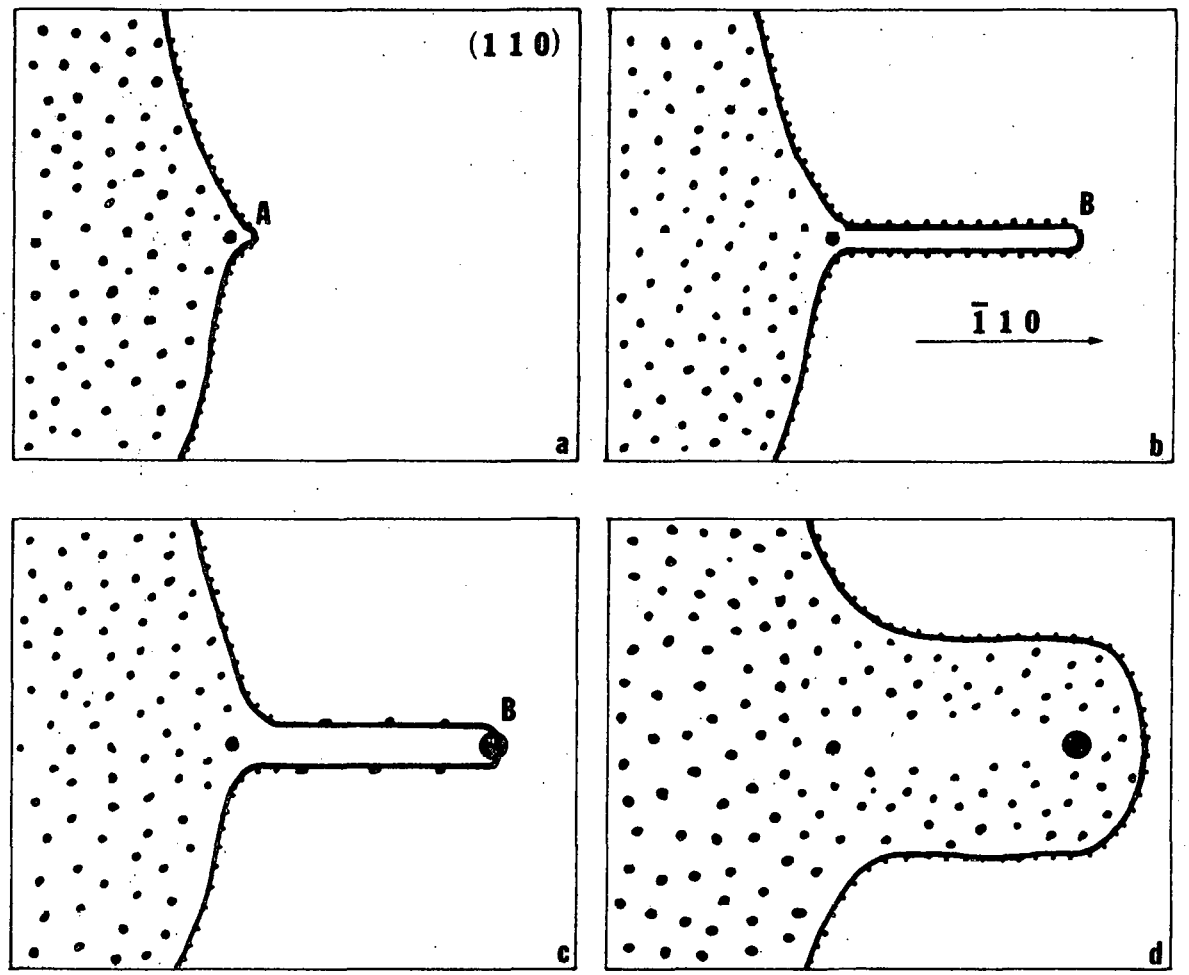

XBL 707-1578

Fig. 42. Sketch showing the formation of a depleted zone in a [110] type colony arm.

iron atoms it will develop into a bigger than average size. This draining effect of the big zone end precipitate is illustrated in Fig. 29, note the gradual decrease in precipitate sizes close to the big precipitate. Finally the dislocation will grow away from the big precipitate and leave behind a depleted zone with the characteristic over-sized precipitate in the zone end closest to the dislocation, Fig. 42d.

More experiments are required in order to find out why, at special sites along the evenly expanding a/2 ⟨110⟩ loop, a small dislocation segment suddenly speeds up in a certain direction. Further, why when just started this dendritic type of growth stops to be followed again by an even climb expansion of the configuration.

5. CONCLUSIONS

The experimental results and the subsequent discussion lead to the following conclusions.

1. The impurity concentration in as grown Lopex silicon crystals is sufficient to cause precipitation of a second phase if the specimens are annealed at temperatures above 700°C followed by a critical cooling rate.

2. The precipitating phase has been tentatively identified as α-Fe_3Si.

3. To account for the number of vacancies absorbed by the growing precipitates it is necessary to assume that the iron atoms are interstitially dissolved.

4. The precipitate colonies are nucleated heterogeneously. It is suggested that the nucleation centers are minute silica particles.

5. The difference in growth kinetics between $\langle 110 \rangle$ and $\langle 100 \rangle$ colony arms may be a result of the difference in the dislocation Burgers vector. Dendritic-like growth of the precipitate-loop configurations may be facilitated by easier pipe diffusion along a $\langle 100 \rangle$ Burgers vector dislocation compared to that along a a/2 $\langle 110 \rangle$ dislocation.

6. The different precipitate-matrix orientation relationships for precipitates belonging to the two types of colony arms are believed to be a result of the different strain fields associated with the a $\langle 100 \rangle$ and a/2 $\langle 110 \rangle$ Burgers vectors.

ACKNOWLEDGMENT

The author is deeply grateful to Professor Jack Washburn for his guidance, encouragements and advice throughout this investigation. My special thanks are also due to Professor Gareth Thomas and Mr. Lutgard De Jonghe for many stimulating discussions, and to Miss Margaret Robson and Mr. Donald Jurica for their assistance in the electron microscope laboratory.

This work was done under the auspices of the U. S. Atomic Energy Commission through the Inorganic Materials Research Division of the Lawrence Radiation Laboratory.

REFERENCES

1. W. C. Dash, J. Appl. Phys. 30, 459 (1959); 31, 205 (1960).
2. G. H. Schwuttke, J. Electrochem. Soc. 108, 163 (1961).
3. H. Reiger, Phys. Stat. Sol. 7, 685 (1964).
4. L. Fiermans and J. Vennik, phys. stat. sol. 12, 277 (1965).
5. L. Fiermans and J. Vennik, phys. stat. sol. 21, 463 (1967).
6. L. Fiermans and J. Vennik, phys. stat. sol. 22, 463 (1967).
7. E. S. Meieran and K. E. Lemons, Adv. in X-ray Analysis 8, 48 (1964).
8. A. R. Lang, Acta. Met. 5, 358 (1957); Acta. Crystallogra. 12, 249 (1959).
9. V. C. Kannan, Direct Observation of Motion of Dislocations in Deformed Silicon by X-ray Topography, (Ph. D. Thesis, University of California) UCRL-18673, Jan. 1969.
10. J. E. Lawrence and H. Hoehler, J. Sci. Inst. 42, 270 (1965).
11. E. Sirtel and A. Adler, Z. fur Metallk. 52, 529 (1961).
12. G. Thomas, Phil. Mag. 17, 1097 (1968).
13. P. B. Hirsch, et al., Electron Microscopy of Thin Crystals (Butterworth, London) (1965) p. 343.
14. W. B. Pearson, Handbook of Lattice Spacings and Structures of Metals 2, (Pergamon Press, 1967).
15. M. C. M. Farquhar, H. Lipson and A. R. Weill, J. Iron Steel Inst. 152, 457 (1945).
16. F. Lihl and H. Ebel, Arch. Eisenhuttenw., 32, 489 (1961).
17. P. B. Hirsch, et al., Electron Microscopy of Thin Crystals (Butterworth, London) (1965) p. 95.
18. V. A. Phillips and J. D. Livingston, Phil. Mag. 7, 969 (1962).
19. P. B. Hirsch, et al., Electron Microscopy of Thin Crystals (Butterworth, London) (1965) p. 178.

20. P. B. Hirsch, A. Howie and M. J. Whelan, Phil. Trans. A 252, 499 (1960).

21. A. Howie and M. J. Whelan, Proc. Roy. Soc. A 262, 217 (1961).

22. M. F. Ashby and L. M. Brown, Phil. Mag. 8, 1083 (1963).

23. G. Thomas, Thin Films (American Society for Metals) (1964) p. 227.

24. G. Thomas and W. L. Bell, phys. stat. sol. 12, 843 (1965).

25. H. H. Woodbury and W. W. Tyler, Phys. Rev. 105, 84 (1957).

26. F. A. Trumbore, Bell Syst. Tech. J. 39, 205 (1960).

27. M. J. Makin, Phil. Mag. 18, 637 (1968).

28. J. D. Struthers, J. Appl. Phys. 31, 2275 (1956).

29. C. B. Collins and R. O. Carlson, Phys. Rev. 108, 1409 (1957).

30. H. Brooks, Metal Interfaces (Cleveland:American Society of Metals) (1952) p. 20.

31. R. G. Baker, D. G. Brandon and F. Nutting, Phil. Mag. 4, 1339 (1959).

32. J. W. Mitchell, J. Appl. Phys. 33, 406 (1962).

33. G. C. Weatherly, Phil. Mag. 17, 791 (1968).

34. J. W. Cahn, Acta. Met. 5, 169 (1957).

35. R. B. Nicholson, Electron Microscopy and Strength of Crystals (Interscience, 1963) p. 861.

36. Corbett, McDonald and Watkins, J. Phys. Chem. Solids 25, 873 (1964).

37. R. C. Newmann and J. B. Willis, J. Phys. Chem. Solids 26, 375 (1965).

38. R. C. Newmann and J. Wakefield, J. Phys. Chem. Solids 19, 230 (1961).

39. J. R. Patel and B. W. Batterman, J. Appl. Phys. 34, 2716 (1963).

40. J. R. Patel, Discussion, Faraday Soc. 38, 201 (1964).

41. W. Schenk, Solid State Electronics 8, 767 (1965).

42. W. Kaiser, Phys. Rev. 105, 1751 (1957).

43. A. Seeger and K. P. Chik, Phys. stat. sol. 29, 449 (1968).

44. A. Seeger and M. L. Swanson, Vacancies and Diffusion Mechanism in Diamond-Structure Semiconductors (Int'l Sym. Lattice Defects in Semiconductors, Tokyo, Sept. 1966).

45. G. D. Watkins, J. Phys. Soc. Japan 18, Suppl. II, 22 (1963).

46. J. W. Corbett, G. D. Watkins and R. S. McDonald, Phys. Rev. 135A, 1381 (1964).

47. J. C. Corelli, G. Oehler, J. F. Becker and K. J. Eieenbraut, J. Appl. Phys. 36, 1787 (1965).

48. G. C. Weatherly and R. B. Nicholson, Phil. Mag. 17, 801 (1968).

TECHNICAL INFORMATION DIVISION
LAWRENCE RADIATION LABORATORY
UNIVERSITY OF CALIFORNIA
BERKELEY, CALIFORNIA 94720